FINAL TECHNICAL REPORT

AWARD NUMBER: G13AP00057

Reducing Uncertainties in the Velocities Determined by Inversion of Phase Velocity Dispersion Curves Using Synthetic Seismograms

Recipient / Primary Investigators

Shahram Pezeshk
Dept. of Civil Engineering, The University of Memphis, Memphis, TN 38152
Phone: (901) 678-4727, Fax: (901) 678-3026 E-mail:
spezeshk@memphis.edu

Jose Pujol
Dept. of Earth Sciences, The University of Memphis,
Memphis, TN 38152, jpujol@memphis.edu

Mehrdad Hosseini
AECOM Technical Services, Inc., Los Angeles, CA 90017
mehrdad.hosseini@aecom.com

Abstract

Characterizing the near-surface shear-wave velocity structure using Rayleigh-wave phase velocity dispersion curves is widespread in the context of reservoir characterization, exploration seismology, earthquake engineering, and geotechnical engineering. This surface seismic approach provides a feasible and low-cost alternative to the borehole measurements. Phase velocity dispersion curves from Rayleigh surface waves are inverted to yield the vertical shear-wave velocity profile. A significant problem with the surface wave inversion is its intrinsic non-uniqueness, and although this problem is widely recognized, there have not been systematic efforts to develop approaches to reduce the pervasive uncertainty that affects the velocity profiles determined by the inversion. Non-uniqueness cannot be easily studied in a nonlinear inverse problem such as Rayleigh-wave inversion and the only way to understand its nature is by numerical investigation, which can get computationally expensive and inevitably time consuming. Regarding the variety of the parameters affecting the surface wave inversion and possible non-uniqueness induced by them, a technique should be established which is not controlled by the non-uniqueness that is already affecting the surface wave inversion. An efficient and repeatable technique is proposed and tested to overcome the non-uniqueness problem; multiple inverted shear-wave velocity profiles are used in a wavenumber integration technique to generate synthetic time series resembling the geophone recordings. The similarity between synthetic and observed time series is used as an additional tool along with the similarity between the theoretical and experimental dispersion curves. The proposed method is proven to be effective through synthetic and real world examples. In these examples, the nature of the non-uniqueness is discussed and its existence is shown. Using the proposed technique, inverted velocity profiles are estimated and effectiveness of this technique is evaluated; in the synthetic example, final inverted velocity profile is compared with the initial target velocity model, and in the real world example, final inverted shear-wave velocity profile is compared with the velocity model from independent measurements in a nearby borehole. Real world example shows that it is possible to overcome the non-uniqueness and distinguish the representative velocity profile for the site that also matches well with the borehole measurements.

Table of Contents

1. Introduction

Seismic design of structures depends on the realistic anticipation of the ground motions generated from various seismic sources. In the design process, seismic structural stability depends on the rate of seismic hazard for a specific region, and in recent years, engineers and seismologists have been working meticulously to correctly estimate the seismic hazard. Seismic hazard is defined as the response of the earth surface with respect to the ground motion of an earthquake. The seismic wave field generated at the location of the source travels though the earth's crust and reaches beneath the specific local site through the bedrock. Bedrock can be covered by deposits and geological structures with different materials and thicknesses. As the seismic wave field finds its way to the surface, passing through the heterogeneity of the local geology, it might get amplified and de-amplified. The greatest hazard is usually associated with soft deposits where seismic waves at the bedrock are amplified at certain frequency ranges as they reach the surface (Kramer, 1996). An example can be observed from the 2011 Tohoku M_w 9.0 earthquake, where seismic waves are recorded both at the bottom of a borehole and also on the surface at a station with a 320-km hypocentral distance. Figure 1.1 shows the three component seismograms of the surface and the borehole recorded at the station CHBH14 with the same scale. From this figure, it is evident that seismic waves are amplified as they reach the surface.

Site response correlates with the mechanical properties of the soil structure especially in its shallow depth. Among the various mechanical properties of soil, the shear-wave velocity (V_S) plays an important role in characterizing the site response.

The important effect of local geology is observed in sedimentary deposits in the Mississippi embayment area that significantly affect the ground motions in the probabilistic seismic-hazard maps. The reason is the possibility of amplification of seismic waves for certain frequency bands due to the shallow shear-wave velocity contrast between soft and stiff materials and soil behavior (Kramer, 1996; Pujol *et al*., 2002). The amplification of ground motion could adversely affect structures that resonate at periods similar to those of the ground on which they are built.

Reliable estimation of the shear-wave velocity profile is not only useful for site response studies and seismic hazard assessments, but is also of great interest in the context of other domains of engineering such as geotechnical engineering and petroleum engineering. In geotechnical engineering, V_S is used in the foundation design process as one of the properties of the underlying soil; in petroleum engineering, V_S is used for the noise attenuation in reflection sections, and for characterizing the near-surface velocity profiles.
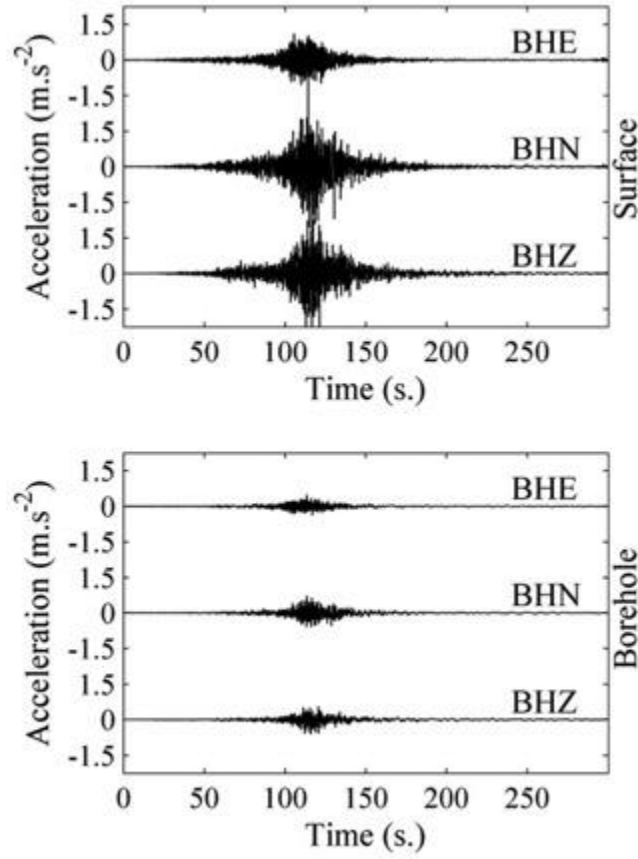
Figure 1.1. Three components of seismograms from 2011 Tohoku M_w 9.0 earthquake recorded on the surface (top) and also in depth of a borehole (bottom) in station CHBH14. The elevation difference between surface and borehole sensors is 525 meters. Seismic waves on the surface are amplified due to the local geology.

1.1　Research Objective

The main objective of this report is to provide a reliable and convenient method for estimation of the shear-wave velocity profile of the subsurface. Such a method will provide site-specific information in detail to improve the seismic hazard maps, specifically for the upper Mississippi embayment region. Soil conditions are often variable even inside of a relatively small area. Thus, to evaluate site-specific seismic hazard and to analyze site response in and around this region, it is necessary to find low-cost methods to obtain shear-wave velocity profiles. In general, borehole logging is considered to be the standard to obtain the needed soil dynamic properties; however, drilling and logging is expensive and this has led to the development of numerous inexpensive surface acquisition techniques. There are issues of non-uniqueness and uncertainties associated with non-invasive procedures that may not result in consistently reliable velocity profiles. Techniques used in this research are expected to improve the non-uniqueness issues in the estimated shear-wave velocity profiles from seismic surface methods, specifically those obtained by analyzing Rayleigh waves.

1.2　Research Overview

This project aims to improve near-surface characterization. A combination of techniques is used to reliably estimate the subsurface shallow shear-wave velocity profile. Currently, there are difficulties with such characterizations such as: (a) velocity reversals due to the presence of a low velocity layer, (b) the decrease in velocity with increasing depth, and (c) the depth of the water table. The problem with the last item is that the Poisson's ratio and density are different for dry and saturated materials. This fact has been usually neglected in the inversion of experimental dispersion curves, which is based on a layered model with small variations across the layers in the values of the Poisson's ratio and density. In fact, early papers on the subject state that the effect of changes in these two parameters is minimal (Nazarian, 1984; Nazarian and Stokoe, 1984). However, recent studies show that this may not be the case when a water table is present (Foti and Strobbia, 2002). In addition, the S-wave velocity models determined by the inversion of phase velocity dispersion curves are affected by a high degree of non-uniqueness because there is little absolute velocity information contained in the phase velocity. This lack of information causes the well-known velocity-depth trade-off (Ammon *et al*., 1990). For example, a thin layer with low velocity will produce an average differential arrival time similar to that caused by a thick layer with high velocity. As a consequence, the inverted velocity models depend on the initial velocity models or on the selected higher mode numbers, resulting in several different inverted velocity models. The proposed methodology helps distinguish among different velocity models by comparing their corresponding synthetic and observed time series.

1.3   Report Overview

Chapter two of this report provides an overview of the estimation of the dispersive properties of surface waves. Chapter two first introduces basic wave propagation theory and unfolds the details of the propagator matrix technique, showing that it can be used for both seismogram synthesis and also theoretical phase velocity estimation in a heterogeneous media. Then, attenuation is presented and the mathematical techniques for implementation of attenuation in the synthesis theory are provided. It is shown how the dispersion is a necessity of a causal system, and some simulations are presented which will be used in development of future theories and assumptions for synthetic seismograms and comparison among observations and synthetics in future chapters.

 Chapter three introduces the devices used in the MASW technique and unveils the details for a successful acquisition of surface waves. Common sources of error and uncertainties are introduced, including amplitude clipping and also the erroneous performance of the trigger which can adversely affect the reliability of results. At the end of Chapter three, the dispersion curve obtained by the MASW technique is compared with that from another surface seismic test (spectral analysis of surface waves, SASW) to see how close is the agreement of the two methods.

Chapter four sets forth the details of the calculation of the experimental dispersion curve from a recorded time series. This section discusses details of the frequency-wavenumber technique and sheds light on this signal processing method by synthetic and   real examples. Chapter four also shows a technique to invert the experimental dispersion curve for the shear-wave velocity structure of the subsurface, and the formulation of the iterative Levenberg-Marquardt inversion is provided. Program SURF96 from Dr. Robert Herrmann (St. Louis University) is introduced, and it is shown how the source code and settings are customized for a successful inversion in shallow applications. A few "bash" scripts are provided and explained to make the suggested modifications practical and repeatable.

Chapter five introduces a synthetic example of the non-uniqueness in the inversion of surface waves, and demonstrates how easy it is to get confused among the pool of different inverted velocity profiles. To solve this problem, a synthetic seismogram technique is used to help separate the real representative profile from the other profiles.

Finally, Chapter six applies all of the techniques explained in the previous chapters to the surface wave data recorded at a site near Memphis, Tennessee, and navigates the reader through the multiple techniques and all the details leading to the detection of the most reliable inverted shear-wave velocity profile. At the end of this chapter, an independent and solid evaluation of the proposed technique is performed by comparing the final inverted profile with the result from a downhole seismic survey. In a second evaluation, the inverted profile is also compared with those from two seismic tests at two sites with similar geology. Previously, two groups of researchers investigated these two sites using borehole and surface wave measurements, and I found it quite useful to compare my outcome with their published results.

2. Literature Review and Basics of Wave Propagation

Knowledge regarding the near-surface seismic velocities unveils information about the subsurface lithology that is not available from surface geological observations (Petrosino *et al.*, 2002). Elastic properties of subsurface materials shed light on factors affecting the wave propagation phenomena, and enables researchers to predict ground motion and ultimately seismic hazard for a local site. Specifically, attenuation and shear-wave velocity structure in the top 30 meters play an important role for the estimation of strong ground motion at a site by estimating the amplification of ground motions or "site effect" (Bard and Bouchan, 1980a, 1908b; Boore *et al.*, 1994; Borcherdt, 1994; Cramer *et al.*, 2002; Electric and Power Research Institute [EPRI], 1993; Evans and Pezeshk, 1998; Frankel and Vidale, 1992; Kramer, 1996; Malagnini *et al.*, 1995; Moczo, 1989; Pezeshk and Zarrabi, 2005; Pezeshk *et al.*, 1998).

The shear-wave velocity profile is estimated by considering the dispersive properties of Rayleigh and Love waves in a vertically heterogeneous medium (Brune and Dorman, 1963; Dorman and Ewing, 1962) and systematic approaches are developed for the use of surface waves in the geophysical and geotechnical prospecting (Gucunski and Woods, 1991; Park *et al.*, 1998a; Pezeshk and Zarrabi, 2005; Rix *et al.*, 2001; Stokoe and Nazarian, 1983). Such methods rely on the inversion of the observed phase velocities for the shear-wave velocity structure by either using a linearized least square inversion (Rix *et al.*, 2001; Xia *et al.*, 1999; Yuan and Nazarian, 1993), or using evolutionary techniques such as a genetic algorithm or a simulated annealing procedure (Beaty *et al.*, 2002; Luke and Calderón-Macias, 2007; Pezeshk and Zarrabi, 2005; Ryden and Park, 2006; Yamanaka and Ishida, 1996; Zeng, 2011; Hosseini and Pezeshk, 2011a). In either case, due to the nonlinearity of the equations, a nontrivial model null space exists that causes non-unique solutions of the surface wave inversion (Aster *et al.*, 2003; Backus and Gilbert, 1970) where different velocity profiles might have similar phase velocity dispersion curves. A null space is a set of solutions (m_0) that if added to initial solution m, the result of a specific function $f(m)$ does not change, i.e. $f(m+m_0)=f(m)$, such as $\sin(\pi/2+2\pi)=\sin(\pi/2)$ where 2π can be considered as the null space of the model in this case (Aster *et al.*, 2003). Specifically, Backus and Gilbert (1970) state that there is no answer to the question that whether, in a nonlinear problem, there are alternative solutions significantly different from the available one. They clearly indicate that to investigate solutions of a non-unique problem, one must either search for solutions by numerical techniques, or use Monte Carlo methods introduced by Keilis-Borok and Yanovskaya (1967) and Levshin *et al.* (1966). Hence, in the nonlinear inversion of Rayleigh waves there is no objective way to discriminate among all the possible inversion results just by relying on the quality of fit between the observed and inverted dispersion data. Although the non-uniqueness is a well-known issue in surface wave inversion, there have not been systematic efforts to address the issue. Widely-used linearized inversion techniques seek iteratively for a solution that is linearly close to the initial model (Cercato, 2009; Parker, 1994) and does not search automatically for the whole solution space (Stovall, 2010). The degree of the non-uniqueness of the problem directly controls the possibility that the objective function contains the solution as a part of its local minima (Backus and Gilbert, 1970; Cercato, 2009), and there is no absolute treatment to handle such non-uniqueness. In a linearized inversion, several techniques have been proposed by researchers, such as imposing constraints on the velocity variations and inclusion of the higher modes (Cercato, 2007, 2009; Gabriels, 1987; Levshin and Panza, 2006; Park *et al.*, 1999b; Stovall, 2010; Xia *et al.*, 2003). Typically, higher modes are dominant in cases where

a high velocity layer is present, or when the source-array offset increases (Cercato, 2009; Cercato *et al.*, 2010; Stovall, 2010; Tokimatsu *et al.*, 1992; Xia *et al.*, 2002). In the inversion of dispersion data including higher modes, a correct identification of mode numbers is essential (Cercato, 2009; Cerato *et al.*, 2010; Forbriger, 2003a, 2003b; Stovall, 2010; Hosseini and Pezeshk, 2011b, 2011c, 2011d, 2012a; Stovall *et al.,* 2011).

Aforementioned techniques that deal with the non-uniqueness problem deal more with the numerical solutions that implements a larger portion of the dispersion data in the inversion process. Along with these techniques, there have been efforts to bring another source of verification by using synthetic time series. Malagnini (1996) and Malagnini *et al.* (1995) inverted dispersion curves from a shallow explosion, and verified the reliability of the inverted shear-wave velocity profile by comparing the observed and the associated synthetic time series. It has been proven that seismograms can hold information regarding the properties of soil layers, and in the context of seismology and exploration, there has been extensive research on the waveform inversion through which the compressional and shear-wave velocities, and in some cases, density of layers/cells are estimated (Strobbia *et al.*, 2012; Zeng, 2011; Tran and Hiltunen, 2012; Groos, 2013).

In this study, a seismogram synthesis technique (Wang and Herrmann, 1980) is used to discriminate among several profiles emerging from the inversion of phase-velocity dispersion curves obtained at a site near Memphis, Tennessee. Regarding the contrast between the embayment soft deposits and the surrounding firmer medium, the amplifying effect of the shallow soil profile is of great importance in the sedimentary deposits of Mississippi embayment (Cramer, 2006; Kramer, 1996; Pujol *et al.*, 2002; Taborda, 2013). The importance of an accurate estimation of the shear-wave velocity profile is in the site response analysis, while otherwise unsatisfactory and often-dangerous results may emerge (Boaga *et al.*, 2012). For this study, a multi-channel analysis of surface waves (MASW) (Park *et al.*, 1999a; Xia *et al.*, 1999a, 1999b) and a downhole seismic survey are conducted. Phase velocity dispersion data from the MASW test are inverted for several high-resolution shear-wave velocity profiles, and then synthetic seismograms are used to find the velocity profile with a minimum error between the synthetics and the observed time series recorded at each surface geophone (Hosseini and Pezeshk, 2012b, 2012c). Then, the final shear-wave velocity profile from the seismogram match is compared with that from the downhole seismic survey, to validate the effectiveness of the proposed technique in identifying the most appropriate velocity profile among a pool of shear-wave velocity structures, inverted through a non-unique process.

In the next section, the equation of motion is introduced and details are provided on how the problem of the wave propagation in a homogeneous half-space is formulated, and how it contains compressional and transverse waves.

2.1   Equation of Motion

Considering small deformations, the strain tensor from Eulerian and Lagrangian descriptions becomes the same (Pujol, 2003) and the infinitesimal strain tensor can be expressed as:

$$\varepsilon_{kl} = \frac{1}{2}\left(u_{k,l} + u_{l,k}\right) \tag{2.1}$$

where ε_{kl} is Cauchy's strain tensor, and $u_{i,j}$ is the derivative of displacement in direction i with respect to j direction. Hereafter, the comma sign means derivative with respect to the direction mentioned right after the comma. Also, the equation of motion can be approximated by neglecting spatial derivatives of u, *which* becomes:

$$\tau_{ij,j} + \rho f_i = \rho \frac{\partial^2 u_i}{\partial t^2} = \rho \ddot{u}_i \tag{2.2}$$

where τ_{ij} is the stress tensor holding normal and shearing stresses, ρ is the density of the medium, f is the body force per unit volume, t is the time, and finally double dots indicates a second derivative with respect to time.

A three-dimensional representation of stress tensors on an infinitesimal cube is presented in Figure 2.1. It is very common to express a stress symbol with σ_{ii} when the direction of force and the normal axis of the plane that the stress acts on are in the same direction. It is common to distinguish the Cartesian axis with numbers 1, 2, and 3 indicating directions X, Y, and Z. Therefore, in symbol τ_{ij}, i and j can be replaced with numbers from 1 to 3, and with this convention τ_{ij} can represent any type of stress in the tensor:

$$\tau = \begin{bmatrix} \tau_{xx}(=\sigma_{xx}) & \tau_{xy} & \tau_{xz} \\ \tau_{yx} & \tau_{yy}(=\sigma_{yy}) & \tau_{yz} \\ \tau_{zx} & \tau_{zy} & \tau_{zz}(=\sigma_{zz}) \end{bmatrix} = \begin{bmatrix} \tau_{11} & \tau_{12} & \tau_{13} \\ \tau_{21} & \tau_{22} & \tau_{23} \\ \tau_{31} & \tau_{32} & \tau_{33} \end{bmatrix} \tag{2.3}$$
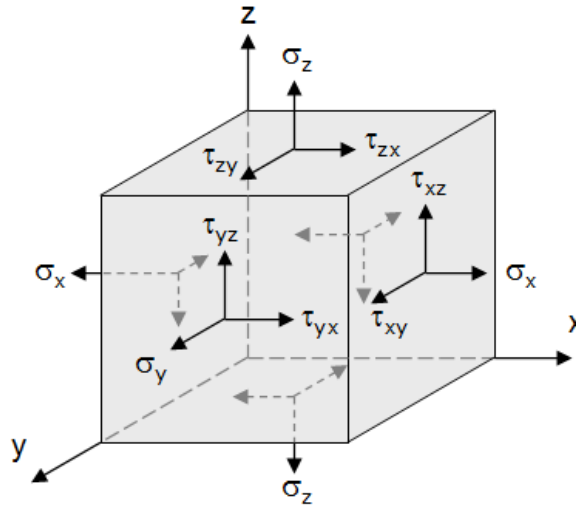

Figure 2.1. Stress tensor presented on an infinitesimal cube.

7

2.1.1   Strain-Stress Relationship and the Equation of Motion

Equation (2.1) relates displacement and strain, and Equation (2.2) relates the displacement with stress. By considering the approximation in deriving these sets of equations, they are valid for any continuous medium. To establish detailed behavior of the wave propagation in a specific medium, we should then introduce the relationship between stress and strain. Such a relationship is expressed using Hooke's law, which relates the deformations to exerted forces. The generalized version of Hooke's law was established by Cauchy (Pujol, 2003; Timoshenko, 1953) as:

$$\tau_{kl} = c_{klpq}\varepsilon_{pq} \tag{2.4}$$

where c_{klpq} is the fourth-order tensor related to properties of the medium, and its reaction to different type of waves and different directions and positions. In general, c_{klpq} has 81 components, which is reduced to 36 after considering the symmetry of stress and strain.

In earth sciences, the tensor c_{klpq} can be simplified even more by assumptions such as that the properties of the medium are the same in any direction (isotropic material). In such case, c_{klpq} for an isotropic solid reduces to:

$$c_{ijkl} = \lambda\delta_{ij}\delta_{kl} + \mu(\delta_{ik}\delta_{jl} + \delta_{il}\delta_{jk}) \tag{2.5}$$

where λ and μ are the Lamé constants, and δ_{ij} is the Kronecker delta function defined as:

$$\delta_{ij} = \begin{cases} 1 & \text{if } i = j \\ 0 & \text{if } i \neq j \end{cases} \tag{2.6}$$

Lamé constants are material properties and are related to other parameters for material properties in engineering and seismology. In seismology, shear and compressional wave velocities (V_P and V_S) are related to Lamé constants by the following equations:

$$V_P = \sqrt{\frac{\lambda + 2\mu}{\rho}} = \alpha$$
$$V_S = \sqrt{\frac{\mu}{\rho}} = \beta \tag{2.7}$$

In engineering, the bulk modulus (K), Young's Modulus (E), and the Poisson's ratio (ν) can be defined as:

$$E = \frac{\mu(3\lambda + 2\mu)}{\mu + \lambda} = \frac{\rho V_S^2 (3V_P^2 - 4V_S^2)}{V_P^2 - V_S^2}$$

$$K = \lambda + \frac{2}{3}\mu = \rho(V_P^2 - \frac{4}{3}V_S^2) \qquad (2.8)$$

$$\nu = \frac{\lambda}{2(\lambda + \mu)} = \frac{V_P^2 - 2V_S^2}{2(V_P^2 - V_S^2)}$$

To do more manipulations on the equation of motion, a series of mathematical operators are defined in Table 2.1. Referring back to the Equation (2.4), the stress and strain relationship can be explicitly defined as:

$$\tau_{ij} = \lambda \delta_{ij} \varepsilon_{kk} + 2\mu \varepsilon_{ij} \qquad (2.9)$$

Now, we can use Equation (2.9) to rewrite the equation of motion (2.2) as:

$$\frac{\partial \tau_{ij}}{\partial x_j} + f_i = \rho \frac{\partial^2 u_i}{\partial t^2} \qquad (2.10)$$

Table 2.1. Mathematical operators used in the study to set up the equation of motion

Operator Name	Equation
Differential Operator	$\nabla = \dfrac{\partial}{\partial x}\mathbf{e}_1 + \dfrac{\partial}{\partial y}\mathbf{e}_2 + \dfrac{\partial}{\partial z}\mathbf{e}_3$
Gradient	$\nabla f = \dfrac{\partial f}{\partial x}\mathbf{e}_1 + \dfrac{\partial f}{\partial y}\mathbf{e}_2 + \dfrac{\partial f}{\partial z}\mathbf{e}_3$
Divergence	$\nabla \cdot f = \dfrac{\partial f}{\partial x} + \dfrac{\partial f}{\partial y} + \dfrac{\partial f}{\partial z}$
Curl	$\nabla \times f = \begin{vmatrix} i & j & k \\ \dfrac{\partial}{\partial x} & \dfrac{\partial}{\partial y} & \dfrac{\partial}{\partial z} \\ f_x & f_y & f_z \end{vmatrix} = \left(\dfrac{\partial f_z}{\partial y} - \dfrac{\partial f_y}{\partial z}\right)\mathbf{e}_1 + \left(\dfrac{\partial f_x}{\partial z} - \dfrac{\partial f_z}{\partial x}\right)\mathbf{e}_2 + \left(\dfrac{\partial f_y}{\partial x} - \dfrac{\partial f_x}{\partial y}\right)\mathbf{e}_3$
Laplacian	$\nabla^2 f = \nabla \cdot \nabla f = \dfrac{\partial^2 f}{\partial x^2}\mathbf{e}_1 + \dfrac{\partial^2 f}{\partial y^2}\mathbf{e}_2 + \dfrac{\partial^2 f}{\partial z^2}\mathbf{e}_3$

where **e** stands for the unit vector. By using Equations (2.9) and (2.1) and the definitions provided in Table 2.1, the equation of motion can be introduced in a vector format as:

$$\mu \nabla^2 \mathbf{u} + (\lambda + \mu) \nabla (\nabla \cdot \mathbf{u}) + \rho \mathbf{f} = \rho \frac{\partial^2 \mathbf{u}}{\partial t^2} \qquad (2.11)$$

Expanding Equation (2.11) further using $\nabla^2 \mathbf{u} = \nabla(\nabla \cdot \mathbf{u}) - \nabla \times (\nabla \times \mathbf{u})$, the equation of motion gets the following form:

$$\frac{(\lambda + \mu)}{\rho} \nabla (\nabla \cdot \mathbf{u}) - \frac{\mu}{\rho} \nabla \times \nabla \times \mathbf{u} + \mathbf{f} = \frac{\partial^2 \mathbf{u}}{\partial t^2} \qquad (2.12)$$

Finally, using Equation set (2.7), one will get the Navier's elastic wave equation:

$$\alpha^2 \ \nabla(\nabla \cdot \mathbf{u}) - \beta^2 \ \nabla \times \nabla \times \mathbf{u} + \mathbf{f} = \frac{\partial^2 \mathbf{u}}{\partial t^2} = \ddot{\mathbf{u}} \qquad \text{(in time)} \qquad (2.13)$$

$$\alpha^2 \ \nabla(\nabla \cdot \mathbf{u}) - \beta^2 \ \nabla \times \nabla \times \mathbf{u} + \mathbf{f} = i\omega^2 \mathbf{u} \qquad \text{(in frequency)} \qquad (2.14)$$

where the double dot on the right-hand side of Equation (2.13) means a second derivative with respect to time, and Equation (2.14) is in the frequency domain form. Note that Equation set (2.13) contains two type of propagating waves: dilatational (first term from left) and rotational (second term from left), corresponding to P and S waves. The equation of motion can also be presented as the following form, to match the notation of Ben-Menahem and Singh (1981, Section 4.1), for an applied force at depth z_0:

$$\alpha^2 \ \nabla(\nabla \cdot \mathbf{u}) - \beta^2 \ \nabla \times \nabla \times \mathbf{u} - \frac{\partial^2 \mathbf{u}}{\partial t^2} = -\mathbf{S}_0 g(t)\delta(z - z_0) \qquad \text{(in time)} \qquad (2.15)$$

$$\alpha^2 \ \nabla(\nabla \cdot \mathbf{u}) - \beta^2 \ \nabla \times \nabla \times \mathbf{u} - i\omega^2 \mathbf{u} = -\mathbf{S}_0 g(\omega)\delta(z - z_0) \qquad \text{(in frequency)}$$

where term $\mathbf{S}_0 \ g(t) \ \delta(z\text{-}z_0)$ represents the body force per unit mass, which is a force of a specific magnitude in different directions ($\mathbf{S}_0$), concentrated at the depth $z=z_0$, and $g(t)$ is a dimensionless function time variation of the force, and $g(\omega)$ is the Fourier transform of $g(t)$. Displacement vector **u** which is the solution to Equation (2.15), can be expressed as (Pujol, 2003):

$$\mathbf{u}(\mathbf{r},t) = h(t - \mathbf{k}.\mathbf{r}/c) + g(t + \mathbf{k}.\mathbf{r}/c) \qquad (2.16)$$

where h and g are functions that travel forward and backward in time, t is time, c is the propagation velocity, **r** is the vector of location, and k is defined as a unit vector ($|\mathbf{k}| = 1$) equal to ($k_x.\mathbf{x}$, $k_y.\mathbf{y}$, $k_z.\mathbf{z}$). Pujol (2003) noted that for a given value of t, u(**r**,t) is constant for all locations (x, y, and z) that **k.r** is a constant value such as C. In such case, equation **k.r** = C

is the wave front of plane waves presented by Equation (2.16). Therefore plane waves have a normal vector **k**, which is called wavenumber vector defining the wave fronts.

2.1.2   Potentials

The wave equation in Equation set (2.13) can be studied in terms of the type of waves that it produces. It is convenient to apply divergence operator to the equation of motion (2.13):

$$\alpha^2\ \nabla\cdot\nabla(\nabla\cdot\mathbf{u})-\beta^2\ \nabla\cdot\nabla\times\nabla\times\mathbf{u}+\tilde{\mathbf{f}}=\frac{\partial^2\left(\nabla\cdot\mathbf{u}\right)}{\partial t^2} \tag{2.17}$$

where $\tilde{\mathbf{f}}$ is the body force vector after divergence operator is applied to. Knowing that $\nabla\cdot\nabla\times\nabla\times\mathbf{u}$ equals zero, then one can define $\varphi=\nabla\cdot\mathbf{u}$ as the P wave potential since the divergence operator calculates the outward flux of a vector field from an infinitesimal volume around a given point, and Equation (2.17) reduces to the familiar form of a vibrating string:

$$\alpha^2\ \nabla\cdot\nabla\left(\varphi\right)=\frac{\partial^2\left(\varphi\right)}{\partial t^2}$$
$$\Rightarrow\ \nabla^2\left(\varphi\right)=\frac{1}{\alpha^2}\frac{\partial^2\left(\varphi\right)}{\partial t^2} \tag{2.18}$$

The same way, curl operator is applied to the Equation (2.15). At every point in the field, the curl of that field is represented by a vector. The attributes of this vector (the length and the direction) characterize the rotation at that point. Applying the curl operator to the equation of motion will result in:

$$\alpha^2\ \nabla\times\nabla(\nabla\cdot\mathbf{u})-\beta^2\ \nabla\times\nabla\times\nabla\times\mathbf{u}+\hat{\mathbf{f}}=\frac{\partial^2\left(\nabla\times\mathbf{u}\right)}{\partial t^2} \tag{2.19}$$

where $\hat{\mathbf{f}}$ is the body force vector after the divergence operator. Knowing that $\nabla\times\nabla(\nabla\cdot\mathbf{u})$ equals zero, and that $\nabla\times\nabla\times\mathbf{X}=\nabla\times\nabla\cdot\mathbf{X}-\nabla\cdot\nabla\cdot\mathbf{X}$ for every vector **X**, then Equation (2.19) reduces to:

$$\beta^2\ \nabla.\nabla(\nabla\times\mathbf{u})=\frac{\partial^2\left(\nabla\times\mathbf{u}\right)}{\partial t^2} \tag{2.20}$$

and after defining $\boldsymbol{\psi}=\nabla\times\mathbf{u}$ as the S wave potential, an equation similar to the P wave potential will be obtained as:

$$\nabla^2(\mathbf{\psi}) = \frac{1}{\beta^2}\frac{\partial^2(\mathbf{\psi})}{\partial t^2} \qquad (2.21)$$

The curl operator is a vector operator that describes the infinitesimal rotation of a three-dimensional vector field.

Based on the discussion above, the general equation of motion possesses two types of propagating waves at the same time, one moving in the direction of the propagation (φ potential), and one moving in the perpendicular direction of the propagation ($\mathbf{\psi}$ potential). The φ potential was obtained using the divergence operator and is related to P waves propagating with the speed of α. In the same way for the $\mathbf{\psi}$ potential, it was obtained using the curl operator and is related to S waves propagating with the speed of β. It is possible to show that the $\mathbf{\psi}$ potential can be decomposed further into two normal directions (each still perpendicular to the direction of the propagation, i.e., SH and SV). Interested readers can find more details on the topic in Aki and Richards (1980), Ben-Menahem and Singh (1981), and Pujol (2003).

Solving Equation (2.13) for a homogeneous half-space (where the material property does not change in any direction) has been studied in detail (Aki and Richards, 1980; Ben-Menahem and Singh, 1981). However, earth usually is considered as layers stacked on top of each other, where the property of material is the same in the horizontal direction and only changes with depth (z). The equation of motion in a multi-layered earth system is introduced in the next section, and important aspects of heterogeneity are presented.

2.1.3   Surface Waves in Heterogeneous Media

The equation of motion (Equation 2.13) carries all components of motion. These components can be broken down into deformation in the direction of the wave propagation (x_1), and perpendicular to the propagation direction (x_2 and x_3). These displacements are referred to respectively as P, SV, and SH waves, and can be studied in term of potentials (Aki and Richards, 1980). In this study, the direction of the x_3 axis (z in Cartesian and z in spherical coordinates) is downward, the direction of the x_1 axis (z in Cartesian and r in spherical coordinates) is horizontal to the right, and the direction of the x_2 axis (y in Cartesian and θ in spherical coordinates) is perpendicular to the plane of x_1 and x_2 axes.

On the surface of a heterogeneous half-space, a series of waves are generated that attenuate with depth and are called surface waves. There are two types of surface waves: Rayleigh waves and Love waves. Rayleigh waves have an elliptical motion and are the result of the interaction between P and SV components. Love waves exist due to the SH component of the motion. The equation of motion can be analyzed further by making assumptions for deformation functions for displacements in different directions. For non-zero displacements, it can be shown that the solution to Equation (2.13) can be expressed in the following oscillatory format:

$$u(\mathbf{x},t) = \mathbf{A}e^{i(\omega t - \mathbf{kx})} \qquad (2.22)$$

where **x** and **k** are the position and the wavenumber vectors. It should be noted that vector **A** represents the direction of ground motion and vector **k** represents the direction of propagation.

2.1.3.1 Rayleigh Waves

The system of coordination is defined similar to the case of Love waves in the previous section. Similar to the previous section, one can express the following relationship for a Rayleigh waves motion-stress vector by defining the following displacement vectors:

$$
\begin{aligned}
u_x &= r_1(k, z, w)\exp\left[i(kx - \omega t)\right] \\
u_y &= 0 \\
u_z &= ir_2(k, z, w)\exp\left[i(kx - \omega t)\right]
\end{aligned}
\tag{2.23}
$$

Please note that Equation set (2.23) is providing components of the displacement vector satisfying equation of motion in Equation (2.15) and is presented as $\mathbf{u} = u_x\mathbf{e}_1 + u_y\mathbf{e}_2 + u_z\mathbf{e}_3$. From Equations (2.23) and (2.2), stress components are calculated as:

$$
\begin{aligned}
\tau_{yz} &= \tau_{xy} = 0 \\
\tau_{xx} &= i\left[\lambda\frac{dr_2}{dz} + k(\lambda + 2\mu)r_1\right]\exp\left[i(kx - \omega t)\right] \\
\tau_{yy} &= i\left[\lambda\frac{dr_2}{dz} + k\lambda r_1\right]\exp\left[i(kx - \omega t)\right] \\
\tau_{zz} &= i\left[(\lambda + 2\mu)\frac{dr_2}{dz} + k\lambda r_1\right]\exp\left[i(kx - \omega t)\right] \\
\tau_{zx} &= \mu\left[\frac{dr_1}{dz} - kr_2\right]\exp\left[i(kx - \omega t)\right]
\end{aligned}
\tag{2.24}
$$

Since stress components τ_{zx} and τ_{zz} are continuous in the z direction, one can rewrite them as a function of two new terms:

$$
\begin{aligned}
\tau_{zx} &= r_3(k, z, w)\exp\left[i(kx - \omega t)\right] \\
\tau_{zz} &= ir_4(k, z, w)\exp\left[i(kx - \omega t)\right]
\end{aligned}
\tag{2.25}
$$

In Equation (2.23), the imaginary *i* factor is introduced in the vertical displacement to account for the π/2 shift, with the horizontal displacement modeling the elliptical motion of Rayleigh

waves. The differential equations for the motion-stress vector $(r_1\ r_2\ r_3\ r_4)^{\mathrm{T}}$ are obtained from Equations (2.23) to (2.25):

$$\frac{d}{dz}\begin{pmatrix} r_1 \\ r_2 \\ r_3 \\ r_4 \end{pmatrix} = \begin{pmatrix} 0 & k & m^{-1}(z) & 0 \\ -k\,l(z)\big[\,l(z)+2m(z)\big]^{-1} & 0 & 0 & \big[\,l(z)+2m(z)\big]^{-1} \\ k^2 x(z) - w^2 r(z) & 0 & 0 & k\,l(z)\big[\,l(z)+2m(z)\big]^{-1} \\ 0 & -w^2 r(z) & -k & 0 \end{pmatrix}\begin{pmatrix} r_1 \\ r_2 \\ r_3 \\ r_4 \end{pmatrix} \tag{2.26}$$

where $\xi(z) = 4\mu(z)[\lambda(z)+\mu(z)]/[\lambda(z)+2\mu(z)]$. The above equation in presented in Aki and Richards (1980) [AR80] and Ben-Menahem and Singh (1981) [BS81]. Care should be taken in comparing the two notations since the order of variable are different:

$$\begin{pmatrix} r_1 \\ r_2 \\ r_3 \\ r_4 \end{pmatrix}_{AR80} = \begin{pmatrix} y_1 \\ y_3 \\ y_2 \\ y_4 \end{pmatrix}_{BS81} \tag{2.27}$$

2.1.4   Dispersion of Rayleigh Waves and Synthetic Seismogram

This study only focuses on Rayleigh waves. In this section, a systematic approach is introduced to analyze displacements and tractions in a heterogeneous half-space for the combined effect of P and SV waves. The dispersive properties of a heterogeneous half-space medium can also be calculated as a secondary result of the analysis. Boundary conditions for Rayleigh waves is zero traction at the surface and zero displacement at the infinite depth:

$$\begin{aligned} r_3, r_4 &\to 0 \quad \text{as } z = 0 \text{ (free surface)} \\ r_1, r_2 &\to 0 \quad \text{as } z \to \infty \end{aligned} \tag{2.28}$$

Equation (2.26) is in the form of:

$$\frac{d\mathbf{f}(z)}{dz} = \mathbf{A}(z)\mathbf{f}(z) + \mathbf{s}\delta(z - z_0) \tag{2.29}$$

where $\mathbf{f}(z)=[r_1\ r_2\ r_3\ r_4]^{\mathrm{T}}$ is the motion-stress vector for a specific layer and $\mathbf{s}=[\,s_1^R\ s_2^R\ s_3^R\ s_4^R\,]$. There are two methods to deal with Equation (2.29): (1) to solve the inhomogeneous Equation (2.26); or (2) to solve the homogeneous version of (2.29) by putting $\mathbf{s}=0$, and applying the following source condition:

$$\mathbf{f}(z+0) - \mathbf{f}(z-0) = \mathbf{s} \tag{2.30}$$

The latter method avoids the direct calculation of the complicated parameters (Ben-Menahem and Singh, 1981), which follows in the rest of this section.

In Equation (2.29), matrix $\mathbf{A}(z)$ is a 4 by 4 matrix in the (x,z) plane (for the case of Rayleigh waves as in Equation 2.30) and is a 2 by 2 matrix. Matrix $\mathbf{A}(z)$ is constant for each isotropic layer in a heterogeneous system at a fixed depth. Using the Jordan decomposition of the motion-stress vector $\mathbf{f}(z)$ (Gantmatcher 1960; Turnbull and Aitken 1952), it is possible to rewrite it for Rayleigh waves as in Wang and Herrmann (1980):

$$\mathbf{f}(z) = \mathbf{F}\mathbf{w} = \mathbf{F}\begin{pmatrix} P_u \\ S_u \\ P_d \\ S_d \end{pmatrix} \tag{2.31}$$

where $\mathbf{w}$ is the wave-vector containing up-going and down-going wave types. The reason to decompose the motion stress vector $\mathbf{f}(z)$ to up going and down going waves is that some of the boundary conditions in heterogeneous media are imposed by suppressing certain type of waves at infinity $(z \to \infty)$, not just by limitations on the stress and strains. Therefore, motion-stress vector should be decomposed in the way introduced in Equation (2.31) and relate it to the wave-vector so the boundary conditions can be applied. Matrix $\mathbf{F}$ is made up from eigenvectors of $\mathbf{A}(z)$ times a matrix containing the vertical phase vectors (Aki and Richards, 1980):

$$\mathbf{F} = \mathbf{E}\mathbf{\Lambda}(z)$$

$$\mathbf{E} = \omega^{-1}\begin{pmatrix} \alpha k & \beta v & \alpha k & \beta v \\ \alpha \gamma & \beta k & -\alpha \gamma & -\beta k \\ -2\alpha \mu k \gamma & -\beta \mu (k^2 + v^2) & 2\alpha \mu k \gamma & \beta \mu (k^2 + v^2) \\ -\alpha \mu (k^2 + v^2) & -2\beta \mu k \gamma & -\alpha \mu (k^2 + v^2) & -2\beta \mu k \gamma \end{pmatrix}$$

$$\mathbf{\Lambda}(z) = \begin{pmatrix} e^{-\gamma z} & 0 & 0 & 0 \\ 0 & e^{-vz} & 0 & 0 \\ 0 & 0 & e^{\gamma z} & 0 \\ 0 & 0 & 0 & e^{vz} \end{pmatrix} \tag{2.32}$$

where $v = \sqrt{k^2 - \omega^2 / \beta^2}$ and $\gamma = \sqrt{k^2 - \omega^2 / \alpha^2}$, and therefore, the final form can be obtained:

$$\mathbf{f}(z) = \mathbf{E}\mathbf{\Lambda}(z)\mathbf{w} \tag{2.33}$$

In a layered media, there are motion-stress vectors $\mathbf{f}(z)$ for each layer as a function of depth (z) for the same layer. Motion-stress vectors connect to each other at different layers by the boundary conditions and assumption of tractions and displacements continuity at the interface

between the layers. Therefore, if one starts from a specific layer and is able to move (recalculate) the motion-stress vector $\mathbf{f}(z)$ to a different depth in any layer, then the problem of finding the displacement in a heterogeneous half-space (synthesis of seismogram) is complete in frequency and wavenumber domain.

It will be shown that if no source of energy (external displacement or traction) is considered in such an approach, then one can find the pair of matching frequency-wavenumber through the process which yields the theoretical Rayleigh wave dispersion curve. Synthesis of seismogram goes a step further when a source of energy in an arbitrary depth can be implemented in the process of moving the motion-stress vector (as described above), and yield vertical and horizontal displacements which later are inverse-transformed into time and space domains.

A schematic view of the above concept is presented in Figure 2.2, in terms of involved matrices. Some of the matrices are not introduced yet, but will be introduced later.

In Figure 2.2, among the introduced vectors and matrices, $\mathbf{w}$ and the stress-motion vector $\mathbf{f}(z)$ are unknowns. It is important to note that for Rayleigh waves, introduced boundary conditions are presented as zero stress at the surface, continuous stress and deformation at boundaries, and no up-going wave field in half-space; which leads to the following sets of equations as shown on the boundary conditions column in Figure 2.2:

$$\mathbf{f}_1(z=0)=[r_1\ r_2\ r_3\ r_4]^{\mathrm{T}}=[r_1\ r_2\ 0\ 0]^{\mathrm{T}}$$
$$\mathbf{f}_i\left(z=h_i\right)=\mathbf{f}_{i+1}\left(z=0\right);\ \text{where}\ i=1\cdots N \qquad (2.34)$$
$$\mathbf{w}_{N+1}=[P_\mathrm{u}\ S_\mathrm{u}\ P_\mathrm{d}\ S_\mathrm{d}]^{\mathrm{T}}=[0\ 0\ P_\mathrm{d}\ S_\mathrm{d}]^{\mathrm{T}}$$

The goal is to relate the wave-vector ($\mathbf{w}_{N+1}$) in half-space to deformations at the surface: $\mathbf{f}_1(z=0)$. Based on Equation (2.33), for a specific layer i, one can relate the top and bottom deformations of the same layer as:

$$\mathbf{f}_i\left(z_t\right)=\mathbf{E}_i\mathbf{\Lambda}_i(z_t)\mathbf{w}_i \qquad \text{(top)}$$
$$\mathbf{f}_i\left(z_b\right)=\mathbf{E}_i\mathbf{\Lambda}_i(z_b)\mathbf{w}_i \qquad \text{(bottom)} \qquad (2.35)$$

where z_t and z_b are the vertical local coordinates (Figure 2.2) at each layer for the top and bottom depths that the stress-motion vector is calculated. After eliminating the wave-vector from Equation (2.35), then the Thompson-Haskell propagation matrix (a) (Haskell, 1953; Wang and Herrmann, 1980) for each layer is defined to relate the stress-motion vector at the bottom (z_b) of the ith layer to the one at the top (z_t):

$$\mathbf{a}_i=\mathbf{E}_i\mathbf{\Lambda}_i(h_i)\mathbf{E}_i^{-1}$$
$$\mathbf{f}_i\left(z_b\right)=\mathbf{a}_i\mathbf{f}_i\left(z_t\right) \qquad (2.36)$$

where h_i is the thickness of the ith layer. As illustrated in Figure 2.2, deformations and tractions at the top of each layer are transferred to the bottom of that layer by multiplying it by the propagator matrix. Since the deformation and stresses are equal at the boundaries, then:
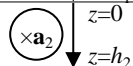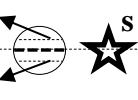
$$\mathbf{f}_{i+1} = \mathbf{a}_i \mathbf{f}_i \qquad (2.37)$$

where the motion-stress vector is calculated at the top of every layer. Now, deformations at the surface can be related to the wave-vector at the half-space with the following recursive Equation:

$$\mathbf{f}_{N+1} = \mathbf{a}_N \mathbf{a}_{N-1} \ldots \mathbf{a}_2 \mathbf{a}_1 \mathbf{f}_1 \qquad (2.38)$$

and from Equation (2.33):

$$\mathbf{E}_{N+1} \mathbf{\Lambda}_{N+1} \mathbf{w}_{N+1} = \mathbf{a}_N \mathbf{a}_{N-1} \ldots \mathbf{a}_2 \mathbf{a}_1 \mathbf{f}_1 \qquad (2.39)$$

Layer Properties/Matrices	Motion-Stress Propagator	Interface No.	Layer No.	Boundary Conditions

$h_1, \alpha_1, \beta_1, \mathbf{E}_1, \mathbf{\Lambda}_1(z), \mathbf{f}_1(z), \mathbf{w}_1$ $\times\mathbf{a}_1$ $z=0$ $z=h_1$

$h_2, \alpha_2, \beta_2, \mathbf{E}_2, \mathbf{\Lambda}_2(z), \mathbf{f}_2(z), \mathbf{w}_2$ $\times\mathbf{a}_2$ $z=0$ $z=h_2$

$\mathbf{f}_{m+1}^{-}$ $\mathbf{s}$ $\mathbf{E}_m, \mathbf{\Lambda}_m(z), \mathbf{f}_m(z)$

$\mathbf{f}_{m+1}^{+}$ $\mathbf{E}_{m+1}, \mathbf{\Lambda}_{m+1}(z), \mathbf{f}_{m+1}(z)$ Source Interface

$h_N, \alpha_N, \beta_N, \mathbf{E}_N, \mathbf{\Lambda}_N(z), \mathbf{f}_N(z), \mathbf{w}_N$ $\times\mathbf{a}_N$ $z=0$ $z=h_N$

$\infty, \alpha_{N+1}, \beta_{N+1}, \mathbf{E}_{N+1}, \mathbf{\Lambda}_{N+1}(z), \mathbf{f}_{N+1}(z), \mathbf{w}_{N+1}$

★ : Source

Interface No.: 0, 1, 2, ..., m-1, m, m+1, ..., N-1, N

Layer No.: 1, 2, ..., m, m+1, ..., N, N+1

Boundary Conditions:

$\mathbf{f}_1(z=0)=[r_1\ r_2\ r_3\ r_4]^{\mathrm{T}} =[r_1\ r_2\ 0\ 0]^{\mathrm{T}}$

$\mathbf{f}_1(z=h_1)= \mathbf{f}_2(z=0)$

$\mathbf{f}_2(z=h_2)= \mathbf{f}_3(z=0)$

$\mathbf{f}_m(z=h_m)= \mathbf{f}_{m+1}(z=0) + \mathbf{s}$

$\mathbf{f}_{N-1}(z=h_{N-1})= \mathbf{f}_N(z=0)$

$\mathbf{f}_N(z=h_N)= \mathbf{f}_{N+1}(z=0)$

$\mathbf{w}_{N+1}=[P_{\mathrm{u}}\ S_{\mathrm{u}}\ P_{\mathrm{d}}\ S_{\mathrm{d}}]^{\mathrm{T}} =[0\ 0\ P_{\mathrm{d}}\ S_{\mathrm{d}}]^{\mathrm{T}}$

Figure 2.2. Heterogeneous system along with its associated matrices.

2.2 Point Force Source and Motion-Stress Vector

A dislocation source across an arbitrarily orientated plane can be expressed by a system of forces that generates an identical radiation field (Kennett and Kerry, 1979). Hudson (1969) showed that a point force across an arbitrary plane can be expressed as dislocations across a horizontal plane. As Kennett and Kerry (1979) state, it is then possible to express a point force by its equivalent discontinuities in displacement and traction across that plane, i.e. there will be a discontinuity in the motion-stress vector. In the case of this study, only point force is the focus and is the same technique as employed by Wang and Herrmann (1980), and Aki and Richards (2002).

It should be mentioned that this technique also has an alternative, which instead of modeling equivalent discontinuity in displacement and stress, rise is given to discontinuity to wave-vector **w** (Kennett and Kerry, 1979). This alternative technique is used by Kennett and Kerry (1979) and Haskell (1964) which is not the focus of this study.

Aki and Richards (1981) and Kennett and Kerry (1979) provides details on how to estimate the discontinuity in the motion-stress vector **f** from a point source with temporal oscillation. Section 7.4.2 from Aki and Richards (1981) provides details on how to calculate such discontinuity from a point source expressed in the frequency domain with **F** $\exp(-i\omega t)$ where **F**=$[F_x \quad F_y \quad F_z]$. With such definition of the point force, the force per unit volume at the plane of the source is related to stress change in bottom and top of that plane:

$$\mathbf{T}(h+0) - \mathbf{T}(h-0) = -\mathbf{F}\exp(-i\omega t)\delta(x)\delta(y) \tag{2.40}$$

where **T** is the traction acting on the horizontal plane. The discontinuity in the traction should be estimated for all azimuthal model numbers (Aki and Richards, 1981; Haskell, 1964) which eventually are expressed as following (Aki and Richards, 1981) for Bessel order number (azimuthal model number) equal to zero:

$$\mathbf{s}_0 = \begin{bmatrix} 0 & 0 & F_z & 0 \end{bmatrix} \tag{2.41}$$

For Bessel order numbers (azimuthal model numbers) equal to +1 or -1, the motion-stress vector discontinuity can be expressed as:

$$\mathbf{s}_{\pm 1} = \begin{bmatrix} 0 & 0 & 0 & \frac{1}{2}\left(\mp F_x + iF_y\right) \end{bmatrix} \tag{2.42}$$

This results from Aki and Richards (1981) are the same as Kennett and Kerry (1979). In Kennett and Kerry (1979), moment tensor elements M_{xx}, M_{yy}, M_{zz}, M_{yz}, M_{xz}, and M_{xy} should be set to zero and direction of z axis should be reversed to match results from Aki and Richards (1981) presented in their equations (7.126) to (7.129).

2.3 Implementing Attenuation in Seismogram Synthesis

Attenuation is a measure of energy loss as seismic waves travel through the dissipative medium. Mathematical approaches have shown that attenuation causes absorption and dispersion. This can lead to complication of the surface wave inversion problem, where the observed dispersion is not only a function of material heterogeneity, but also a function of attenuation of the medium. The focus of this section is on the Futterman (1962) operator. To develop mathematical formulations related to absorption and dispersion, it is best to start with a one-dimensional plane wave displacement amplitude equation:

$$u(x,t) = A\exp(-\alpha(\omega)x)\exp\left[i\left(kx - \omega t\right)\right] \tag{2.43}$$

where $u(x,t)$ is the medium displacement, A is the amplitude of the wave, x is the location of the observation, t is the time of observation, k is the wavenumber, ω is the angular frequency, i is the imaginary number, and $\alpha(\omega)$ is the frequency-dependent attenuation factor and should not be mistaken with the compressional wave velocity introduced in the previous section. Following Futterman (1962), Equation (2.43) can be reformulated to represent a complex wavenumber $K(\omega)$:

$$\begin{aligned} u(x,t) &= A\exp\left[i\left(i\alpha(\omega) + k\right)x\right]\exp\left[-i\omega t\right] \\ &= A\exp\left[iK(\omega)x\right]\exp\left[-i\omega t\right] \end{aligned} \tag{2.44}$$

where $K(\omega) = k + i\,\alpha(\omega) = \omega/c_0 + i\,\alpha(\omega)$ is the complex wavenumber, and c_0 is the non-dispersive limit of the phase velocity in the low frequency. To study the dispersive and the absorptive properties for such propagation, the refraction index is introduced which is the ratio of the complex wavenumber to its non-dispersive counterpart:

$$n(\omega) = {K(\omega)}\Big/{K_0(\omega)} \tag{2.45}$$

where $K_0(\omega) = \omega/c_0$ is the non-dispersive wavenumber defined as the case where no attenuation exist (no imaginary term in $K(\omega)$). The refraction index has real ($\mathfrak{Re}.\ n(\omega)$) and imaginary ($\mathfrak{Im}.\ n(\omega)$) components, where the real part is associated with the dispersion, and its imaginary component is associated with the absorption (Futterman, 1962). It has been observed that the absorption coefficient decreases with frequency, and there should be a small frequency ω_0 below which the absorption is negligible. Futterman (1962) showed that this cutoff frequency is arbitrarily selected as a small value and is larger than zero. For frequencies $\omega < \omega_0$ the complex wavenumber becomes $K(\omega) = K_0(\omega) = \omega/c_0$. From now on, the dimensionless variable r is defined by $r = \omega/\omega_0$ (Futterman, 1962).

2.3.1 Dispersion

To decompose the wave propagating in the absorptive medium into different frequencies, the wave displacement amplitude $u(x,t)$ can be written as:

$$u(x,t) = \int_{-\infty}^{\infty} u_\omega(x,t)\, d\omega \tag{2.46}$$

where $u_\omega(x,t)$ is the component of the wave carrying only a single frequency ω. Having real amplitude and phase, $u_\omega(x,t)$ can be expressed as:

$$u_\omega(x,t) = A_\omega(x)\exp(i\phi_\omega)$$
$$A_\omega(x) = A(0)\exp(-\alpha(\omega)x) \tag{2.47}$$
$$\phi_\omega(x,t) = kx - \omega t$$

where A_ω and ϕ_ω are the real amplitude and phase for the single frequency ω. Considering the dependence of the phase with respect to time, t, and position, x, then one can define the phase velocity $c(\omega)$ as the velocity that keeps phase term ϕ_ω constant with variations of t and x. The phase velocity is defined as the variation of distance dx in a specific time change dt while a constant phase is maintained:

$$c(\omega) = \left(\frac{dx}{dt}\right)_{\phi=\text{constant}} = \frac{\omega}{k(\omega)} \tag{2.48}$$

Equation (2.48) can be stated in term of the index factor:

$$c(\omega) = c_0 / \mathscr{R}_e\, n(\omega) \tag{2.49}$$

where the real part of the refraction index is introduced explicitly after the introduction of absorption in the next section. Dispersion is an unavoidable phenomenon as a result of imposing the causality constraint. This means that if no pulse is expected before the arrival time x/c, then the dispersion becomes necessary, as shown by Aki and Richards (1980).

2.3.2 Absorption

It is possible to measure the dissipative properties of the medium in a way that we can relate the attenuation in space to the damping in time. A single-frequency component of displacement is considered:

$$u = A\exp(-\gamma t)\cos(\omega t + \beta) \tag{2.50}$$

where γ is the damping factor and β is the phase. Note that the dissipative term is exp(-γt) in Equation (2.50) which is different from exp(-αx) in Equation (2.43): in the former term γ is damping in time, and in the latter α is the attenuation term in space. Within a period ($t=2\pi/\omega$) the amplitude drops by a factor of:

$$\exp(-2\pi\gamma/\omega) = \exp(-\Delta) \tag{2.51}$$

where Δ is the logarithmic drop in amplitude in one period. The ratio of energy loss per cycle to maximum stored energy in the medium ($\Delta W/W$) forms a basis to define the quality factor, and is also a function of logarithmic amplitude drop:

$$\frac{\Delta W}{W} = \frac{2\pi}{Q} = 1 - \exp(-2\Delta)$$

$$\Rightarrow Q = 2\pi \left[1 - \exp(-2\Delta)\right]^{-1}$$

(2.52)

A sinusoidal approximation of a propagating wave can be expressed as:

$$u_\phi(x,t) = A\exp(-\alpha x)\cos\phi(x,t)$$

(2.53)

where $\phi(x,t)=\omega(x/c - t)$ is the phase. To calculate the logarithmic amplitude drop for one period, one can consider the phase 0 and phase 2π, where the wave is at x and $x + \delta x$ and the amplitude drop becomes (Futterman, 1962):

$$\Delta = 2\pi\alpha c / \omega$$

(2.54)

and from Equation (2.52), the quality factor is expressed as:

$$Q = 2\pi\left[1 - \exp(-4\pi\alpha c / \omega)\right]^{-1}$$

$$\Rightarrow Q \approx \frac{\omega}{2\alpha(\omega)c(\omega)} \quad \text{(if } 4\pi\alpha c / \omega << 1)$$

(2.55)

By defining $Q_0(\omega)=\omega/2\alpha(\omega)c_0$, the intrinsic dependence to frequency happens in the attenuation term. The imaginary part of the refraction index can be expressed as:

$$\mathfrak{Im}.\ n(\omega) = 1/2Q_0(\omega) \tag{2.56}$$

Please note that in the desired frequency range one would like attenuation to be strictly linear; therefore, $\mathfrak{Im}.\ n(\omega)$ and Q_0 are frequency independent. To show the dependency of $\mathfrak{Im}.\ n(\omega)$ with frequency, it is shown that the following definition works fine (Futterman, 1962):

$$\mathfrak{Im}.\ n(\omega)= \frac{1}{2Q_0}\left[1 - \exp(-|r|)\right]\mathrm{sgn}\,r \tag{2.57}$$

In practice by selecting a small cutoff frequency, the exponential term in Equation (2.57) can be ignored and the last sgn term can be neglected by only using positive frequencies. The real part of the refraction index was left to be introduced here as:

$$\mathfrak{Re}.\ n(\omega) =1 - \frac{1}{\pi Q_0}\ln(r) \tag{2.58}$$

Substituting Equation (2.58) into Equation (2.49) will result in (Futterman, 1962; Kanamori and Anderson, 1977):

$$c(\omega) = c_0 \left[1 - \frac{1}{\pi Q_0} \ln(r) \right]^{-1}$$

$$\approx c_0 \left[1 + \frac{1}{\pi Q_0} \ln(\frac{\omega}{\omega_0}) \right]$$

(2.59)

Again, velocity c_0 is the velocity in a low reference frequency ω_0 where $\omega_0 > \omega$. In Equation (2.59) the effect of dispersion on velocity is expressed with respect to the known reference velocity c_0. The same concept can be applied when the reference frequency is at high frequency ω_∞ with velocity c_∞ where $\omega < \omega_\infty$. The attenuation dispersion effect on velocity can be expressed as the following equation, as introduced by Equation (14) of Kanamori and Anderson (1977):

$$c(\omega) = c_\infty \left[1 - \frac{1}{\pi Q_0} \ln(\frac{\omega_\infty}{\omega}) \right]$$

(2.60)

2.3.3 Implementation

Implementation of dispersion and absorption is simply followed by the use of the refraction index in a complex velocity term, as used by Herrmann (1987) in his HPREP96 program (subroutine "aten" in the section "Futterman Causal Q"), and also introduced by Aki and Richards (2002):

$$c(\omega) \approx c_0 \left[\frac{1}{\Re_e.\, n(x)} - \Im_{m.}\, n(x)\, i \right]$$

$$\approx c_0 \left[1 + \frac{1}{\pi Q_0} \ln(x) - \frac{i}{2 Q_0} \right]$$

(2.61)

In this study, the full waveform synthetics are investigated using the software package "Computer Programs in Seismology (CPS)" developed by Herrmann (1987) for a two-layer medium with one layer over half-space. The shear-wave velocity (V_S), the compressional-wave velocity (V_P), layer thickness (H), and density (ρ) along with the quality factor for P and S waves (Q_P and Q_S) are provided in Table 2.2.

Table 2.2. Earth model used to study attenuation effect on synthetic seismogram.

	H (m)	V_P (m/s)	V_S (m/s)	ρ (gm/cc)	Q_P	Q_S
Layers	10.0	500.0	60.0	2.1	20.0	20.0
	∞	800.0	112.0	2.1	20.0	20.0

There are three major programs in the CPS package to run in a Linux environment for successful seismogram generation: HPREP96, HSPEC96, and HPULSE96. Figure 2.3 shows a simple script to run the set of programs:

Details for synthesis are provided in the Robert Herrmann's website (http://www.eas.slu.edu/eqc/eqccps.html, last visited March 2014). In line #4 of Figure 2.3, HPREP96 reads model "end.mod" and distance "dfile" files. Model file "end.mod" represents the earth model introduced in Table 2.2 and is shown in Figure 2.4.

```
#!/bin/bash
HS=0.0                      # Source Depth
HR=0.0                      # Receiver Depth
hprep96 -M end.mod -d dfile  -HS "$HS" -HR "$HR" -ALL          LINE 4
hspec96                                                         LINE 5
hpulse96 -p -V -l 1  |  f96tosac -B                             LINE 6
gsac << EOF                                                     LINE 7
r *Z*F*sac                                                      LINE 8
dif                                                             LINE 9
w                                                              LINE 10
q                                                              LINE 11
EOF                                                            LINE 12
```

Figure 2.3. Script using CPS package to generate synthetic seismogram.

```
MODEL.01
Model after    11 iterations
ISOTROPIC
KGS
FLAT EARTH
1-D
CONSTANT VELOCITY
LINE08
LINE09
LINE10
LINE11
H(KM)   VP(KM/S) VS(KM/S) RHO(GM/CC)   QP   QS    ETA    ETAS   FREFP   FREFS
0.0100   0.5002   0.0600   2.1000     0.0  0.0   0.00   0.00   10.00   10.00
0.0000   0.8002   0.1121   2.1000     0.0  0.0   0.00   0.00   10.00   10.00
```

Figure 2.4. Earth model (file "end.mod") presented in Table 2.2 in specific format for CPS package to be used to generate the synthetic seismogram.

The distance file contains multiple lines, and for each line a seismogram is generated. Each line can then be considered as the information of a sensor that the user intends to use to generate synthetic time series (Figure 2.5).

```
0.060000 0.0025  4096  0    0
```

Figure 2.5. Distance file (file "dfile") showing the specification of a synthetic seismogram to be generated at a station with 0.06 km (60 m) offset from source, a time step of 0.0025 seconds, and 4096 points.

Each line of the distance file contains the offset of that sensor to the source, time step, number of points to be generated, and start time for the seismogram synthesis, in terms of two parameters of the reduction velocity and initial time shift.

Through the command line, HPREP96 accepts the type of the green function to be produced, which the option "-ALL" in line #4 in Figure 2.3 requests that all types of green functions to be generated.

The depth of source (*$HS*) and receivers (*$HR*) are introduced as arguments in the HPREP96 command line. In line #5, the wavenumber integration is performed based on the details provided in Sections 2.1.4 using the HSPEC96 program. The final step is to select output type (displacement, velocity, or acceleration) and also to convolve the green function with a source wavelet using the program HPULSE96 in line #6. Since geophones are used, in line #5, the option "-V" is used to generate velocity synthetics, which later were convolved with the source wavelet. Therefore, the logical selection for the source wavelet in the HPULSE96 program is a Dirac delta function. However, to reduce negative truncation effects (the Gibbs phenomena) that produces side lobes, an alternative approach is followed (private communications with Robert Herrmann, and presented at http://www.eas.slu.edu/eqc/eqc_cps/TUTORIAL/RICKER/index.html): a parabolic source wavelet with a base width of Δt, is selected and then seismograms are differentiated (lines #7 through #12) with respect to time. Note that files for the green function synthesis are in the format "file96," and then are converted to the binary (B) SAC file format by piping them to the F96TOSAC program. Among different types of green functions, the one with extension code ZVF, which is the vertical velocity (ZVF) resulting from a vertical point force (ZVF), is used.

The reason for not using HPULSE96 in convolving the source wavelet with green functions is the way HPULSE96 is programmed, and also the high frequency of the observed source wavelet. For a parabolic or triangular source shape, the HPULSE96 program accepts the frequency of the pulse as a multiple of time step (Δt) introduced in the distance file. Since the observed frequency of the sledgehammer pulse is high, a very small time step (Δt) should be used in the synthesis. Otherwise, the synthesis computational time would be prohibitively long (about 6-7 days) for 72 geophones. The program HSPEC96 performs the major

calculation of wavenumber integration and also the implementation of complex wavenumber as described in Section 2.3.3.

HSPEC96 has the option to use a causal or a non-causal attenuation operator (the default is a causal operator, and adding "–N" in the command line argument switches to non-causal). The causality definition means that no wave arrives prior to the theoretical arrival time ($t = x/c$). In the source code of the HSPEC96 program the implementation for causality is the use of complex velocity in the form of Equation (2.61), and for the non-causal Futterman (1962) Q operator, the real part of the argument in Equation (2.61) is set to zero and only the imaginary part is used.

For the model introduced in Table 2.2, both the causal and non-causal Futterman (1962) Q operators are used based on the options introduced in the HSPEC96 documentation tutorial, and results obtained for a sensor at a distance of 60 m from the source is shown in Figure 2.6. The reference frequency used to generate synthetic seismograms in Figure 2.6 is 1.0 Hz.
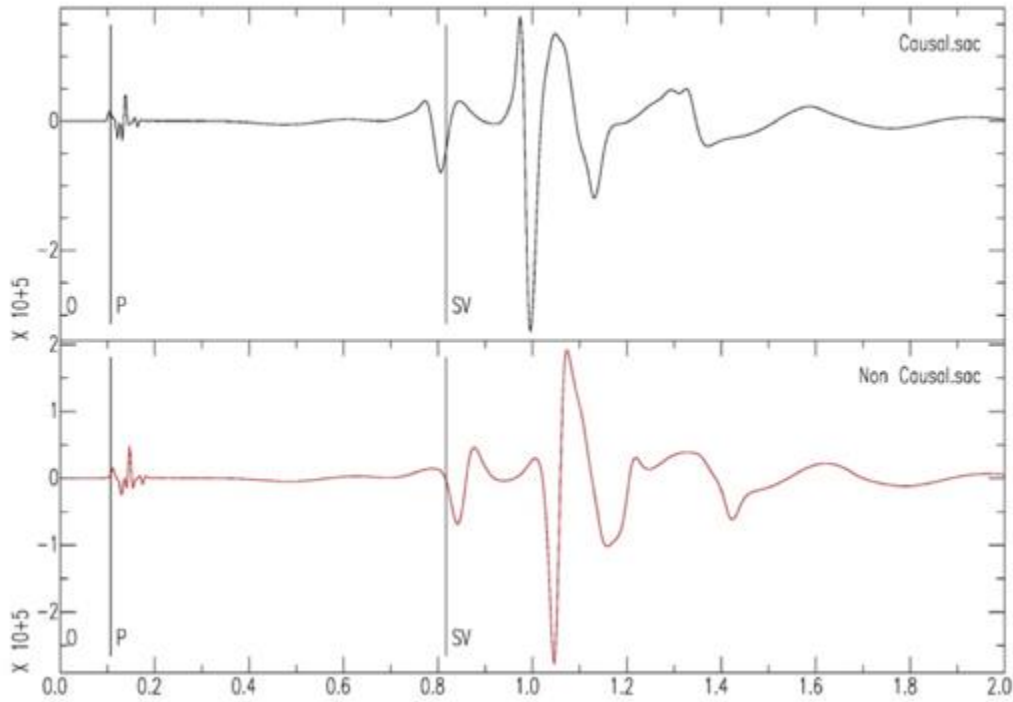

Figure 2.6. A synthetic full waveform seismogram with Futterman (1962) causal (top) and non-causal (bottom) operators using CPS package for the model, introduced in Table 2.2 for a sensor with 60 m offset.

It is observed that using the causal attenuation operator versus a non-causal one affects the arrival time of the wave. Other simulations have been performed considering other reference frequencies, including 10 Hz and 100 Hz, and are plotted against each other in Figure 2.7.
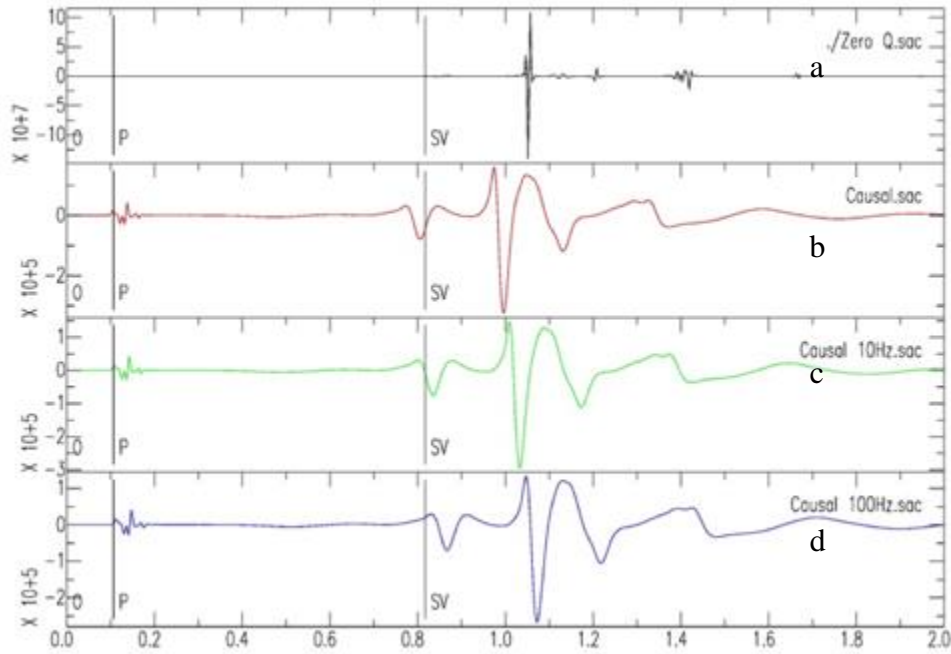
Figure 2.7. Comparison between different reference frequencies: (a) no attenuation, (b) 1 Hz, (c) 10 Hz, (d) 100 Hz.

2.3.4 Effect of Different Q Values on Seismogram

Since a constant quality factor is used for all layers, and since in some cases (Malagnini 1996) simultaneous inversion for the quality factor and phase velocities, does not yield reasonable results, it is useful to study the effect of different quality factor values on synthetic seismograms. A synthetic seismogram in an arbitrary geophone (#40) is generated based on an assumed 20 layer velocity model. The model comes from case 12 (Section 6.4) and quality factor values of 15, 20, 25, and 30 are used in generating the synthetic seismograms. The aforementioned values cover a widely acceptable range for quality factors, and will show that the selected quality factor in this range of 15 to 30 will not drastically change the amplitude and frequency content of the seismograms. Figure 2.8 shows a comparison between the time series for geophone #40 generated with four different Q factors. It is observed that the overall shape of the pulse is not changed much considering different Q factors, and only the arrival time of the pulse is mostly affected. This mild change in arrival times is due to the attenuation dispersion, since the heterogeneity of the model has not changed among different simulations.
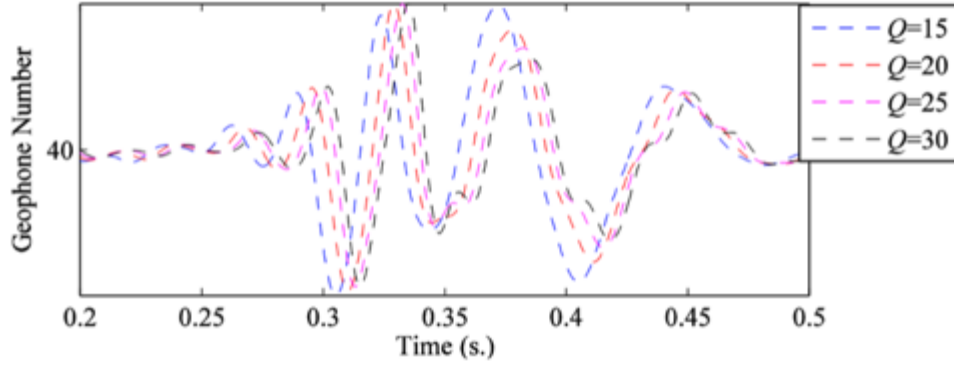
Figure 2.8. Four synthetic seismograms generated with four values of quality factor for geophone #40.

For comparison reasons, a quality factor of 25 is selected as a reference. Synthetic seismograms with quality factors of 15, 20, and 30 are compared with the synthetic seismogram generated with the quality factor 25. A cross-correlation coefficient is used to perform the comparison. First 3000 points corresponding to a time window of [0 0.75] seconds is used for correlation and comparison. The value of the zero lag cross-correlation is also presented, which is the 3000th element of the cross-correlation vector.

Figure 2.9 illustrates such a comparison. The correlation coefficients $CC(Q)$ are plotted for different Q values and time lags. The maximum correlation coefficient (CC_{max}) is also shown. It can be observed that the maximum coefficients are very close to unity, indicating that the two time series that are being compared are almost identical.
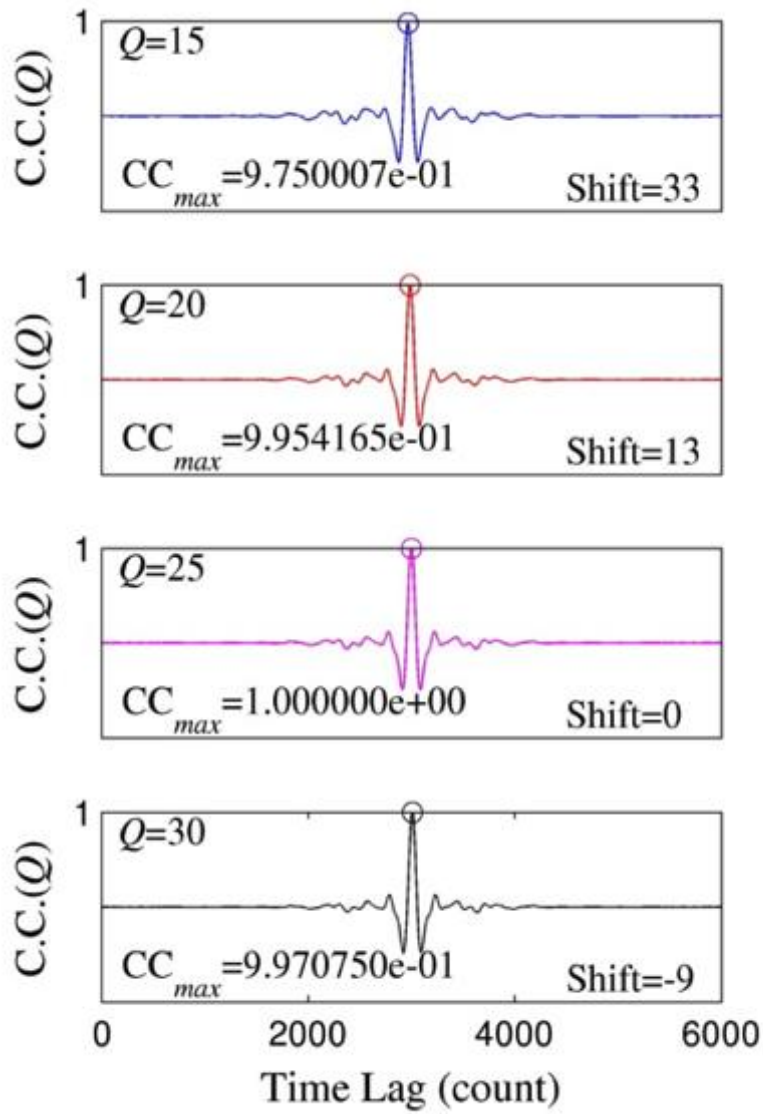
Figure 2.9. Correlation coefficient between synthetic seismogram with different Q values with the synthetics from Q=25. It is observed that cross-correlation coefficients are close to 1.0 after time shifts.

It is observed that in the case of geophone #40 and the current velocity model, the *Q* value does not affect the quality of the match between the synthetic seismograms drastically, and they are interchangeable in the range of study trial *Q* values.

2.3.5 Independent Estimation of Quality Factor

As will be mentioned in the following sections, it is possible to simultaneously invert for the shear-wave velocity profile and the quality factor. However, it is also possible to study the logarithmic drop in the Fourier amplitude of the recorded time series in space and to estimate the quality factor of the medium. Conceptually, this method is analogous to Section 2.3.2 where the logarithmic drop of amplitude is used to define the quality factor. It is noteworthy that the estimation of P-wave, S-wave or Rayleigh wave quality factors are essentially the same, and the difference is only in selecting the portion of the seismogram that carries that specific phase and in selecting a relevant geometric spreading for that specific phase.

2.3.6 Summary

The goal in seismology is to predict the ground motion at surface having the earth mechanical properties as known parameters. This chapter introduced the equation of motion for seismic waves in a homogeneous medium and then presented a systematic matrix approach to deal with the heterogeneous medium. The relationship between unknown surface displacements was related to the properties of each layer; displacement and stress at bottom of each layer were expressed as a function of those values at top of that layer and also properties of the layer. The requirement of continuity of displacement and stress at boundaries between layers made it possible to start from free surface of medium and kind of 'walk through' the layers and assemble the mechanical properties of those layers in a general relationship that connects the unknown surface displacement to deep half-space where displacements should be zero.

In this process, synthesis of seismogram becomes possible by consideration of an energy source at the interface between two layers. The equivalent displacement and stress due to the existence of the energy source should be considered in the aforementioned 'walk through' and since point force simulates the effect of source used in this study, the ensuing displacement and stress from a point source was introduced.

In the next section, attenuation was introduced into the wave equation using a complex wavenumber and the two effects of the attenuation were considered; i.e. dispersion and absorption. It was shown that dispersion is a necessity for a realistic seismogram without which there will be non-zero amplitude prior to the theoretical arrival time of the wave and supports the causality of the attenuation relationship. For absorption, it was shown that it affects the amplitude of the waves and at the end, a final formulation is provided to update for a complex velocity by having a known quality factor.

In the final section, numerical examples are provided showing that how selection of a suitable reference frequency is important and affects the arrival time of different phases. As Kanamori and Anderson (1979) stated, the selection of reference frequency should be based the knowledge of the velocity of material in that frequency range and it is easy to get confused by choosing a non-relevant reference frequency and velocity pair.

3. Field Test and Equipment

Two different field experiments were performed in this study: (1) a multi-channel analysis of surface waves (MASW) and (2) a downhole seismic survey. The concepts and the necessary background regarding the MASW method were introduced in previous chapters. In this chapter, the equipment used and some details necessary for a successful MASW experiment are presented. In regards to the downhole seismic survey, information on equipment, acquisition, and analysis techniques is provided by Stovall (2010) and will not be repeated here.

3.1 MASW Equipment

A successful acquisition using the MASW technique depends on correct connections among the different instruments:

- Vertical geophones to convert surface perturbations into electric analog signals (Figure 3.1).

Figure 3.1. Vertical geophone with corner frequency of 4.5 hz.

- Geophone cables for every 24 geophones to transmit the electric signals to the digitizing unit (Figure 3.2).
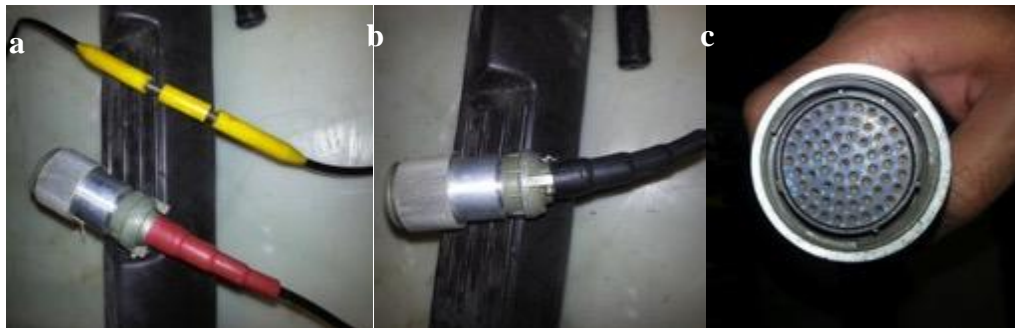

Figure 3.2. Geophone cable: (a) red end-connection and yellow slot for geophone hookup, (b) black end-connection, and (c) details of end-connection.

- Digitizing units that transform the electric analog signal into digital data recordable as a computer file. We use a Geometrics Geode® for this purpose (Figure 3.3).

Figure 3.3. Geometrics Geode® 24 channel digitizer.

- Data cables to transfer the digitized data into a PC (Figure 3.4).

Figure 3.4. Data transfer cable from Geode to Geode, or from Geode to software console on laptop.

- A laptop connected to the data cable to record incoming digitized signals into data files.
- A software console handling communication with the digitizers, recording the digitized signals into a file, and setting parameters related to the test. Such software also is the only interface interacting with the user.
- A source of energy like a sledgehammer.
- A trigger attached to the hammer, and an extension cable to attach the trigger to the digitizer (Figure 3.5).

Figure 3.5. Trigger that attaches to the sledgehammer and signals the hit time.

When the whole test setup is complete and everything is tested, then by striking a metal plate with a sledgehammer at a specific location, Rayleigh waves are generated. The trigger signals the digitizer to start recording at the onset of hit time, and the digitizer sends the data from the geophones to the software console on the laptop.

3.2 Sequential Use of Multiple Geodes

Geodes used for this study have 24 channels. If there are more than 24 geophones, a second Geode is required. In such a case, the first 24 geophones are connected to the Geode #1 using geophone cable #1, and data are sent to the second Geode using data cable #1. The second Geode captures data from geophones 25 to 48 and sends them along with the data coming from Geode #1, to Geode #3, and this process is repeated until digitized signals from all sensors are sent to the software console on the laptop.

When more than one Geode is being used, the sequence of geophones is very important. A geophone cable provided by the manufacturer has two ends, and the number assigned to each geophone depends on which head is connected to the Geode. (1) If the red head is connected, then all the numbering of geophones printed on the cable is correct. Otherwise, (2) if the black head is connected, then the numbering of the geophones is reversed. Therefore, there can be confusion in setting up the whole test, when geophone #25 on the ground is showing as geophone #48 on the console, geophone #26 is showing as geophone #47, etc. Therefore, it is useful to have someone walk by the geophone arrays while another person is checking the received signal on the console (using the noise monitor), to make sure that the number of the geophone on the console is the same as the physical location of the geophone that the person is walking by.

3.3 Trigger Effect and Stacking

Considering the presence of noise in the recorded data, it is common practice to repeat each hit several times and then stack the recorded data, so that the random nature of the noise will result in cancellation of the noise and the strengthening of the signal.

It is expected that when a trigger is used, all data recorded at a different hit will have the same signal, which can just be added point by point. However, after inspection of five different

recorded hits, it was realized that the trigger does not always trigger the same way at different hits. It seems that the recorded data from the five different hits were slightly shifted in time prior to the stacking process. This observation is related to 5 hits at the same place, close to geophone #1. Similar triggering time delays were observed at other locations of hits (geophone #3). Figure 3.6 shows perturbations recorded by four geophones from five hits (location of hits is at geophone #1 in Figure 3.6a and at geophone #3 in Figure 3.6b).
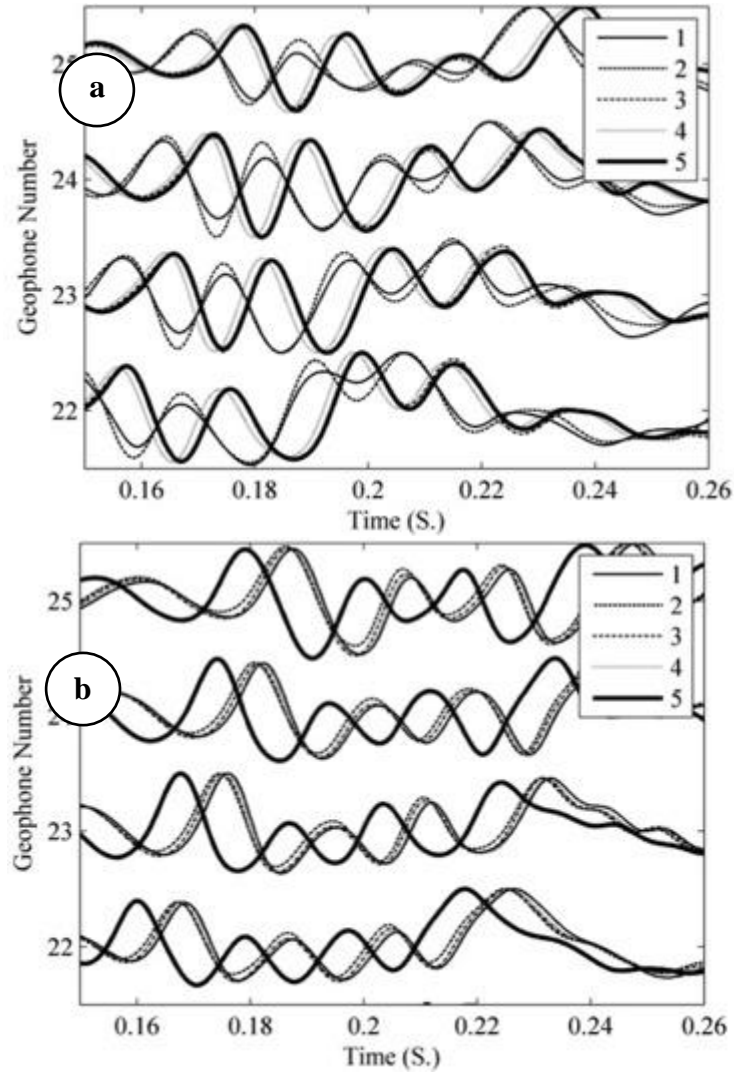
Figure 3.6. Time series recorded on four geophones from five different hits. It seems that the triggers have not been working uniformly among different hits; therefore, time series should be lined up prior to the stacking process. (a) the location of hits at geophone #1, (b) the location of hits at geophone #3.

The idea of correlation was used as a tool to synchronize the recorded time series at each geophone before the stacking process. As an example, the traces from the second hit shown in Figure 3.6 were used as the reference hit to estimate the required time shifts, so the best cross-correlation coefficient is obtained between other hits and the second hit. This process is repeated for all geophones, in the case where the hit location is at the first geophone (used in this study) and results are shown as a function of time step (Δt) in Figure 3.7b. The time lags resulting from a similar cross-correlation analysis for the hit location at geophone #3 is also provided in Figure 3.7a, showing that such problems always exist, and one must be cautious not to stack the traces prior to synchronization.
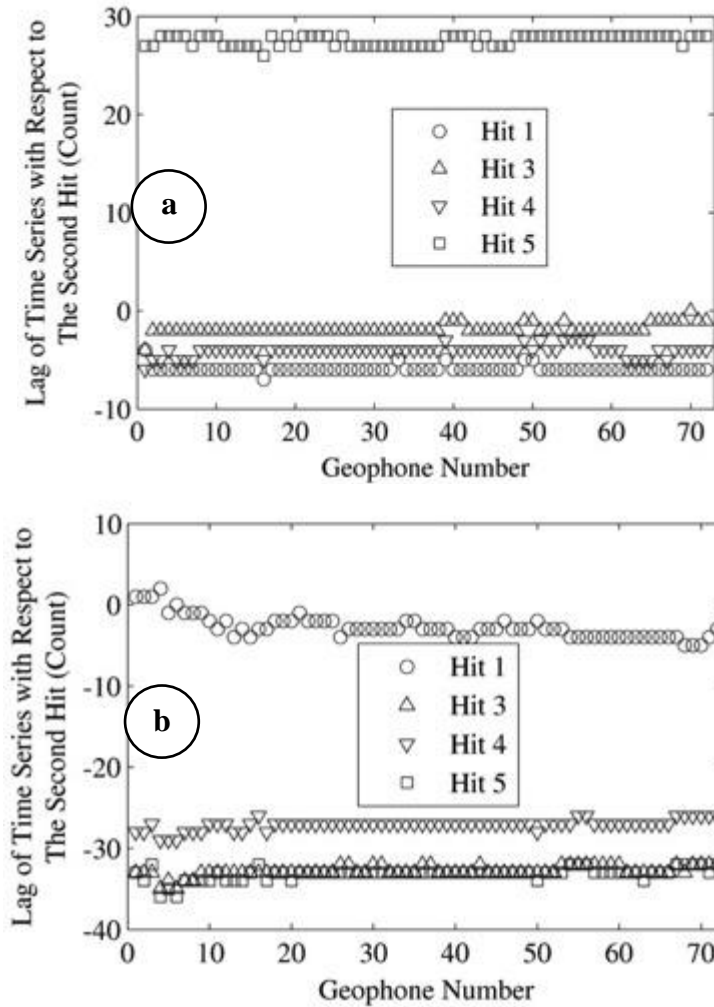

Figure 3.7. Time lags of 72 geophones (x-axis) with respect to the second hit. It is observed that the hit #5 has the maximum time lag of about 28 counts (equal to 28Δt). (a) the location of hit is at geophone #1, (b) the location of hit is at geophone #3.

3.4   Amplitude Clipping

It is observed that geophones that are very close to the hit location are clipped (*Figure 3.8*) where maximum amplitudes have exceeded a specific limitation and are replaced with a maximum threshold. Two points are necessary to be taken into account while designing a MASW experiment: (1) very close geophones are not to be used in the analysis of surface waves due to near-surface effects; and (2) sometimes even those geophones beyond the domination of the near-surface effect may also experience clipping. In the second case, the solution is to use a low gain in the acquisition, or to increase the source-array offset, while considering the far-field effect.
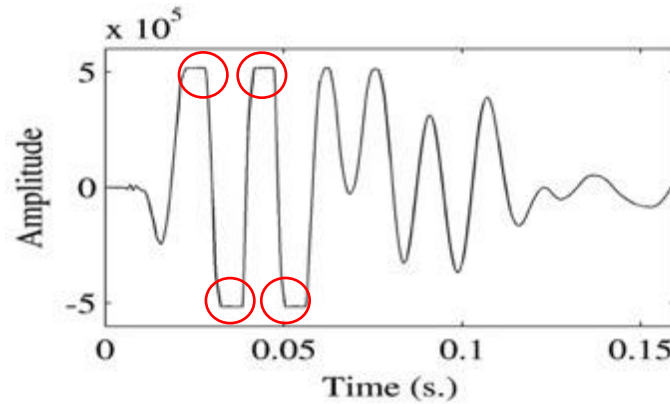

Figure 3.8. Time series are clipped at the location of the red circles (geophone #4, stacked data).

The software console is able to identify when the clipping happens, and marks those traces with red color instead of black. In the case of the existence of clipping, the clipped traces should not be considered in the analysis.

3.5   Comparison of MASW with Another Surface Seismic Method

Even though the method used to estimate the experimental dispersion curve from the field data has not been discussed yet, it seems necessary to determine whether the dispersion from the MASW experiment agrees well with other surface-based seismic methods such as the Spectral Analysis of Surface Waves (SASW) experiment with multiple channels.

The SASW experiment was performed using an electrical shaker oscillating at a preset frequency range of 3.75 to 100 hz, recording each frequency for a window of 16 seconds. The shaker oscillates with a fixed frequency for 16 seconds, and then the frequency is increased and the process is repeated to reach a maximum frequency of 100 Hz. Data are windowed for the middle 10 seconds for each frequency.   Rayleigh waves are recorded using 15 accelerometers deployed with a non-uniform spacing. Details of the SASW test can be found in Stovall (2010). The array is positioned in a way that its midpoint falls on the location of the borehole (for downhole test) and the same for the MASW array. The SASW field test and data analysis were performed by the authors.

Even though the source type, array lengths, and the spacing between sensors for MASW and SASW tests are completely different, the authors find it logical to compare the dispersion curves between the two methods. It has been observed in the literature that researchers use different methods (surface and borehole), different types of sensors (accelerometers and geophones), and different types of sources (active and passive) to estimate the ensuing shear-wave velocity for a specific location, and compare the results against each other (O'Connell and Turner 2011; Odum *et al.* 2013; Piatti *et al.* 2013). Therefore, two different testing procedures (MASW and SASW) are employed and will be used to determine the shear-wave velocity profile as a function of depth. Since it is possible to compare shear velocities from different methods, it is logical to be able to compare the phase velocities as a function of frequency for the two methods as well.

More importantly, inversion adds uncertainties into the inversion problem regarding the assumptions made through the inversion and also the inevitable non-uniqueness of the inversion solutions. It is inferred that it is logical to compare the data prior to being contaminated with these uncertainties. Therefore, the dispersion curves from the MASW and the SASW tests are compared. Figure 3.9 illustrates the dispersion contour obtained by performing the SASW test, while the circles plotted on top of the dispersion contour are from the MASW method. It can be observed that there is a good match between the MASW and SASW dispersion curves.
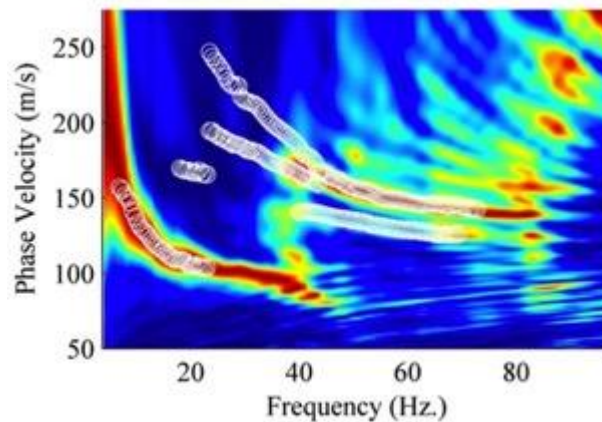

Figure 3.9. The MASW dispersion curves (white circles) are plotted on top of the SASW dispersion contour. A good agreement exists between the two methods.

4. Experimental Phase Velocity Dispersion and Inversion: Procedures

4.1   Signal Processing Techniques for Observed Dispersion

Applying the inversion methodology introduced in the previous chapter clearly requires the experimental (observed) dispersion data to be inverted to determine the shear-wave velocity structure. Therefore, the very first step to start the analysis of the field data should be initiation of a signal processing technique to reliably measure the phase velocities of the Rayleigh wave. In this study, vertical geophones were used; therefore, the effect of Love waves is not considered.

Recorded time series from the geophone array are used to construct a contour representing the variation of the phase velocity versus the frequency, which is called the phase velocity dispersion curve. First, time series are decomposed into several narrow-frequencies using a narrow band-pass filter, and then for each group of filtered time series, an appropriate signal-processing technique is used to measure their phase velocity spectrum for the center frequency of that band. Details of the required procedures to construct the experimental dispersion curve are discussed in the following sections.

4.2   Frequency-Swept Decomposition of Time Series

This section provides detailed information on how to alter recorded time series into time series that contain only a desired frequency band by using a narrow band-pass filter. A stretch function is used to separate each time series into individual frequencies. Each set of individual-frequency time series are analogous to those recorded by using a harmonic source (Coruh, 1985; Park *et al*., 2000).

Typically, two different source types are used: (1) a harmonic shaker and (2) an impulsive force like a sledgehammer (Park *et al*., 2000). A harmonic shaker generates a sinusoidal motion with a specific frequency for a short period of time (i.e., 10-20 seconds; see Stovall 2010), and then the frequency is incremented and the process is repeated. This type of source provides a frequency-swept record where the response of the earth to a harmonic wave with a single frequency is determined in the field. Data collected using a harmonic source is ideal because it is already in a frequency-decomposed format. An impulsive force contains a broader range of frequencies and therefore should be decomposed into narrow-band frequency time series to be comparable to those from a harmonic vibrator. It is possible to use a filter to make a time series carry only frequencies in a desired frequency range, mimicking records from a harmonic source. The impulsive force source type is similar to the seismic reflection experiments where a shotgun/airgun is used. An impulsive force source is widely used in the MASW method. In this study, a sledgehammer was used as the impulse force. A stretch function can be defined as (Coruh, 1985):

$$\mathbf{R}_s(t) = \mathbf{R}(t) * \mathbf{S}(t) \tag{4.1}$$

where $*$ denotes the convolution operator and the subscript s indicates the waveform vector after being convolved with the stretch function. The stretch function $\mathbf{S}(t)$ is a sinusoidal function where the frequency changes with time. Waters (1978) and Park $et\ al.$ (2000) suggested using a stretch function similar to the Vibroseis surveys:

$$\mathbf{S}(t) = \sin\left(2\pi f_1 t + \frac{\pi(f_2 - f_1)}{T} t^2 \right) \tag{4.2}$$

where f_1 and f_2 are the lowest and highest frequencies of the desired frequency band and T is the length of the stretch function in seconds. In this study, the variables f_1 and f_2 have a difference of 1 Hz while their average is equal to the target frequency. The stretch function works like a band-pass filter, and it should be convolved with the observed time series.

The next step is to estimate the phase velocity from the filtered time series. In this study, a frequency-wavenumber technique is used for this purpose, which is discussed in the next section.

4.2.1   Concept of the Frequency-Wavenumber Method

This section provides insight into the nature of the frequency-wavenumber method. Beamforming is a well-known signal-processing technique that is used in sensor arrays for directional transmission or reception (Van Veen and Buckley, 1998). The beamforming technique is widely used in radio communications where a special type of antenna is used, instead of a linear receiver array, to reconstruct the message sent from the source (Van Veen and Buckley, 1998). In the field of geophysics and seismology, the reception of the seismic wave is of interest and; therefore, the beamforming technique consists of reconstructing the signal generated at a source by combining the received signals at the array channels with different delays, so that the overall summation of delayed signals can be a more accurate representation of the original signal. The signal from the channel closest to the source needs minimum delay compensation in time, while the signal from the farthest channel requires maximum delay compensation.

The beamforming technique and the frequency-wavenumber Fourier method are similar, but the latter has advantages over the former method from a computational efficiency viewpoint (Hinichi, 1980). However, both methods share almost the same concept and are replaceable in regards to their application in this study. Therefore, in this study, the beamforming concept was used to determine the phase velocity spectrum at a specific frequency.

The goal of this section is to determine the phase velocity by which a wave with a specific frequency is traveling. This goal is accomplished by presenting a spectrum curve for a single frequency wave that has a peak at the target phase velocity. Considering Equation (4.3, we are looking for a frequency-wavenumber pair that generates a peak in the spectrum contour

$$V_R = f . \lambda = \frac{2\pi f}{k} \tag{4.3}$$

where V_R is the phase velocity, f is the frequency, λ is the wavelength, and k is the wavenumber (Richart *et al*., 1970). Since the frequency is assumed to be constant, then we are looking for the wavenumber (k_0) that generates the peak considering a wave bearing the constant frequency (f_0). The amplitude of a wave with a constant angular frequency can be defined at the source location as (Hinichi, 1980; Longhurst, 1967):

$$\mathbf{u}(t) = \mathrm{Re}\left\{|A|\left[\cos(\omega_0 t) + i\sin(\omega_0 t)\right]\right\} = \mathrm{Re}\left\{|A|\exp[i\omega_0 t]\right\} \tag{4.4}$$

where $\mathbf{u}(t)$ is the time domain source signal and ω_0 is the constant angular frequency of the wave, and the complex exponential is a result of Euler's equations. Assume that such a wave is traveling parallel to a sensor array consisting of *M* channels. Assuming a homogeneous medium with no attenuation, the time domain signal recorded at the jth channel can be presented as:

$$
\begin{aligned}
\mathbf{R}(t, x_j) &= \mathrm{Re}\left\{|A_j|\left[\cos(w_0\, t + j) + i\sin(w_0\, t + j)\right]\right\} \\
&= \mathrm{Re}\left\{|A_j|\exp[i(w_0\, t + j)]\right\} = \mathrm{Re}\left\{|A_j|\exp\left[i\left(w_0 t - \frac{w_0}{V_R} x_j\right)\right]\right\} \\
&= \mathrm{Re}\left\{|A_j|\exp\left[i(w_0 t - k_0 x_j)\right]\right\}
\end{aligned}
\tag{4.5}
$$

where $\mathbf{R}(t, x_j)$ is the time domain signal at the location of the jth channel, x_j is the distance of the channel from the source, φ is the time delay or phase shift that occurs for a wave with angular frequency ω_0 and phase velocity V_R to travel from the source to the receiving channel, and k_0 is the characteristic wavenumber associated with the signal.

Now assume that we would like to estimate the summation of the peaks of a known signal over all stations using a beam pointed parallel to the array. For this goal, since the wave characteristics are known, then we know the two fundamental parameters of wavenumber and frequency of the traveling wave (k_0 and ω_0). Knowing these two parameters, we can then calculate and compensate the phase shift and add the amplitude of all the signals together, and this gives a different result from simply averaging the signals (Hinichi, 1980):

$$
\begin{aligned}
\mathbf{B}(t) &= \frac{1}{M}\sum_{j=1}^{M}\mathrm{Re}\left\{|A_j|\exp\left[i\left(w_0 t - \frac{w_0}{V_R} x_j\right)\right]\right\} \\
&= \frac{1}{M}\sum_{j=1}^{M}\mathrm{Re}\left\{\mathbf{s}(t, x_j)\exp[ik_0 x_j]\right\}
\end{aligned}
\tag{4.6}
$$

The methodology, by which we can reconstruct a signal from observations in different sensors, is demonstrated in Figure 4.1. A source signal $\mathbf{u}(t)$ with a constant frequency is generated at $x = 0$ and is recorded at six channels, $\mathbf{R}(t, x_j)$, while $j = 1$ to 6, located over a range of distances from 4 to 8 meters from the source location. We have tried to reconstruct the signals by averaging the signals $\frac{1}{M}\sum_{j=1}^{M}\mathbf{R}(t, x_j)$, and it is obvious that they have destructive interference because the simple average has much lower amplitude than the original signal generated at the source. However, we can use Equation (4.6) to compensate for the time delay among different signals and source time series by applying an appropriate phase shift in the frequency domain and, therefore, we can reconstruct the source signal amplitude accurately.

The last term of Equation (4.6) is equivalent to computing a spatial Fourier transform of the M signals from the array. In the frequency-wavenumber analysis, the time series from a finite number of channels are filtered for a specific frequency, and then the spatial Fourier transform is computed, and the square of the magnitude of such a transform will be equal to $(M|A|)^2$ if the selected wavenumber is equal to that of the propagating wave for that specific frequency,

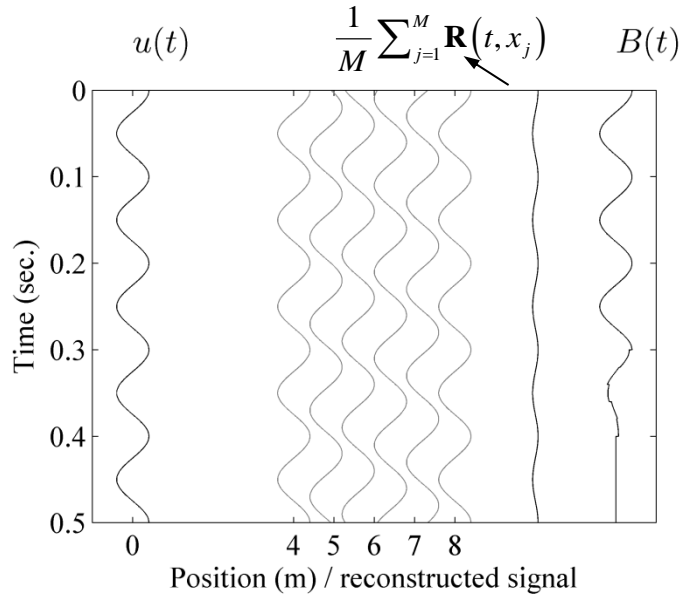$k = k_0 = \frac{\omega_0}{V_R}$ (Hinichi, 1980).

Figure 4.1. Reconstruction of B(t) of source signal u(t) by superposition of delayed received signals.

4.2.2 Frequency-Wavenumber Technique

After each time series is separated into individual frequencies, the required next step to construct the experimental dispersion contour is to determine the phase-velocity spectrum for each group of individual frequency time series.

The phase velocity can be defined as the slope of the line connecting the relevant wave peaks together in the offset-time (*t-x*) plot. A practical way to do the calculation is to consider different slopes and calculate a normalized summation of wave amplitudes along each slope to obtain the phase velocity spectrum for a single frequency. The slope associated with the maximum cumulative amplitude is used to obtain the phase velocity for that specific frequency. An example of field-recorded data is provided in Figure 4.2, where the time series for four geophones are plotted along with their real (blue) and imaginary (red) components of their Fourier transform. The time series are filtered using a transfer function with a center frequency of 10 Hz.

Two major problems might arise in working with slopes in the time domain: (1) the method may provide different cumulative normalized amplitudes for a specific slope as shown in Figure 4.3 for two different time-intercepts; and (2) the method may be developed poorly on the assumption that the velocity of the wave from one geophone to another is constant along a specific slope, which might not be the case. To overcome these limitations and inaccurate assumptions, the frequency-wavenumber technique (Hebeler, 2001; Stovall, 2010; Zywicki, 1999) is used.
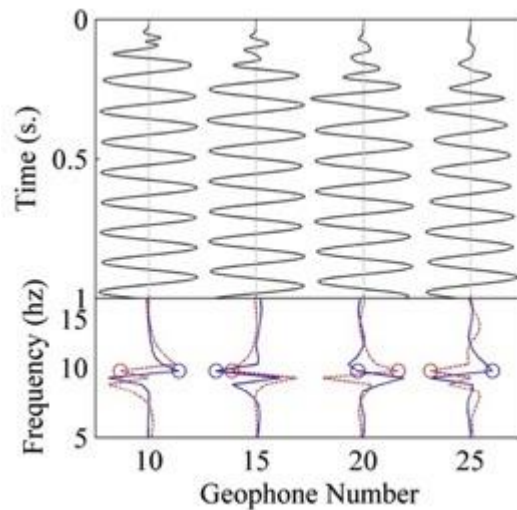

Figure 4.2. (Top) Times series from field data in four geophones. (Bottom) The Fourier transform is used to calculate the real (blue) and the imaginary (red) parts of traces. Time series were previously convolved with the stretch function of 10 Hz and, spectral values at 10 Hz frequency are determined, indicated with circles.
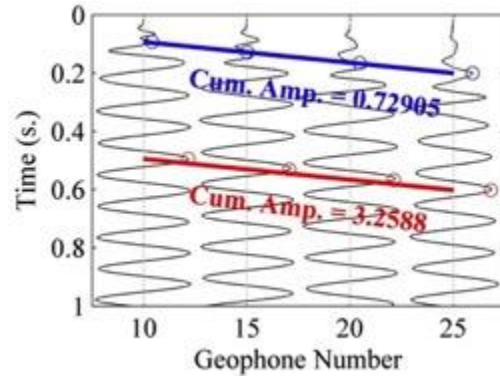
Figure 4.3. Cumulative amplitude along two lines with different time intercepts. Sloped lines are associated with a phase velocity of 116 m/s. Time series are carrying a center frequency of 10 Hz only.

To solve the two problems discussed above, one can use the Fourier amplitude rather than time series. As shown in Figure 4.3, each time series has various peak amplitudes, but the Fourier amplitude is always the same for a specific frequency. Instead of using time series peaks to determine the cumulative amplitude for a give slope, the frequency domain counterpart is used. First, a Fourier transform is applied to obtain $F(\omega)$ from the time series f (*t*) for each geophone. The Fourier spectrum can be written as $F(\omega) = a+jb$, where the colors are analogous to those colors used in plotting real and imaginary parts of the Fourier spectrum in Figure 4.2 and Figure 4.4.

The spectrum $F(\omega)$ is calculated for a broad range of frequencies, and we will be looking for the complex number associated with the angular frequency (ω_f) that we already filtered the data for. The $F(\omega)$ spectrum is displayed in Figure 4.4 for four geophones, and the values of the real and imaginary spectrums corresponding to ω_f are plotted with blue and red circles respectively.
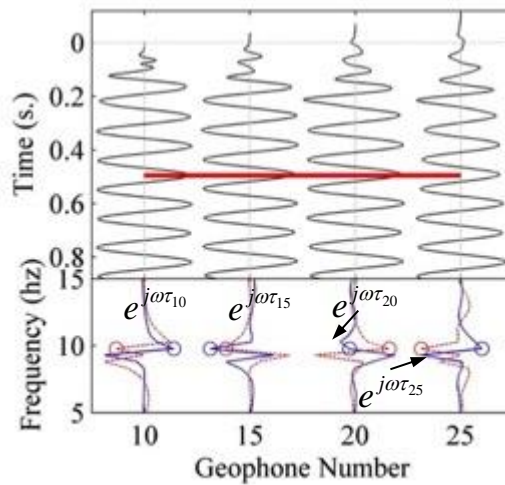

Figure 4.4. Alternative approach for calculating amplitudes along red sloped line in Figure 4.3.

43

The cumulative amplitude of the time series along a specific slope (like the red line in Figure 4.3), resembles moving each time series backward in time (a time shift of τ_i for the ith geophone) so that amplitudes along the slope will line up (Figure 4.4). Multiplying $F(\omega_f)$ with $\exp(j\,\omega_f\tau_i)$ in the frequency domain is similar to a time shift of τ_i in the time domain. The time shift τ can be calculated as:

$$\tau_i = \frac{x_i}{c_k} \tag{4.7}$$

where x_i is the distance between the first geophone and the ith geophone, and c_k is the phase velocity associated with the trial slope ($m = 1/\ c_k$) along which the cumulative amplitude is being calculated. Figure 4.4 shows the exponential values by which the Fourier spectrum should be multiplied.

This frequency-wavenumber (f-k) technique was introduced by Capon (1969), and can be used to generate the experimental phase velocity dispersion contour. A slightly modified procedure by Park et al. (1998a) was used because of its efficiency. This method is different compared to the conventional f-k transformation and seems to work better with a limited number of geophones (Park et al., 1998a; Tran and Hiltunen, 2008). The pair of frequencies and their associated wavenumber is addressed with a peak in the spectrum (Tran and Hiltunen, 2008):

$$\mathbf{P}(f,V_R) = \sum_{i=g_1}^{g_2} \exp\left[j\frac{2\pi f}{V_R} x_i \right].\mathbf{N}(f,x_i) \tag{4.8}$$

where $\mathbf{P}(f,V_R)$ is the phase velocity dispersion spectrum, V_R is the trial phase velocity, f is the dominant frequency, x_i is the distance of the ith geophone from the source, g_1 and g_2 are the number of the first and last geophones for calculating dispersion, j is the imaginary number, and $\mathbf{N}(f,x_i)$ is the normalized Fourier transform of the time domain signal recorded at the ith geophone for the single frequency f, defined as:

$$\mathbf{N}(f,x_i) = \mathbf{OF}(f,x_i)/\left|\mathbf{OF}(f,x_i)\right| \tag{4.9}$$

where $\mathbf{OF}(f,x_i)$ is the discrete Fourier transform of $\mathbf{OF}(t,x_i)$ at the frequency f, and where $\mathbf{OF}(t,x_i)$ is the filtered seismogram at the ith geophone by convolving it with the stretch function given in Equation (4.2):

$$\mathbf{OF}(t,x_i) = \mathbf{O}(t,x_i)*\mathbf{S}(t) \tag{4.10}$$

An example of the dispersion calculation of the dispersion spectrum based on Equation (4.8) is presented for the time series from geophones 10, 15, 20, and 25, as illustrated in Figure 4.5.

It is observed that the cumulative amplitude is a maximum at a slope associated with a phase velocity of about 130 m/s. Recalling that we had filtered the raw time series for a center frequency of 10 Hz, the phase velocity at 10 Hz is $c(10\text{ Hz}) \approx 130$ m/s.
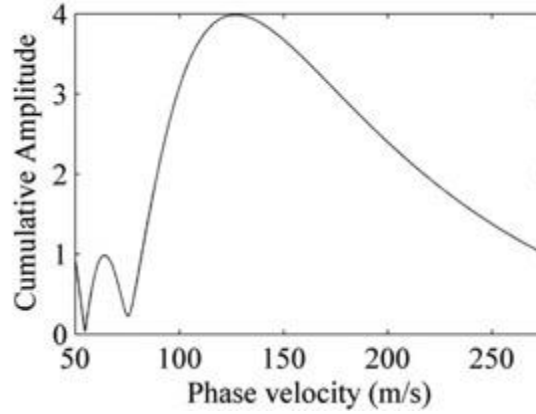

Figure 4.5. The dispersion spectrum at a center frequency of 10 hz, or $\mathbf{P}(10, V_R)$.

Repeating the aforementioned process using the frequency-wavenumber method for a wide frequency range can provide the spectrum (distribution of energy) for a range of phase velocities at each single frequency. The result of such an analysis procedure can be presented as a contour plot, which is referred to as a "dispersion contour" or "overtone image," and the dispersion curve is generated by picking velocities with the maximum amplitude at each frequency. In general, the flowchart for construction of the dispersion contour can be summarized as:

1. A range of frequencies is selected; the spectrum will be determined for each single frequency in the selected range.
2. A phase velocity range is selected for calculating the spectrum at each single frequency.
3. The times series are filtered using the stretch function with a center frequency selected from Step 1.
4. The frequency-wavenumber transform from Equation (4.8) is applied to the filtered time series, and the dispersion spectrum for the selected frequency is obtained.
5. Repeat Steps 1 through 4 for frequencies in the selected range of step 1.
   A software program for calculation of dispersion curves using the aforementioned steps are developed in MATLAB (Hosseini, 2014).

4.3   Inversion and Non-uniqueness

Inversion of surface waves can be established by the use of partial derivatives of the phase velocity with respect to the model parameters. Model parameters are unknowns and can be found in the inversion process. The phase velocity dispersion curve is mostly sensitive to the

shear-wave velocity of the layers (V_S) and their thickness (H) (Nazarian, 1984; Yuan and Nazarian, 1993; Xia *et al*., 1999a, 1999b). It is common to keep one of these two parameters (V_S or H) fixed (Nazarian, 1984; Yuan and Nazarian, 1993; Xia *et al*., 1999a, 1999b). A thickness of about 1.5 m (5 ft) was selected for each layer, corresponding to the reported depth intervals in the downhole seismic survey. Compressional wave velocity (V_P) is calculated from V_S considering a fixed Poisson's ratio for each layer. A Poisson's ratio of 0.45 (Foti and Strobbia, 2002) was selected for this study. Yuan and Nazarian (1993); Xia et al. (1999a, 1999b); and Rix and Lai (1998) provided techniques for stable inversion of surface waves. In general, for a nonlinear inversion problem $\mathbf{G}(\mathbf{m}) = \mathbf{d}$, the solution can be obtained by using Occam's localized inversion technique (Aster *et al*., 2003) by using the Jacobian matrix. Inversion is performed by minimizing the following objective function in a damped least-square inversion (Aster *et al*., 2003):

$$F = \left\| \mathbf{J}(\mathbf{m})(\mathbf{m} + \Delta\mathbf{m}) - (\mathbf{d} - \mathbf{G}(\mathbf{m}) + \mathbf{J}(\mathbf{m})\mathbf{m}) \right\|_2^2 + \lambda^2 \left\| \mathbf{L}(\mathbf{m} + \Delta\mathbf{m}) \right\|_2^2 \qquad (4.11)$$

where $\mathbf{m}$ is the unknown model parameters vector, $\Delta\mathbf{m}$ is the change in vector $\mathbf{m}$ with m elements, $\mathbf{d}$ is the observed data with n elements, $\mathbf{G}$ is a known n by m a matrix that relates model parameters with observations, $\mathbf{L}$ is the finite difference operator (Aster *et al*., 2003, Chapter 5) approximating the first or second derivatives of the model parameters when it is multiplied by them and controls the smoothness of the solution, $\| \ \|_2^2$ is the L_2 norm squared, λ is the damping factor, and finally $\mathbf{J}(\mathbf{m})$ is the Jacobian matrix, introduced as:

$$\mathbf{J}(\mathbf{m}) = \begin{bmatrix} \dfrac{\partial G_1(\mathbf{m})}{\partial m_1} & \cdots & \dfrac{\partial G_1(\mathbf{m})}{\partial m_m} \\ \vdots & \ddots & \vdots \\ \dfrac{\partial G_n(\mathbf{m})}{\partial m_1} & \cdots & \dfrac{\partial G_n(\mathbf{m})}{\partial m_1} \end{bmatrix}_{n \times m} \qquad (4.12)$$

The Jacobian matrix holds the partial derivatives of the forward equation with respect to the model parameters, and in the case of our study, it is holding the partial derivatives of phase velocity with respect to shear-wave velocities at each layer (and may be quality factors at each layers if they are considered unknown). Equations for partial derivatives of phase velocity with respect to model parameters are provided in Chapter 3, Section 9 of Ben-Menahem and Singh (1981). Selecting an appropriate damping factor λ is crucial for a successful inversion. Pujol (2007) gives a good insight into the solution of nonlinear inverse problems using the Lenevberg-Marquardt method. Inversion for surface waves is performed iteratively using Occam's algorithm to find the model parameters (Aster *et al*., 2003):

$$\mathbf{m}^{k+1} = \left[\mathbf{J}(\mathbf{m}^k)^{\mathrm{T}} \mathbf{J}(\mathbf{m}^k) + \lambda^2 \mathbf{L}^{\mathrm{T}} \mathbf{L} \right]^{-1} \mathbf{J}(\mathbf{m}^k)^{\mathrm{T}} \left[\mathbf{d} - \mathbf{G}(\mathbf{m}^k) + \mathbf{J}(\mathbf{m}^k)\mathbf{m}^k \right] \qquad (4.13)$$

where k is the iteration number, and the initial profile starts at $\mathbf{m}^0$. As will be seen in the results in the following chapter, the phase velocity dispersion curve has different branches of

phase velocities that are related to different modes. Using phase velocity data for higher modes increases the resolution of the inversion in depth according to the longer wavelength of higher modes (Beaty *et al.*, 2002; Stovall, 2010; Xia *et al.*, 2003), and is unavoidable according to the results in the final chapter. To benefit from the higher modes, assigning a specific mode number to each branch of the observed dispersion curve is essential (Herrmann, 1987; Luo *et al.*, 2007; 0Park *et al.*, 1999a; Stovall, 2010) and, therefore, by assigning different mode numbers to each dispersion curve branch, several scenarios exist which increases the problem associated with the non-uniqueness.

4.3.1 Inversion of Surface Waves with CPS

Herrmann (1987) provided a series of software programs to invert surface wave phase velocities. SURF96 is the computer program used in this study. Dr. Herrmann on his web site provides a tutorial and an example. Since this study deals with shallow velocity profiles in the case of the MASW test, a set of special settings is considered:

- A known thickness and quality factor structure is assumed,
- The dispersive effect of attenuation is considered along with the Rayleigh dispersion,
- Half-space velocity is allowed to change in the inversion process, and

The SURF96 source code is modified to keep the density fixed in the iteration process. In the subroutine MODLS() from file MODLS.F, the following lines must be added after line 162, before line 163 in the original source code, and recompiled for an updated SURF96 executable file using command "make all" (Figure 4.6):

```
r(i) = rho(i)
```

Figure 4.6. Modifications to be made to MODLS.F to stop SURF96 from changing density for shallow sites.

- No difference minimization (smoothing) is allowed in the inversion, and
- Damping values for each iteration are selected in such a manner that no increase in error percentage is allowed as the number of iterations grows.

In the last item mentioned above, the error at each iteration is calculated using the shell script provided in Figure 4.7:

```
#!/bin/sh
rm tmpmod* tmpsrfi* *.PLT *.out end.mod tmpmrgs* start.mod o17.* damping -fr
surf96 39              # Clean up
surf96 31 20 1         # Half-space velocity is allowed to change
surf96 35 2            # Inversion based on Q-Vs full interaction
surf96 36 0            # No difference minimization (smoothing)
NI=5; DF=20                                                              LINE 7
surf96 32 "$DF"        # Damping factor = 20                             LINE 8
for i in $(seq 1 "$NI") # Number of Iterations                          LINE 9
do                                                                      LINE 10
  time surf96 37 1 1 2 6                                                LINE 11
  xn=`expr $xn + 1 | awk '{printf "%02d\n",$1}'`                        LINE 12
  surf96 17 > o17.$xn                                                   LINE 13
  surf96 47 |grep "Damping value"  | awk '{print $2}' >> damping        LINE 14
done                                                                    LINE 15
surf96 1 2 28 end.mod  # Get the final inverted model
./geterror.sh          # Calculate percentage error
```

Figure 4.7. Bash script used in the inversion of surface waves using SURF96

where $NI is the number of iterations with the specific damping factor of $DF. At each iteration, partial derivatives are calculated and the model is updated (line #11), the theoretical dispersion curve of the current iteration is reported to file *O17.$XX* in line #13 where *$XX* is the sequential number of iteration, and in line #14 damping for the current iteration is also reported to file "damping." To increase the number of iterations and also change the damping factor, lines 7 through 15 must be duplicated and additional iteration numbers and new damping factors should be updated at the line corresponding to line #7 for the new block. At the end of the inversion, a script called geterror.sh is run, and the error for each iteration is calculated using the following equation:

$$Error = \sum_{i=1}^{NB} \sum_{j=1}^{NF(i)} \left[\frac{100 \times \dfrac{\left| c_{i,j}^{obs.} - c_{i,j}^{theo.} \right|}{c_{i,j}^{obs.}}}{NB \times NF(i)} \right] \tag{4.14}$$

where *NB* is the number of modes of the dispersion curve, *NF(i)* is the number of frequencies for i^{th} mode, $c_{i,j}^{obs.}$ is the experimental dispersion curve at frequency *j* and mode *i*, and $c_{i,j}^{theo.}$ is the theoretical dispersion curve after a specific number of iterations. Such calculations are simply implemented in a shell script (file "geterror.sh" as presented in Figure 4.8) using the following single-line script for every *O17.$XX* file and error is appended to the file "errorlist":

```
#!/bin/bash

tail -n`cat o17.$XX | wc -l | awk '{print ($1)-1}'` o17.$XX | awk 'BEGIN {c=0;xn=0;}
{d=1;if($5-$6<0)d=-1;c=c+d*100*($5-$6)/$5;xn=xn+1;}END{print c/xn}' >> errorlist
```

Figure 4.8. Shell script used to calculate the error percentage between the theoretical and experimental dispersion curves after the SURF96 inversion.

5. Simulation of Non-uniqueness in Surface Wave Inversion

To investigate the source of non-uniqueness in the inversion of phase-velocity dispersion curves, a synthetic example is presented where a dispersion curve from a known velocity profile is inverted, and it is shown that the two different velocity profiles exhibit very similar dispersion properties.

5.1 Simulation of Non-uniqueness

A three layer over half-space model is assumed to be representative of the shallow subsurface. Each layer is assumed to have a thickness of 4 m, and the half-space starts from a depth of 12 m. The synthetic model is intended to resemble a real case; therefore, a water level is assumed to be present at the interface between the first layer and the second layer (Foti and Strobbia, 2002). Water level affects the Poisson's ratio; for saturated soil a ratio of 0.45 is used; otherwise, 0.25. Figure 5.1 shows the profile used in this synthetic example.
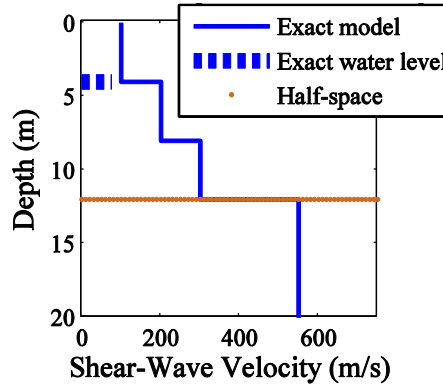
Figure 5.1. The exact model assumed in the synthetic test as the representative of the shear-wave velocity profile of the subsurface.

Using forward modeling, the phase-velocity dispersion curve is determined and a random five percent noise with a normal distribution is added to the dispersion data (Figure 5.2) to generate a realistic synthetic experimental dispersion curve (SEDC). This curve is treated as the dispersion curve obtained from the field data and is used in the inversion process. The inversion process is a linearized damped inversion technique (Aster *et al.*, 2003), which will be discussed later in the inversion section for the real world data.
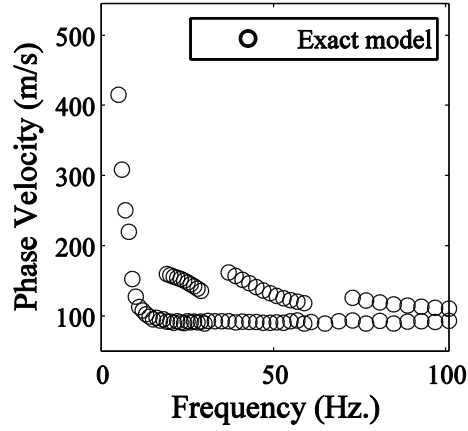
Figure 5.2. Synthetic experimental dispersion curve (SEDC) is constructed by generating a dispersion curve from the exact model presented in Figure 5.1 and adding 5 percent random noise to it.

Initial velocity profiles for the inversion were constructed by assuming six layers over half-space (each layer 2 m thick), and the half-space depth is 12 m. By combining two V_S profiles and eight different levels of water table, sixteen initial velocity profiles are generated and separately inverted. The focus of this discussion is on two inverted models (labeled 6 and 11) for which the dispersion curves are virtually indistinguishable for all the modes (up to three higher modes). Figure 5.3 and Figure 5.4 present the results of inversion for cases 6 and 11.
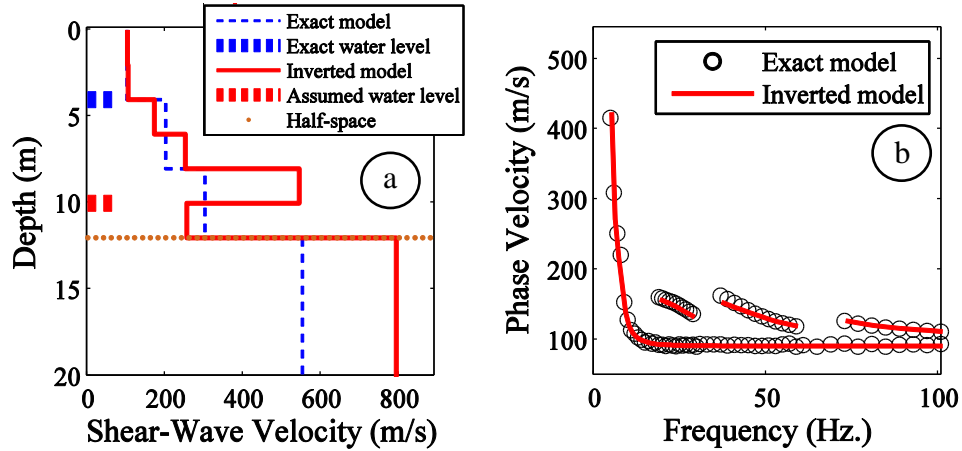
Figure 5.3. (a) Inverted model no. 6 (solid red) compared with the exact profile (dashed blue). Water levels between the inverted model and the exact one (red and blue bold dashed lines) are different between the profiles. (b) Dispersion curves for inverted (red line) and exact (circle) models are matching well, despite the difference between the models.
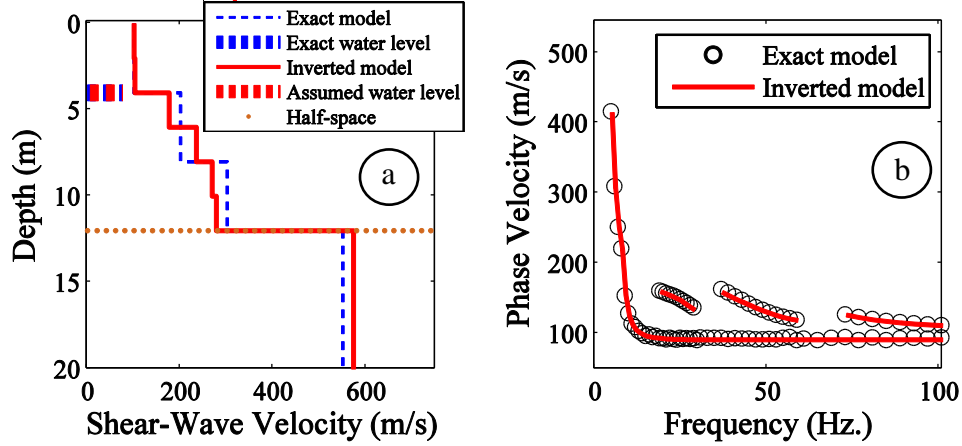
Figure 5.4. Similar to Figure 5.3, for inverted model no. 11.

It is observed that the dispersion curve for this profile matches well with the SEDC; however, the velocity profile no. 6 is very different from the exact model. On the other hand, Figure 5.4 presents the dispersion and the velocity structure for the profile no. 11. It is observed that the inversion procedure has been successful in terms of matching the theoretical dispersion curve of profile no. 11 with SEDC, as well as the water level and V_s of profile no. 11, and matches well with those from the exact profile. Therefore, the inversion of the phase velocity dispersion curve has provided two different inverted velocity profiles, both having a good match between their dispersion and SEDC, and therefore, without a knowledge of real V_s model (exact model), it is not possible to choose either of them as the final solution to the inversion. Consideration of higher modes cannot improve this observed non-uniqueness, as dispersion curves from profiles no. 6 and 11 are matching up to four modes with the SEDC.

In contrast to the dispersion curves, the synthetic time series from profiles no. 6 and 11 are very different and can be used as a tool to distinguish between the two profiles. Figure 5.5 shows synthetic seismograms generated from profiles no. 6 and 11 (red) plotted on top of the seismograms from the exact profiles (blue).
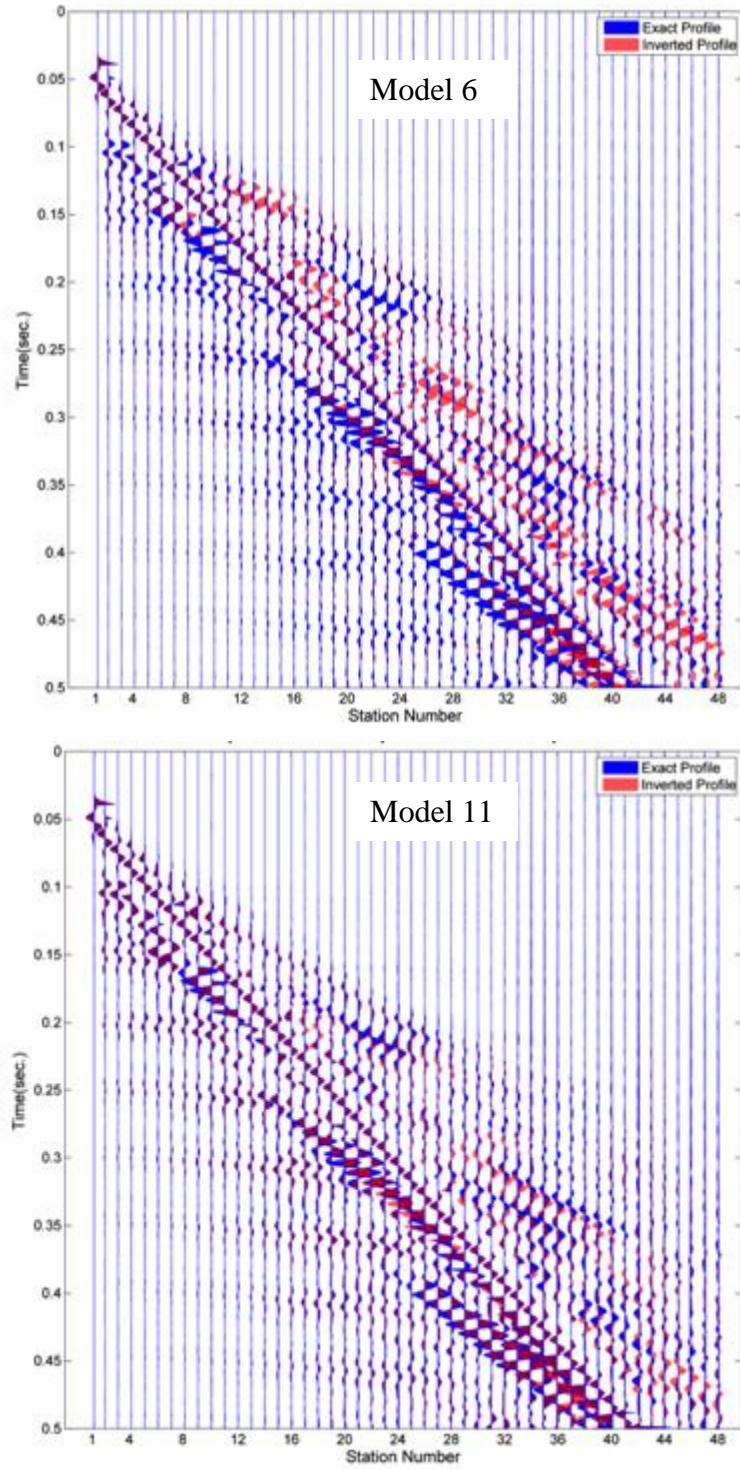
Figure 5.5. Comparison between synthetic time series from inverted profile no. 6 (top), and profile no. 11 (bottom) with the time series from exact model. Rayleigh wave train is scaled down for clarity.

For purposes of clarity, Figure 5.5 has been scaled differently for reflections, refractions, and direct waves compared to the Rayleigh wave train. It is evident that profile no. 11 has a better match between the seismograms, and can be selected as the final solution. In this synthetic example, attenuation is not considered; however, with the real data, it should be implemented.

To have a quantitative tool for the assessment of seismograms similarity, the zero-lag cross-correlation coefficient is used as an indicator of similarity. Results are provided in Figure 5.6, which shows that profile 11 has a better match with observed seismograms in most of the 48 geophones. Therefore, by comparing the synthetic seismogram it is possible to distinguish between the two different profiles that have similar dispersion curves and overcome the non-uniqueness problem of this example.
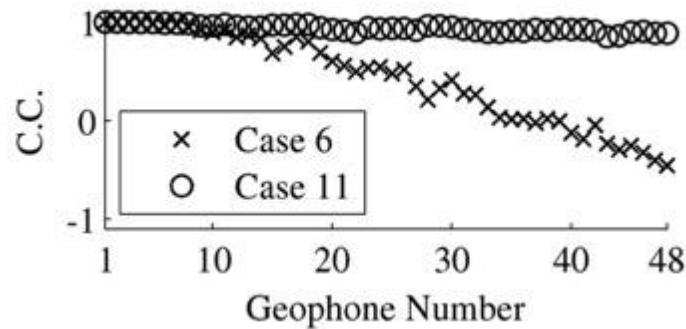
Figure 5.6. Zero-lag correlation coefficient (C.C.) for synthetics from models no. 6 and 11, correlated with the synthetics time series and those from the exact model.

6. Real World Data Analysis and Results

This chapter presents a real-world example problem through which the strength of the proposed procedure is discussed. The real-world example consists of a study site located in Memphis, Tennessee, two miles north of the Mississippi State border. The selected site is located on the top of a sedimentary deposit within the Mississippi embayment. The reason for the selection of this site is the possibility of amplification of seismic waves for certain frequency bands due to the shallow shear-wave velocity (V_S) contrast between soft and stiff materials and soil behavior (Kramer, 1996; Pujol *et al*., 2002; Malekmohammadi and Pezeshk, 2014). The amplification of ground motion could adversely affect the structures that resonate at periods similar to those of the ground on which they are built (Bodin and Horton, 1999). Therefore, to carry out the response analysis and seismic design at a particular site, all relevant information about the soil (e.g., shear-wave velocity profile) need to be correctly identified, which allows predicting the ground motion characteristics during earthquakes.
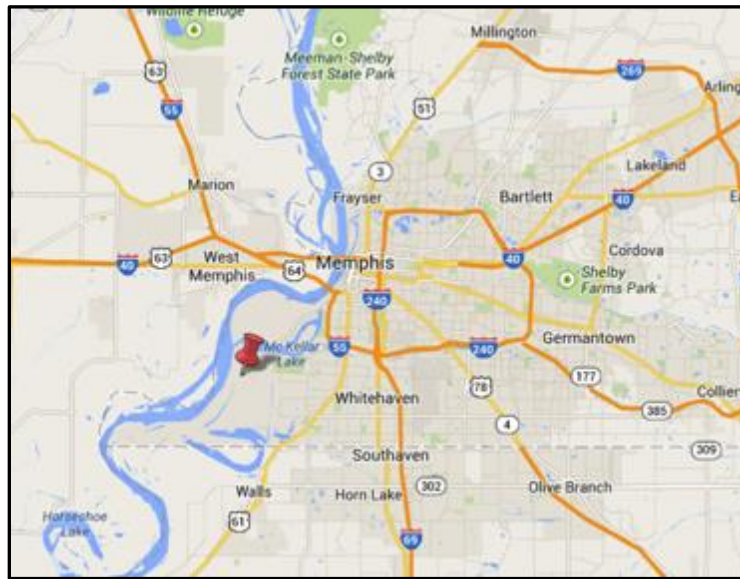

Figure 6.1. The MASW test location, near Memphis, Tennessee, in the vicinity of the Mississippi river.

6.1 The Experiment

The MASW experiment was performed to collect data from an array of 72 geophones. A geophone spacing of 0.9144 m (3 ft) was used. Furthermore, a sledgehammer was used as the source at the very first geophone. Vertical geophones (4.5 Hz) were used for this study. Regarding the large number of the geophones, it was decided to record data with

zero source-array offset for studying the source wavelet. Midpoint of the array is positioned exactly at the location of a borehole where downhole seismic survey was performed. The borehole located at the mid-span of the MASW spread is 30 m (100 ft) deep, and shear-wave velocities are available every 1.524 m (5 ft). The site is located at a remote area far from the road and man-made noise, which minimizes the contamination of data. The MASW experiment was repeated five times to increase the signal to noise ratio (SNR). Figure 6.2 shows the stacked observed seismograms and Figure 6.3 unveils its frequency content.
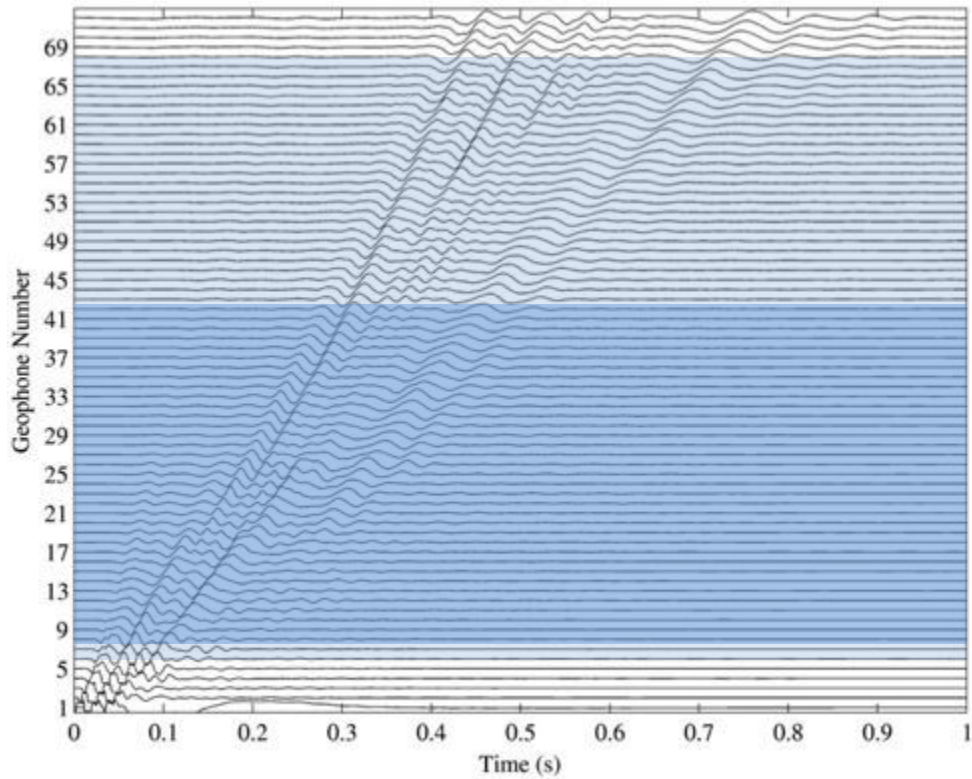
Figure 6.2. Time series recorded in the field from 72 geophones. Shaded areas are limitations used for geophone numbers in the calculation of dispersion curves. Recommendation for the ranges of geophones (such as those by Kansas Geological Survey) is indicated with bold color. However, using range of geophones indicated with the light color shade increases the resolution of the dispersion curve.
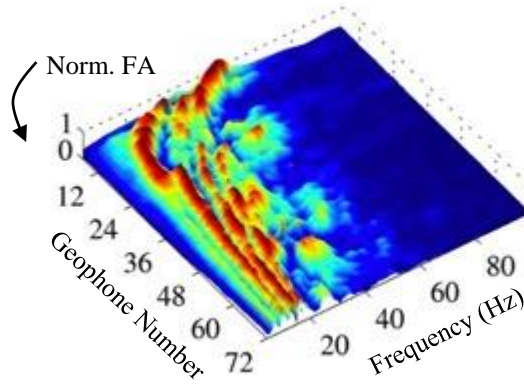
Figure 6.3. The frequency content of recorded time series presented in Figure 6.2. Fourier amplitudes (FA) are normalized at each geophone.

6.2   Experimental Dispersion Curve

It is common to filter observed seismograms to only contain a narrow frequency band centered on the frequency *f* by convolving them with the stretch function [Equation (4.2)]. After evaluating Equation (4.9), the phase velocity dispersion spectrum $\mathbf{P}(f,V_R)$ at one frequency is calculated from Equation (4.8) for a broad range of trial phase velocities, and then the whole process is repeated for another frequency. The spectrum $\mathbf{P}(f,V_R)$ then can be presented as a normalized three-dimensional contour (Figure 6.4). The experimental dispersion curve is picked from this contour by selecting points of high amplitude at each frequency. Such a dispersion curve is indicated with white circles in Figure 6.4b, which is a 2D representation of dispersion spectrum $\mathbf{P}(f,V_R)$. Geophone 7 (g_1=7) and geophone 66 (g_2=66) were used as the first and the last geophones to generate the dispersion spectrum and contour shown in Figure 6.4.
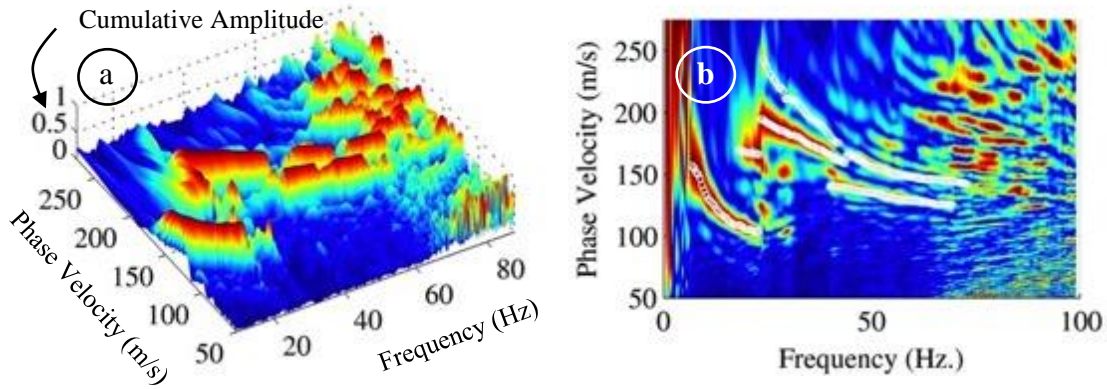
Figure 6.4. (a) Phase velocity spectrum $\mathbf{P}(f, V_R)$ *is plotted as a function of the phase velocity and frequency. (b) Two dimensional representation of the same spectrum in (a). The final phase velocity dispersion curve (white circles) is determined by picking high amplitude points.*

The Kansas Geological Survey recommends a minimum source offset and a maximum spread length in development of a dispersion curve to consider for the near- and far-field effects. In the study site, it is possible to go beyond these proposed limitations in the calculations to improve the resolution of the dispersion curve. The first and the last geophone numbers g_1 and g_2 in Equation (4.8) are related to the offset between the source and the first geophone in the array (x_1) and the array length (L). The offset (x_1) is recommended to be from one-fourth to one-fifth of the array length, and the array length is to be around the depth of investigation (Z_{max}). A Z_{max} equal to 30 m is considered for this study. Therefore, an array of the same length as Z_{max}, is chosen with 34 geophones. The offset is around 6 m, so neglecting the first 7 geophones results in the following geometry:

$$L = Z_{max} = 30m \simeq 34 \text{ geophones}$$
$$x_1 = L/5 = 6m \simeq 7 \text{ neglected geophones from the beginning}$$

(6.1)

A comparison is made between the dispersion contours obtained using the recommend geometry (geophones 8 to 41) as shown in Figure 6.5a, and a geometry considering geophones 7 to 66 (shown as white circles in Figure 6.5a) to see the effect of the recommended offset and spread length on the dispersion curve. If the dispersion curve is not negatively affected by a larger number of geophones, then it can help to distinguish higher modes better (Tokimatsu *et al.*, 1992). Comparing the white circles with the background contour in Figure 6.5a, it can be observed that the fundamental mode and some branches of the dispersion curve do not change with fewer numbers of geophones; however, it is observed that the contour loses its resolution in higher modes, and therefore, in depth. To inspect the lower resolution of higher modes, dispersion spectra from two geophone ranges 7-66 and 8-41 are plotted for frequencies from 10 Hz to 50 Hz, in 10-Hz increments on the same graph and shown in Figure 6.5b. It is evident that

the shorter spread of geophones is a smeared version of the longer spread. In summary, introducing a longer array and slightly shorter source offset does not change the overall pattern of the spectrum, but instead, increases the resolution.
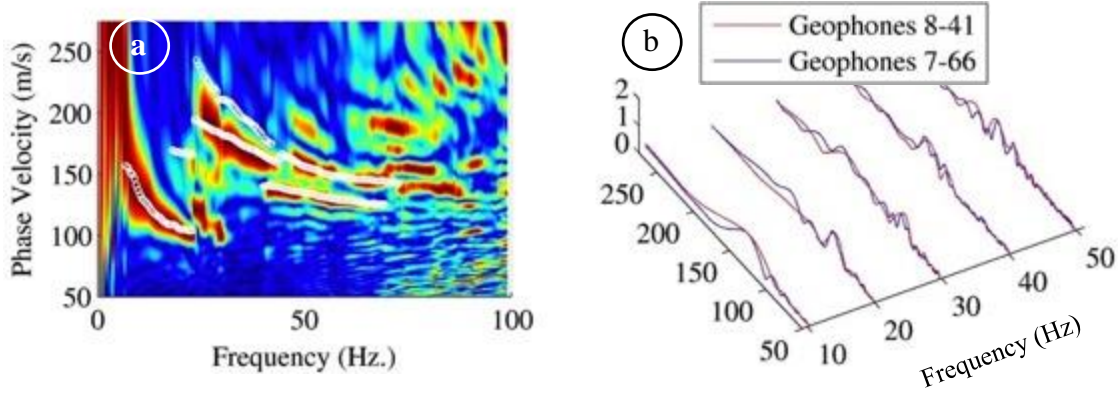

Figure 6.5. (a) Phase velocity dispersion contour from geophones series 8 to 41. The experimental dispersion curve from geophones 7 to 66 are plotted as white circles on top of it. (b) Three dimensional plots from spectrum contour at five sample frequencies for two ranges of geophones. The resolution of the spectrum reduces by decrease in the number of geophones.

High attenuation is expected in the study area as suggested and confirmed by Pujol *et al.* (2002) and *Ge et al.* (2009). Therefore, attenuation should be considered in the analysis process, and a detailed discussion of this is presented next.

6.3   Observed Attenuation

Recorded time series are used in an inversion process similar to that by Pezeshk and Hosseini (2013), Hosseini *et al.* (2014; 2012), Conn *et al.* (2012), and McNamara *et al.* (2012) to estimate the attenuation for various frequencies. Seismic characterization techniques are also used in other engineering fields to describe the properties and behavior of the medium (Hosseini, 2013; Hosseini and Aminzadeh, 2013; Hosseini *et al.*, 2013; Olson *et al.*, 2011; Kafash *et al.*, 2013). The procedure simply accounts for the drop in amplitude generated by the sledgehammer as it travels its way through the medium to the geophones. Two phenomena are considered for the amplitude drop: (1) geometric spreading with decay rate of $1/\sqrt{R}$ where R is the distance between source and geophone, and (2) anelastic attenuation described by:

$$\gamma(f) = \frac{\pi f R}{Q(f)U(f)} \tag{6.2}$$

where f is the frequency for which the quality factor is being investigated, $Q(f)$ is the frequency dependent quality factor, and $U(f)$ is the group velocity. It is possible to use the experimental attenuation coefficient $g(f)$ in the surface wave inversion process along

with the experimental phase velocity dispersion data to simultaneously invert for V_s and Q structure (Lee and Solomon, 1978; Malagnini, 1996; Taylor and Toksöz, 1982). Such an inversion was performed, but reasonable values for the inverted Q structure were not obtained. Malagnini (1996) made the same observation where he did not get stable attenuation coefficients in the inversion process along with the V_S model. Therefore, in this study, only V_s was considered as unknown in the inversion process and the quality factor was considered as a known parameter.

Group velocities in Equation (6.2) are extracted from time series recorded from each geophone. Following Malagnini (1996), the group velocities from geophone #36 was chosen for its "appropriate looking" curve. Figure 6.6 shows the group velocity curve for geophone #36 obtained using the multiple filter technique (Dziewonski et al., 1969; Hales, 1972; Herrmann, 1987).
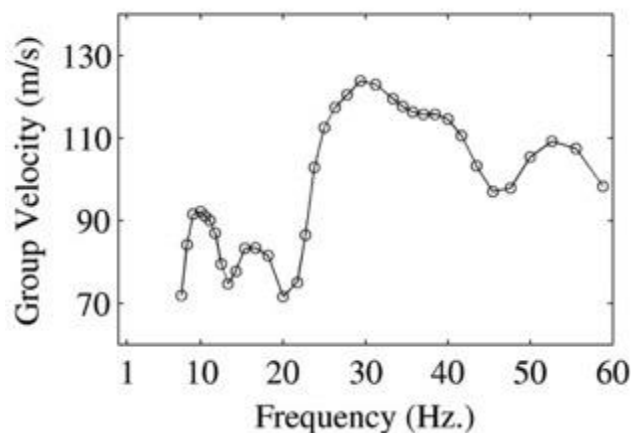

Figure 6.6. Group velocities from multiple filter technique, estimated from geophone #36.

The result of the inversion for the quality factor Q is presented in Figure 6.7. From this figure, it can be observed that the Q factors are unreliable due to erratic spikes in certain frequencies, because of numerical instability of the inversion for these frequencies. Quality factors selected to be used for the remainder of this study are shown by "X" markers in Figure 6.7. The average of the selected quality factors is about 25, which is in the range reported by Ge *et al.* (2009) and Pujol *et al.* (2002). We considered equal compressional and shear-wave quality factors ($Q = Q_\alpha = Q_\beta$) (Malagnini, 1996) and set them to 25 in the rest of the analysis. A slight difference in the quality factor does not lead to a drastic change in the shape and the frequency content of the pulse, but only modifies the arrivals of the wave with respect to induced attenuation dispersion. Therefore, an analysis process is implemented to account for the slight difference in the arrival times while comparing the observed and synthetic time series.
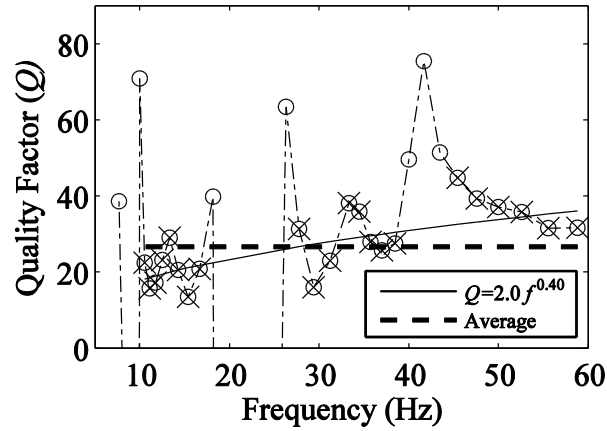
Figure 6.7. Inverted quality factors versus frequency.

6.4   Inversion

To understand various considerations for the inversion process, it is important to identify high mode contributions. As an example, Figure 6.8 shows the experimental dispersion curve obtained using the MASW experiment at the study site. This dispersion curve possesses six different branches. It is not obvious which mode number each branch represents. Table 6.1 represents 22 different possibilities of various modes assigned to branches of the experimental dispersion curve. For example, in case C1, Branch B1 represents the fundamental mode, Branches B2 and B3 represent the second higher mode, Branch B4 represents the third higher mode, and Branches B5 and B6 represent the fourth higher mode.
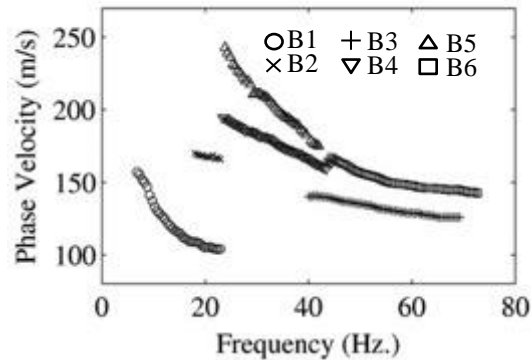

Figure 6.8. The experimental dispersion curve consisting of six branches used in the inversion process.

Table 6.1. Twenty two combinations for mode number assignment to each branch of the experimental dispersion curve. Mode numbers change from 0 (fundamental mode) to 7 (7th higher mode). Dash means that that specific branch is not used.

| | | | | Branch Numbers | | | |
		B1	B2	B3	B4	B5	B6
Case Numbers	**C1**	**0**	**2**	**2**	**3**	**4**	**4**
	C2	0	2	3	4	5	5
	C3	0	1	1	2	3	3
	C4	0	1	2	3	4	4
	C5	0	2	2	3	-	4
	C6	0	2	3	4	-	5
	C7	0	1	1	2	-	3
	C8	0	1	2	3	-	4
	C9	**0**	**-**	**-**	**-**	**-**	**-**
	C10	0	-	-	3	4	4
	C11	0	-	-	4	5	5
	C12	**0**	**-**	**-**	**2**	**3**	**3**
	C13	0	-	-	3	-	4
	C14	0	-	-	4	-	5
	C15	**0**	**-**	**-**	**2**	**-**	**3**
	C16	0	-	-	5	-	6
	C17	0	-	-	-	-	3
	C18	**0**	**-**	**-**	**-**	**3**	**3**
	C19	0	-	-	-	-	4
	C20	0	-	-	-	-	5
	C21	0	-	-	-	-	6
	C22	0	-	-	-	-	7

Not all of the 22 cases yielded a reliable dispersion inversion. Such a mismatch shows that the assigned mode number for the experimental dispersion curve is not appropriate. Figure 6.9 shows an example of a dispersion curve inversion where the selected mode number for the experimental dispersion curve branches is not appropriate. From 22 cases, five have acceptable inversion quality (bold in Table 6.1), and were selected for further investigation. This is another source for non-uniqueness of the solution, if after inverting dispersion curves from five cases; different shear-wave velocity profiles are obtained.
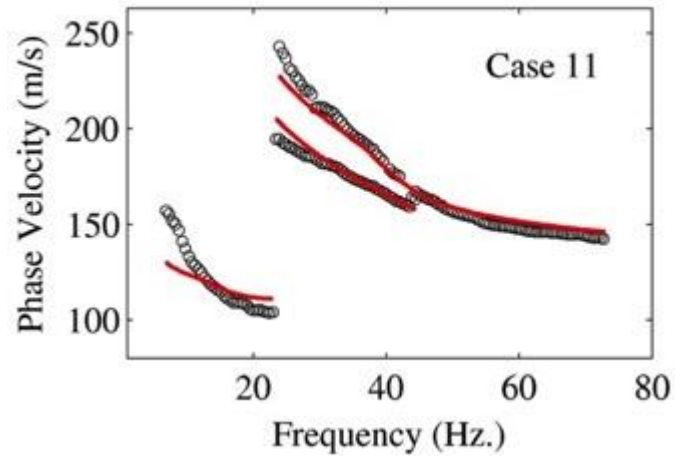
Figure 6.9. Low quality of match between the theoretical (red line) and experimental (black circles) dispersion curves indicates that the mode numbers assigned to the branches of the dispersion curves is not appropriate.

The five selected dispersion curves with assigned mode numbers to various branches as highlighted in Table 6.1 are inverted. The number of iterations and damping ratios are considered in such a way that the errors of each iteration step becomes less as the number of iterations increases. The threshold error is selected to be around 1.2 to 1.5 percent for the final iteration, and damping ratios are selected manually for each case. The five profiles, as provided in Figure 6.10, show that there is no way to discriminate one profile over another by relying only on the available dispersion data. The goodness of fit between the theoretical and the experimental phase velocity dispersion data, along with the damping ratio, and the error for different iterations are provided in Figure 6.11 and Figure 6.12.
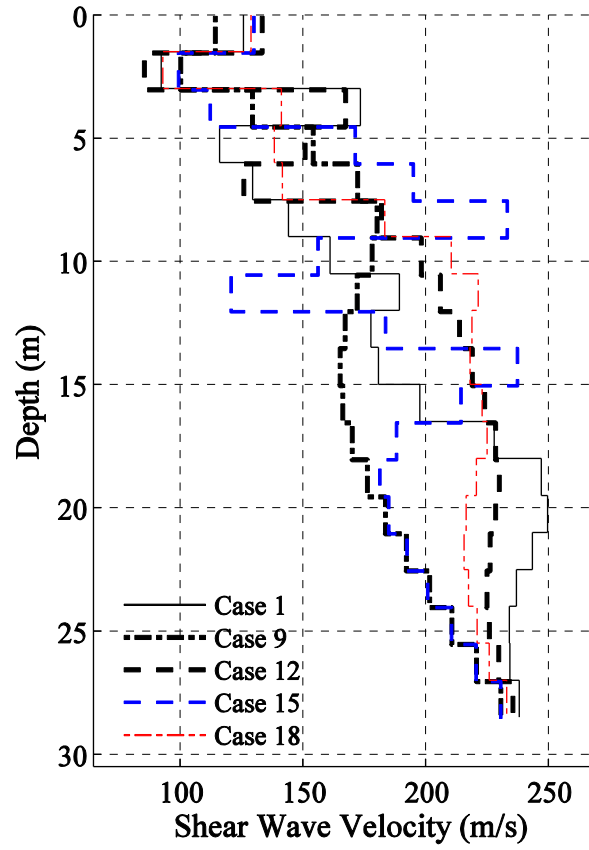
Figure 6.10. Five shear-wave velocity profiles from inversion of cases 1, 9, 12, 15, and 18.

Next, synthetic seismograms are generated for each of the five velocity profiles presented in Figure 6.10 to help with the selection of the best profile and to improve the non-uniqueness. Synthetic time series are compared with the recorded time series from the geophones, and it is anticipated that by comparing the similarity between the synthetics and observations, it will be possible to identify the best shear-wave velocity profile among those presented in Figure 6.10.
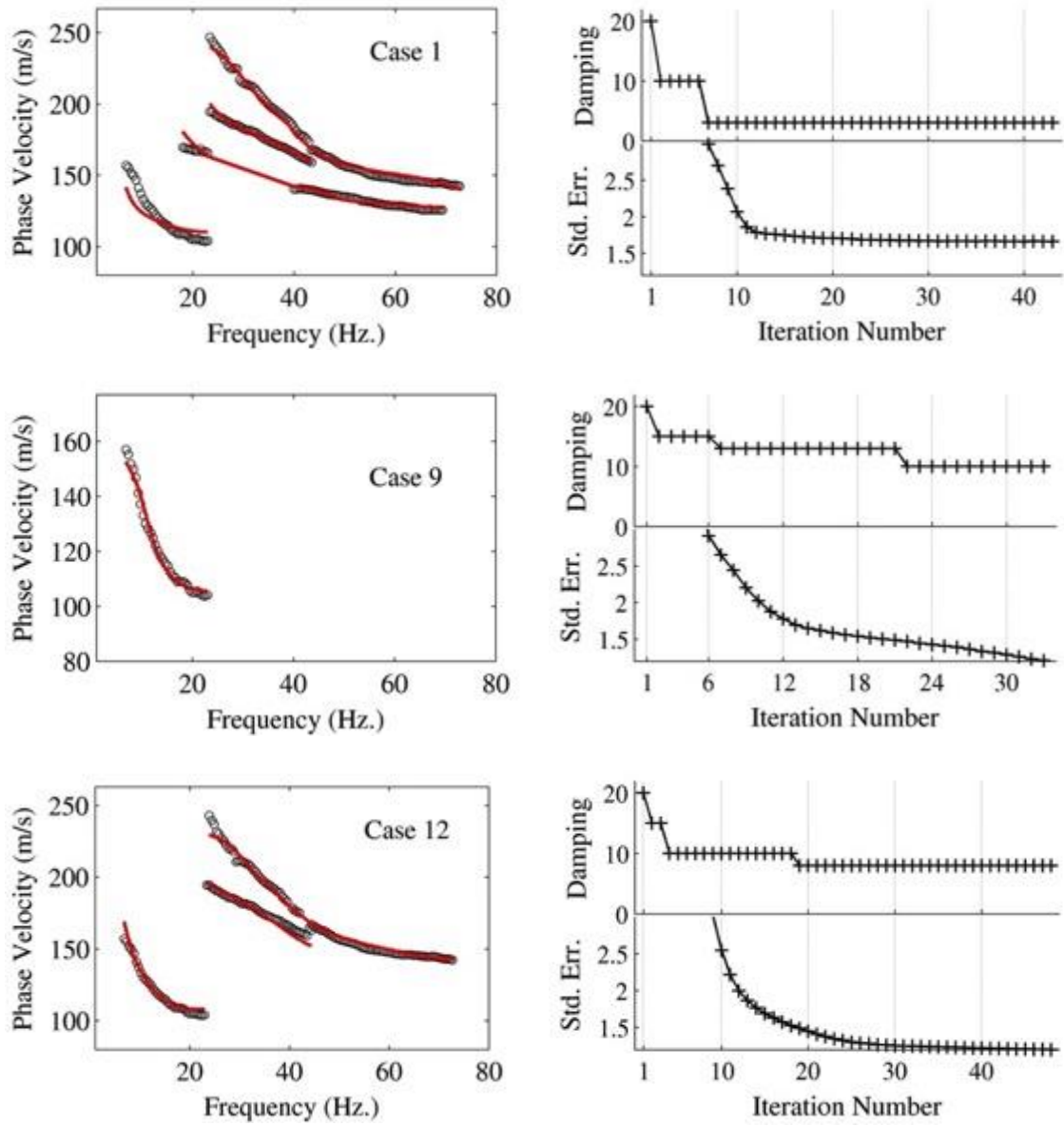
Figure 6.11. Details of inversion for Cases 1, 9, and 12. Left column shows the theoretical and the experimental dispersion curves. Right column shows the corresponding standard error and damping factor for each iteration in the inversion process.
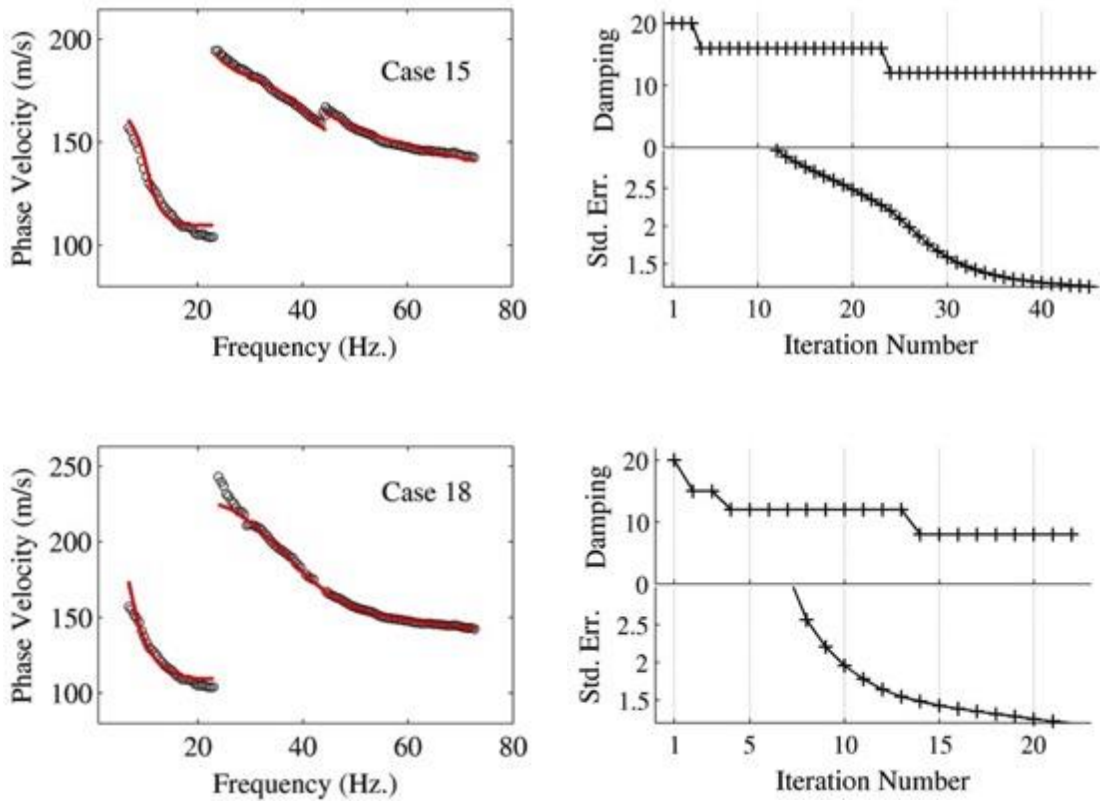
Figure 6.12. Similar to Figure 6.11 for Cases 15 and 18.

6.5   Synthetic Time Series

Synthetic full waveforms are useful in realistic simulation of the ground motion where direct waves, reflections, refractions, and surface waves are all included. The wavenumber integration technique (Wang and Herrmann, 1980) is used to generate synthetic seismograms from the V_S profiles provided in Figure 6.10. Corresponding V_P profiles are calculated from V_S by considering a Poisson's ratio of 0.45. As shown in Figure 6.10, there are a total of 19 layers over a half-space. Time series are generated for a length of 10.24 seconds with a time step (Δt) of 0.005 seconds. A quality factor of 25 in all layers is assumed, and the Futterman (1962) causal Q operator is implemented as a complex velocity term in the wavenumber integration technique (Herrmann, 1987). After experimenting with different reference frequencies, a reference frequency of 1.0 Hz seems to produce synthetics matching the observations better than any other value for all five cases. Synthetic seismograms are generated and compared with observations for geophones #6 through #72. Velocity impulse response is produced by assuming a parabolic source with the base length of $4\Delta t$ and then differentiating the time series with respect to time (private communications, Dr. Herrmann). Impulse responses are then convolved with a half cycle sinusoidal source wavelet with a frequency of 60 Hz.

6.6 Comparison Between Observed and Synthetic Time Series

Cross-correlation is used as a tool to compare the similarity of synthetic and observed time series. Cross-correlation is used in the following equation to calculate the "match ratio" between the synthetic (f) and observed (g) discrete data (Anderson, 2004; Taborda and Bielak, 2013):

$$
MR = \left[\frac{\sum\limits_{i}^{N} f_i g_i}{\left(\sum\limits_{i}^{N} f_i^{\,2} \right)^{\frac{1}{2}} \left(\sum\limits_{i}^{N} g_i^{\,2} \right)^{\frac{1}{2}}} \right] \tag{6.3}
$$

It is logical to use a zero time-lag cross-correlation value in the Equation (6.3); however, this might lead to a partially unreliable assessment of goodness of fit. There are several sources of uncertainty in the inverted velocity model and, therefore, in the ensuing synthetic seismograms. The very first item affected by the uncertainties in the experimental dispersion curve and its inversion is the inverted velocity profile. Therefore, the arrival time of waves in the synthetic seismogram may not be accurately computed. To solve this problem, the uncertainty in the arrival time of surface waves is assumed to be related to the mismatch between the experimental and theoretical dispersion curves. Therefore, it might be more logical for our study to calculate cross-correlation values for a range of positive and negative time-lags; i.e., to shift the synthetic seismograms forward or backward with respect to the observation until the maximum match ratio between the signals is reached. The time range over which to shift the synthetics is assumed to be related to the maximum percentage of the error in the dispersion curve inversion. The whole idea is to allow the seismogram to shift slightly in time so it can match the observation in the best possible way under a constraint on the shift amount. Figure 6.13a shows this concept, where a synthetic time series is plotted against the observation. The match ratio based on zero time-lag cross-correlation gives an absolute value of 0.12. Figure 6.13b and Figure 6.13c show that by having an estimation of arrival time uncertainty percentage (ϵ), it is possible to calculate cross-correlation for a time-lag ranging from $t_0(1 - \epsilon)$ to $t_0(1 + \epsilon)$. Provided in Figure 6.13d, the best match occurs when the original arrival t_0 is moved to t_f resulting in a match ratio of about 0.64. After applying such a correction as shown in Figure 6.13d, the match ratio increased about 530 percent compared to its initial quality of match of 0.12.
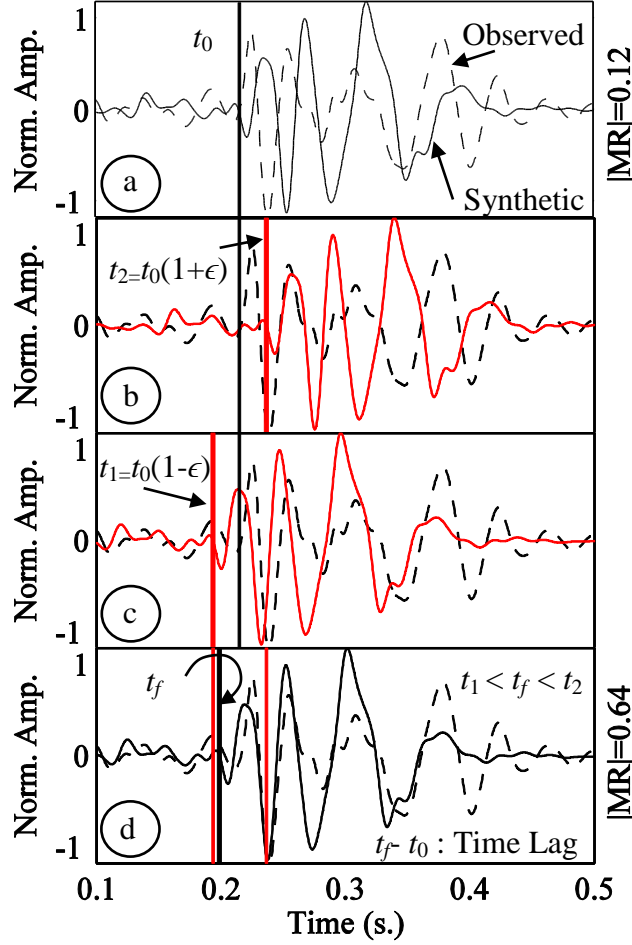
Figure 6.13. (a) Observed time series (dashed lines) and corresponding synthetic (solid lines) ones are not exactly aligned on top of each other due to the late first arrival t_0 in the synthetic. The synthetic is then allowed to shift backward and forward in a limited time frame to achieve the best match ratio with observation. Before shifting, the absolute of the match ratio (MR) is about 0.12. Maximum (b) and minimum (c) time shift allowed for the synthetics as a function of t_0 and ϵ (maximum error of dispersion inversion). (d) Best match ratio is occurring at time t_f showing that absolute of match ratio increases to 0.64, when the synthetics are shifted ($t_f - t_0$) seconds. Red lines distinguish the allowed time range over which the synthetic seismogram is allowed to move.

By applying such a concept to all cases, one can make a better judgement about the realistic degree of match between the synthetic and observed time series. Such a technique can be applied in two ways: (1) by allowing observed and synthetic time series to shift in time with respect to each other, separately for each geophone, or (2) by applying an equal amount of time shift to synthetic time series from all geophones. In the next two sections, these two techniques are introduced and applied to the data and results of match are provided. The second method that time shift is equal for all geophones seems to be a more logical approach for seismogram comparison. It will be shown that the two techniques yield the same answer.

6.7 Free Time Shift of Time Series at Each Geophone

For time series at several geophones, the match ratio as a function of time-lag can be presented as a contour for each case. In Figure 6.14, such a contour is shown for Case 12. From this Figure, it can be observed that the best match between synthetics and observations for most of the sensors occurs when the synthetic time series are slightly moved in time with respect to their original position.
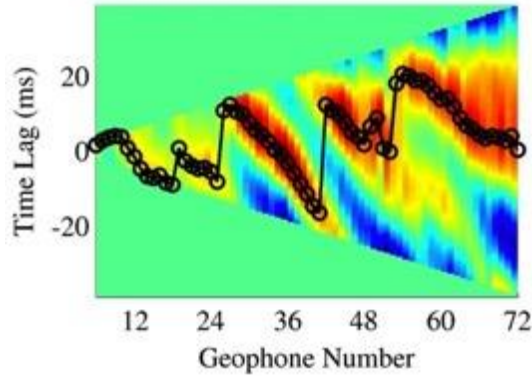

Figure 6.14. Match ratio as a function of time lag at each geophone for Case 12 with a maximum dispersion inversion error (σ) of about 12 percent. Lower and upper bounds for time lag are calculated as 12 percent before and after the Rayleigh wave arrival in the synthetic time series. Color scale shows maximum correlation with red and minimum value with blue.

It should be noted that in Figure 6.14, geophones closer to the source have a narrower range of allowed time-lag compared to farther ones. The maximum values of match ratio for each geophone are picked in the allowed range, as shown with circles in Figure 6.14. The match ratio obtained for each of the five cases is compared as an indicator guide to select a representative shear-wave velocity profile. Figure 6.15 shows the match ratios for cases 1, 9, 12, 15, and 18. For each case, the match ratios are averaged over 72 geophones and shown on the right-hand side of Figure 6.15 with a set of horizontal lines. The one with the highest match ratio represents the case with the best soil profile. It is observed that, based on synthetics, cases 12 and 18 have the highest match ratios and are very close to each other. Since cases 12 and 18 have very close match ratios, they must have soil profiles, which resemble each other, as, can be seen in Figure 6.10.
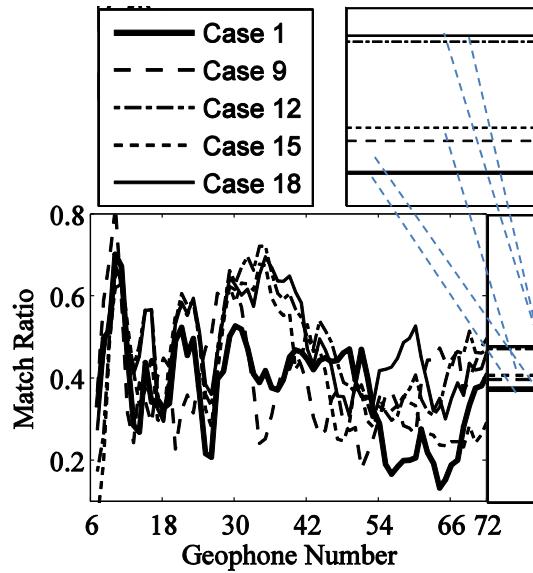
Figure 6.15. Match ratio at each geophone for different cases are compared. The average match ratios are plotted on the right hand narrow window. Cases 12 and 18 are close in the average match ratio values.

Figure 6.16 shows the synthetic seismogram (solid line) plotted on top of the observed ones (dashed line) for case 12. Figure 6.17 shows the same version of the previous figure, except that the synthetic time series are shifted in time to the position where the match ratio is a maximum, according to Figure 6.14. To have a better view for visual comparison, Figure 6.18 presents the shifted synthetic and observed time series, where both sets of time series are plotted after an arrival time corresponding to a reduction velocity of about 160 m/s. Such an onset after which the time series are plotted can be observed in both Figure 6.16 and Figure 6.17 as a sloped line.
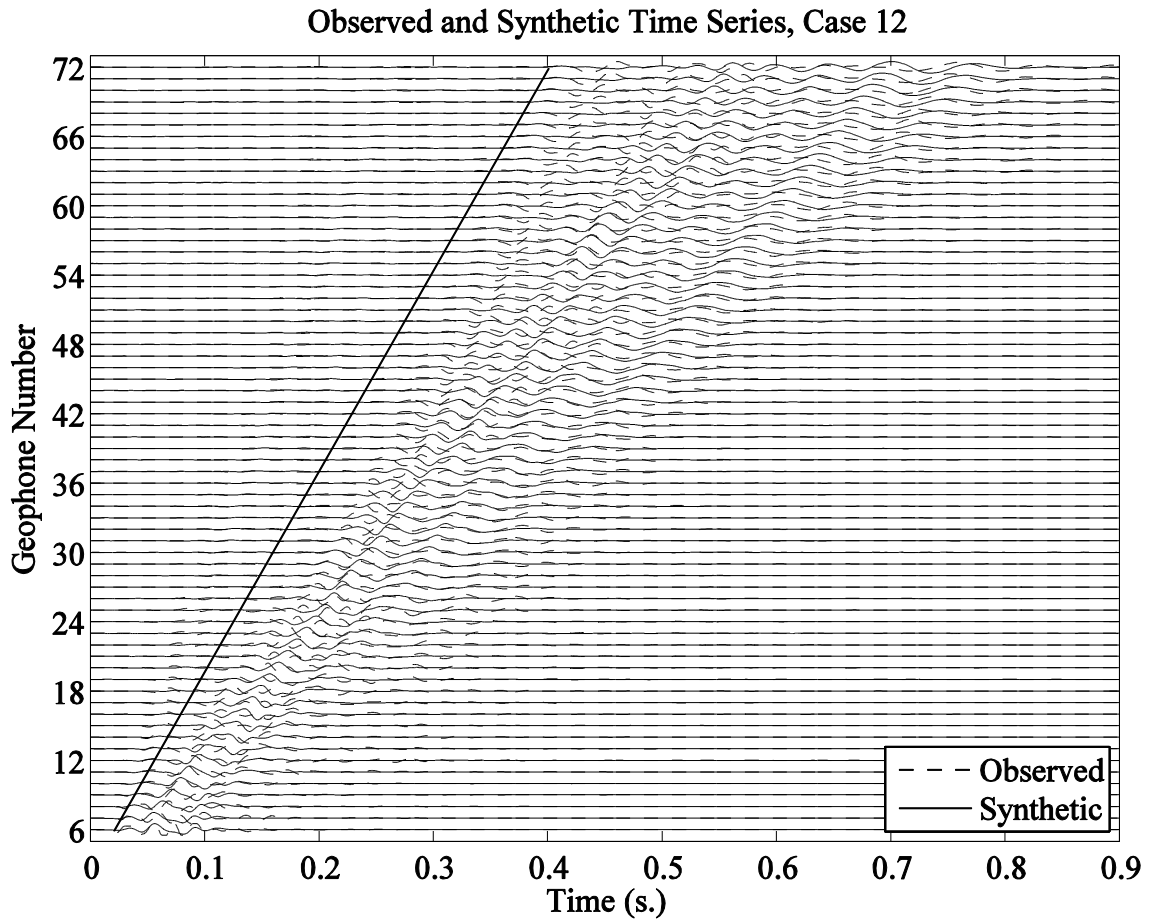
Figure 6.16. Observed (dashed lines) and synthetic (solid line) time series for case 12. The sloped line presents a velocity of about 160 m/s which will be used to plot time series after the line in following figures.
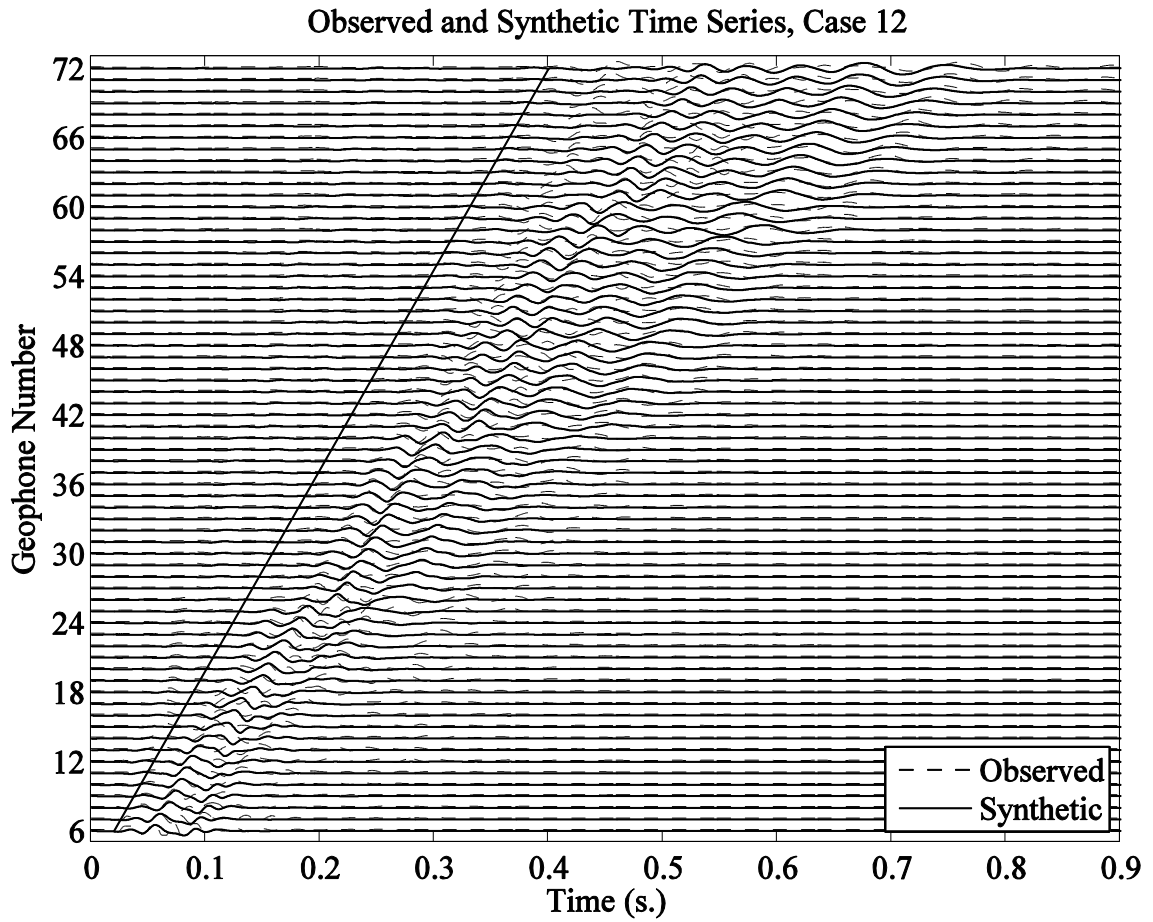
Figure 6.17. Same as Figure 6.16, except that synthetic time series are shifted according to the time-lags for maximum match ratio in Figure 6.14.
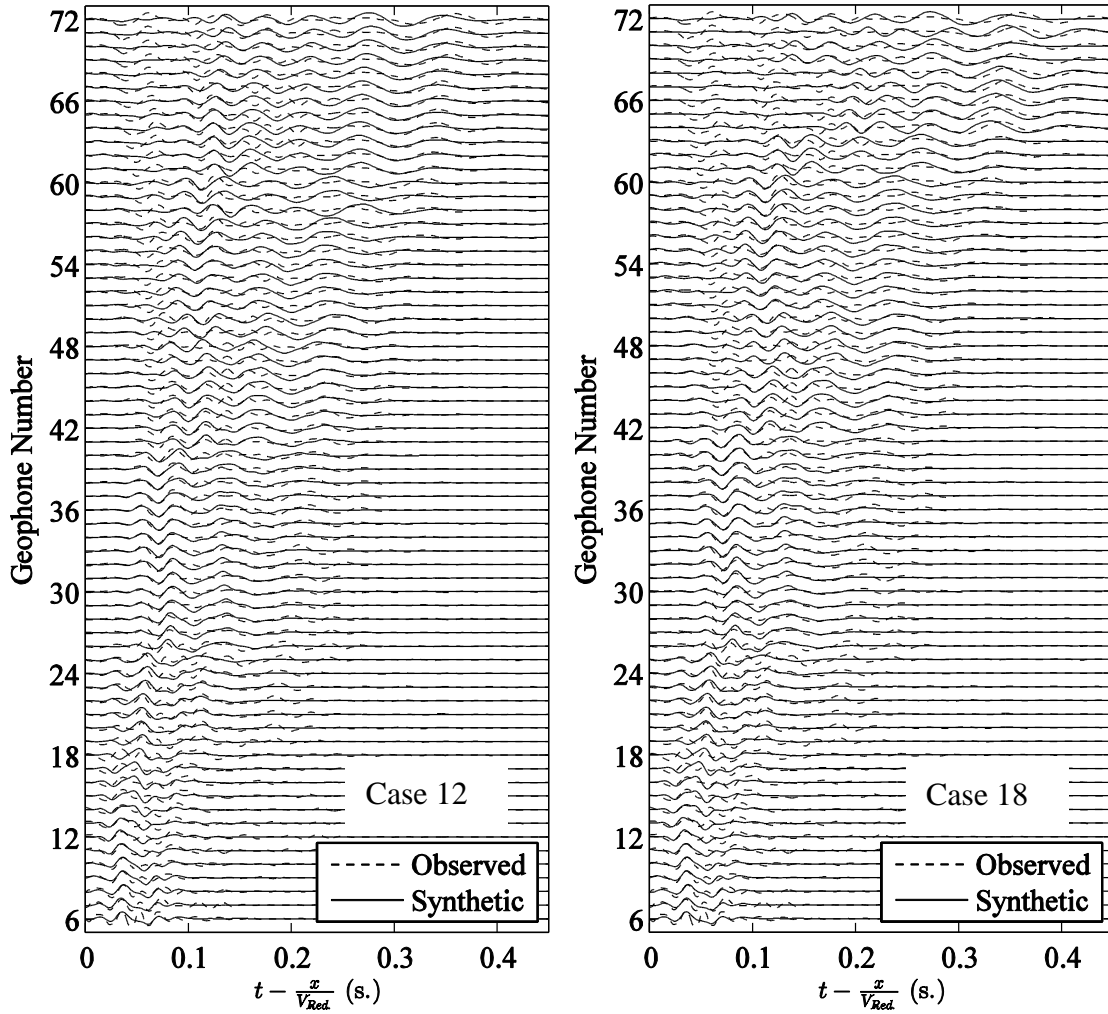
Figure 6.18. Observed (dashed lines) and shifted synthetic (solid lines) time series for Case 12 (left) and Case 18 (right). A reduction velocity of 160 m/s is used to plot time series corresponding to the sloped line in Figure 6.16.

Based on the discussion above, two profiles (Cases 12 and 18) have been identified with the highest average match ratio between their corresponding synthetic seismograms and observed time series. From Figure 6.10, it is evident that Case 12 and Case 18 both have very close shear-wave velocity profiles, and both profiles may be considered as an accurate model for the study site. For validation purposes the shear-wave velocity profiles associated with cases 12, 18, and their average are compared with the results from the downhole seismic survey.

6.8   Equal Time Shift of Time Series at All Geophones

In this case, observed time series from all geophones are equally time-shifted with respect to the synthetic ones. Using a cross correlation technique, the similarity between the observations and synthesis with an equal amount of shift can be easily assessed. Figure 6.19 shows the mean of cross correlation coefficients at all geophones (from 6 to 72) for different time lags and for five different cases (Cases 1, 9, 12, 15, and 18). To find out the best shift in time, the average of mean correlation coefficient is plotted as a curve on the top of Figure 6.19 and the time lag associated with the maximum average coefficient (shown with circle) is used as a suitable time lag to be applied to all geophones for all cases. Note that amount of time shift is equal among all geophones and all cases.

At the specific time-shift mentioned above, the mean cross correlation coefficient is plotted for five cases in 6.20 and it is observed that Case 12 and Case 18 have maximum match between their observed and synthetic time series. This result agrees with that from the alternative technique in previous section in which time series are allowed to move freely at each geophone.
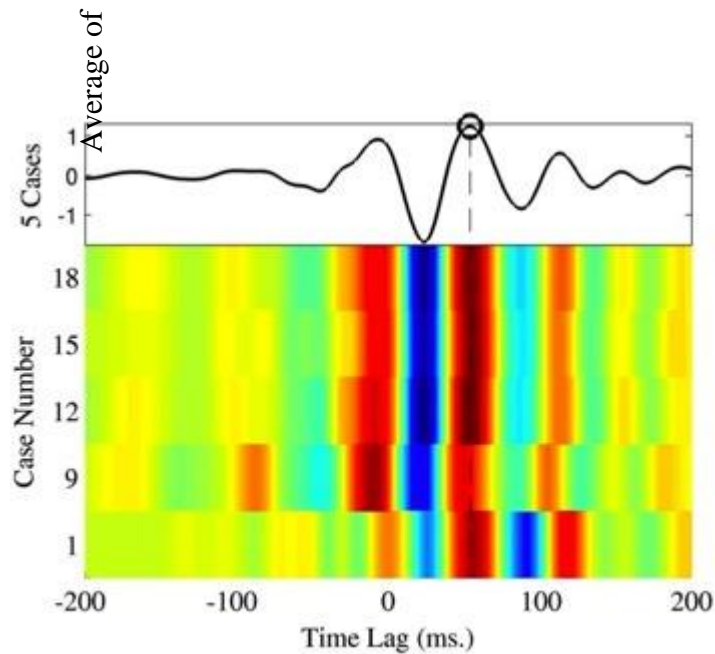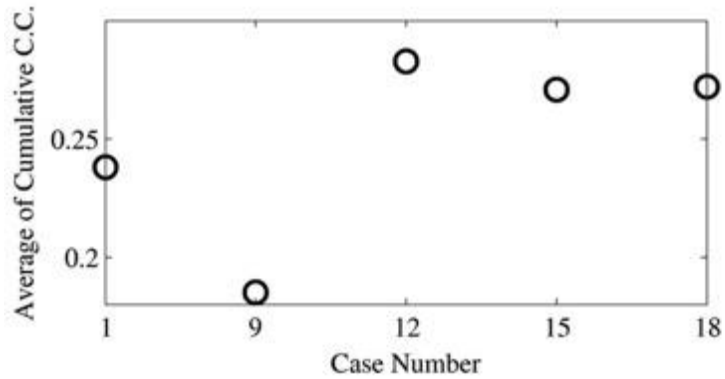

Figure 6.19. Mean cross correlation coefficient as a function of time lag for five cases (bottom contour). The average of mean cross correlation coefficient for five cases are used to find the best amount of time shift.

6.20. Mean cross correlation coefficient at the time lag associated with maximum average mean cross correlation coefficient.

6.9   Comparing MASW V_S with the Downhole Velocity Profile

The downhole seismic survey is performed using two geophones, five feet apart, lowered into a borehole every five feet. A pneumatic source capable of generating shear-waves is located at the ground surface close to the borehole. Shear-waves are generated twice in two opposite directions and recorded by two borehole geophones and one surface geophone (Figure 6.21).
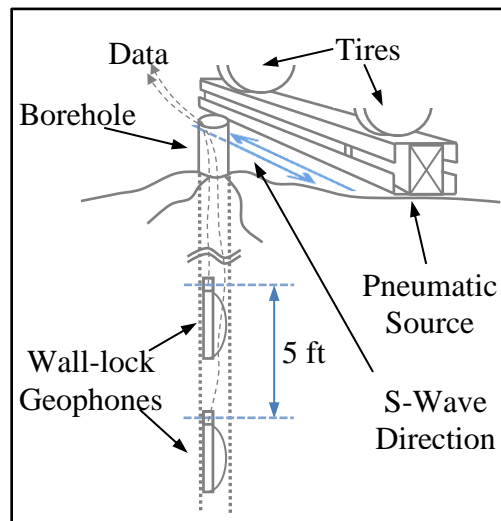

Figure 6.21. Schematic view of the downhole seismic survey.

Recorded data from the borehole geophones are used to pick first arrivals and calculate the shear-wave velocity of layers at five-foot intervals. It should be mentioned that the shear-wave velocity estimated for the top three layers is not reliable considering the loose confinement around the borehole PVC pipe. To illustrate this,

Figure 6.22 shows the shear arrivals recorded on one of the horizontal channels of the borehole geophone, and it is observed that the arrival time is lower in the second layer, than the first layer.
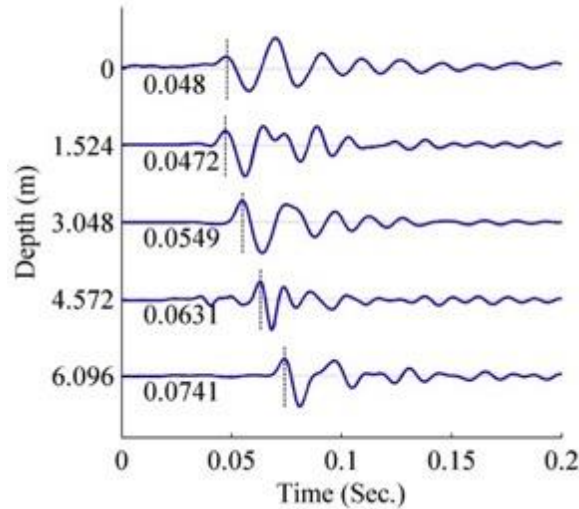

Figure 6.22. Arrival times recorded in one of the borehole geophones, horizontal channel #1. Arrival of the second layer is earlier than the layer above.

The shear-wave velocity is determined by the analysis of arrival times and is plotted against the profiles from the surface wave inversion (Figure 6.23). It is observed that V_S profiles from Case 12 and Case 18 match the downhole results well, as was expected due to the agreement between the synthetic and observed time series shown in Figure 6.15. Figure 6.23 shows the result from inversion of the fundamental mode only as well (Case 9), showing that for a reliable inversion higher modes must be present in the experimental phase velocity dispersion curve.
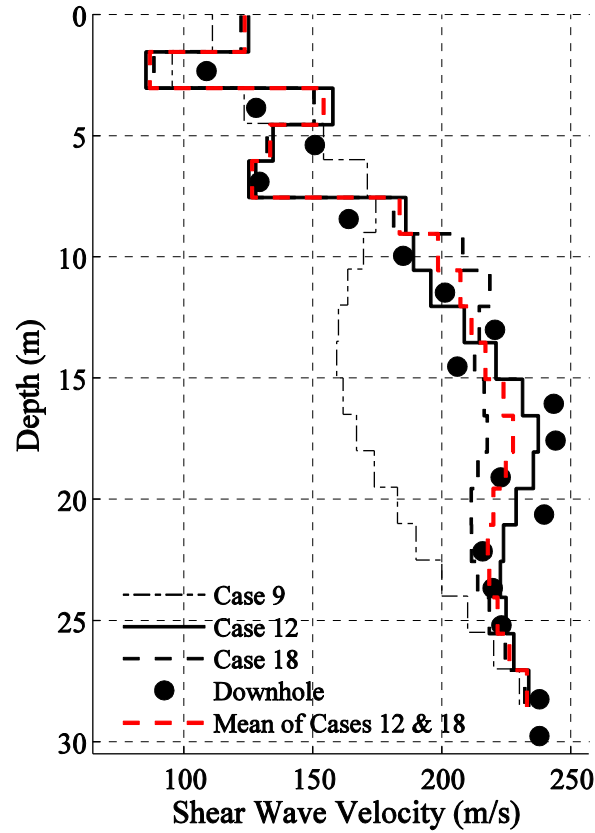
Figure 6.23. The inverted shear-wave velocity profiles (Case 9, Case 12, Case 18, and average of Cases 12 & 18) and the profile from the downhole seismic survey. Downhole profile is in close agreement to cases 12 and 18 as predicted by the synthetic match.

It is useful to compare the similarity between the downhole velocity profile and those from the surface wave inversion. Table 6.2 compares the profiles from the surface wave estimation and borehole measurements using five different criteria proposed by Xia et al. (2000). Table 6.2 contains the data for the inverted velocity profiles from Case 12, Case 18, and their average compared against the downhole measurements. From Table 6.2 it can be concluded that all five criteria in this study for all three cases of inversion are close to the lowest values reported by Xia et al. (2000) in their comparison between their inversion and their downhole measurement, indicating an acceptable match between the downhole and inverted velocity profiles.

Table 6.2. Comparison of inverted velocity profiles with borehole measurements.

Inverted Profile	Maximum difference (m/s)	Average difference (m/s)	Maximum relative difference (m/s)	Average relative difference (%)	Standard deviation (m/s)	Depth studied by MASW (m)	Inverted velocity range (m/s)
Case 12	28.3	10.8	10.8	4	8.8	30	83-250
Case 18	31.5	12.7	12.0	5	9.9	30	89-246
Average	29.9	11.5	11.4	5	8.9	30	86-247

Terminology used in this table: 1. Maximum difference $D = \max_{1 < j < n} \left| V_b - V_i \right|_j$, where V_b is S-wave velocities from borehole measurement, V_i is S-wave velocities inverted from Rayleigh wave phase velocities, and n is the number of layers. 2. Average difference $\underline{D} = 1/n \sum_{k=1}^{n} \left| V_b - V_i \right|_k$. 3. Maximum relative difference $R = 100 * D / (V_b)_k$, where $(V_b)_k$ is the S-wave velocity from borehole measurement associated with D. 4. Average relative difference $\underline{R} = 100/n \sum_{k=1}^{n} (\left| V_b - V_i \right| / V_b)_k$. 5. Standard deviation $S = \left[1/2n \sum_{k=1}^{n} \left| V_b - V_i \right|_k^2 \right]^{1/2}$. Structure and terminologies in this table is borrowed from Xia et al. (2000).

6.10 Comparing MASW V_S with Velocity Profiles in the Literature

The location of the study site suggests that its geology may be similar to sites located in Marked Tree, Arkansas, and Risco, Missouri. The geology of these sites consists of Holocene Mississippi river floodplain sand, silt, and gravel (Liu *et al*. 1997). Liu et al. (1997) performed downhole seismic surveys at three locations in the Mississippi embayment and determined the shear- and compressional-wave velocities at the boreholes. Boreholes for Marked Tree and Risco are 36 m and 27 m deep and readings are repeated every 0.91 m. Later, Rosenblad *et al.* (2010) studied surface wave measurements in the Mississippi embayment at 11 sites and used a swept frequency device capable of generating low frequency harmonic waves. They estimated the velocity profiles for a depth of about 200 m. Rosenblad *et al.* (2010) confirmed the shear-wave velocity profiles reported by Liu *et al.* (1997). In this study, due to the geological similarity, the inverted shear-wave velocity profile (the average of profiles from cases 12 and 18) is compared with Liu *et al.* (1997) and Rosenblad *et al.* (2010) results from sites located in Marked Tree, Arkansas, and Risco, Missouri (Figure 6.24).
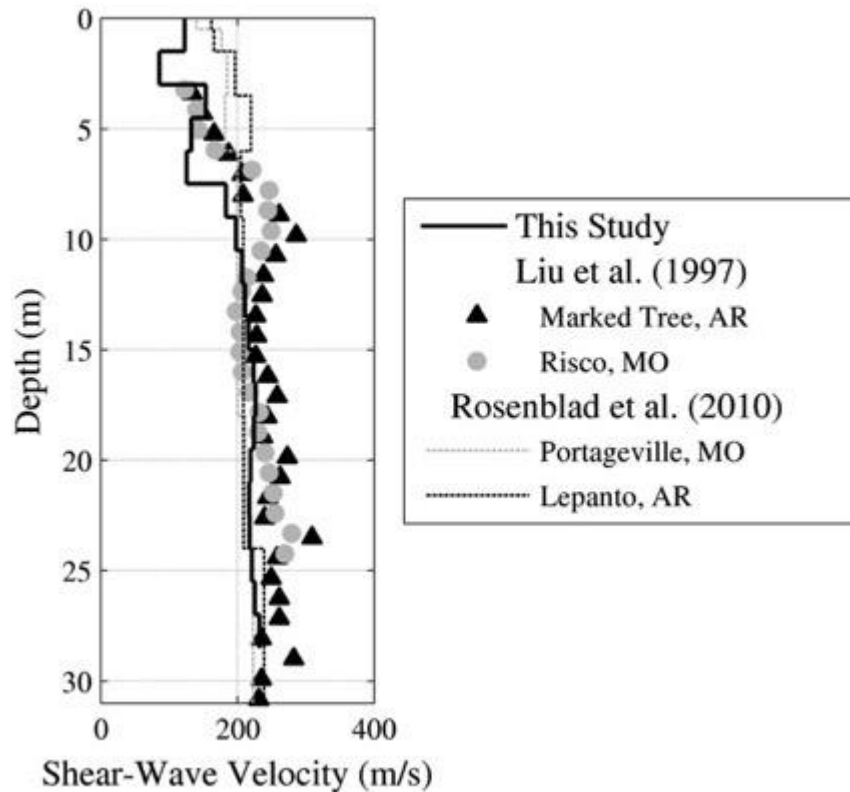
Figure 6.24. Obtained shear-wave velocity profile in this study is compared with the downhole observations by Liu et al. (1997) and inverted profiles from Rosenblad et al. (2010). Rosenblad et al. (2010) estimated the velocity by inverting the surface wave dispersion data. Current figure is similar to Figure 7 in Rosenblad et al. (2010) using an analogous scale for the shear-wave velocity range.

6.11 Conclusions

A methodology has been proposed through which the non-uniqueness of the surface wave inversion is reduced for the study site near Memphis, Tennessee. Higher modes in the experimental phase velocity dispersion curve provided higher resolution in depth; however, they also added to the problem of non-uniqueness for the study case. The cost of eliminating the higher modes is technically unbearable regarding the short range of frequencies over which the fundamental mode is defined, and is shown to result in an unreliable inversion. Therefore, dealing with higher modes and the consequential non-uniqueness are unavoidable. Different mode numbers were assigned to the higher modes in the experimental dispersion curve and several cases were produced. Inversion of different cases generated multiple shear-wave velocity profiles, all fitting the observation well. To overcome the non-uniqueness, synthetic seismograms were used; for each velocity profile, full waveform time series were synthesized using a half-cycle sinusoidal source wavelet at distances corresponding to the physical location of the geophones. The

match ratio between the synthesized and observed time series helped to identify the two best-matching velocity profiles. The final velocity profiles are compared with the downhole velocity structure, and it was observed that the proposed methodology is an effective tool to overcome the non-uniqueness in the study case.

7. Future Work

Future work will concentrate on the observed discrepancy in the arrival times of the actual and synthetic data, the latter being considerable later than the former (see Figures 7.1a and 7.1b). To try to understand this discrepancy, the actual and synthetic data were converted to the frequency-wave number (f-k) domain. To account for geometric spreading, all the traces were normalized to their maximum amplitudes (in absolute value).

The corresponding results (Figures 7.2 and 7.3) show that the actual data have high amplitudes for phase velocities between about 100 m/s and 220 m/s. In contrast, the synthetic data do not have large amplitudes for velocities higher than about 150 m/s and frequencies higher than about 15 Hz. In other words, the synthetic data constitute an f-k filtered version of the actual data, with the higher velocity arrivals filtered out.

The difference in observed and synthetic arrival times should be the result of one or more of the following factors: (a) problems with the generation of the observed dispersion curves, (b) misidentification of modes, and (c) problems with the inversion of the phase velocities. We have already looked at the first two possibilities, and have identified some potential problems. To investigate possibility (a) we propose a new approach for the generation of dispersion curves. Let c indicate phase velocity.

In the new approach, the f-k plots are converted to c-f plots. This process consists in a change of the k axis, which is replaced by $c = f/k$. The corresponding results for the actual and synthetic data are shown in Figures 7.4 and 7.5. Comparison of these two figures shows that the synthetic data only include the fundamental mode, with the two higher modes missing.

To address possibility (b) we compared the phase velocities determined with a current approach (Figure 7.6) with those determined using the new approach (Figure 7.4). The differences between the two approaches are striking. While the new approach produces very clear and well-defined dispersion curves for three modes, the current approach produces a complicated pattern, which makes it difficult to identify modes without ambiguity. In particular, the lower-frequency part of the second mode is almost completely missing, and the lower-frequency part of the fundamental mode is poorly defined. Finally, it is not clear whether the alignments seen for frequencies higher than about 60 Hz have physical significance or are mere artifacts. Also note that there is a systematic difference of about 4 Hz in the frequencies.

Future work will include a phase-velocity inversion using the new phase velocities using f-k method (such as the one derived from Figure 7.4) and the generation of the corresponding synthetic seismograms. In addition, new synthetic data (with and without added noise) will be used with the two approaches to establish whether the observations described here are generally valid. As the generation of synthetic seismograms includes the computation of phase velocities, it will be another way to establish with certainty the reliability of the velocities inferred from the dispersion curves.
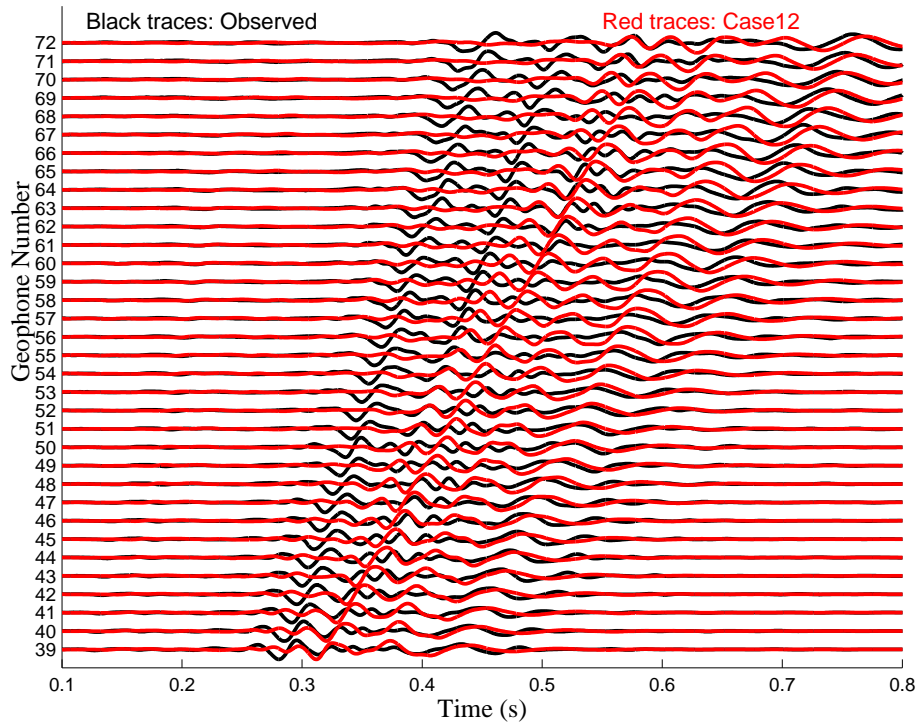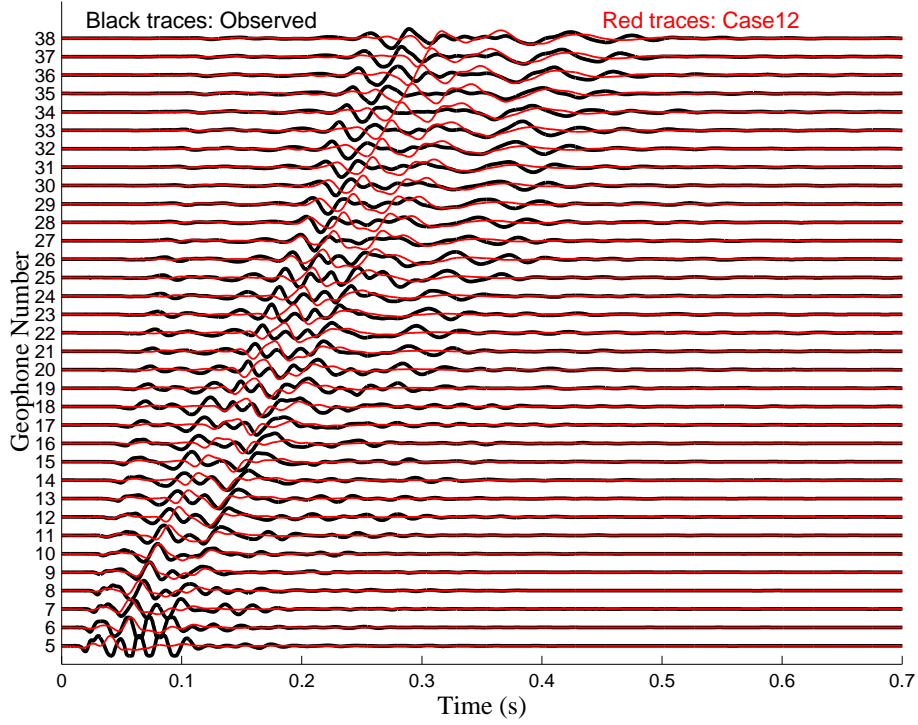
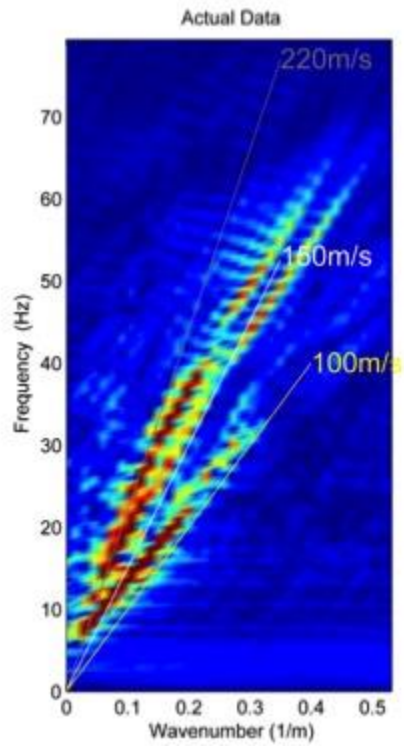*Figure 7.1. Arrival times of the (a) actual and (b) synthetic data.*
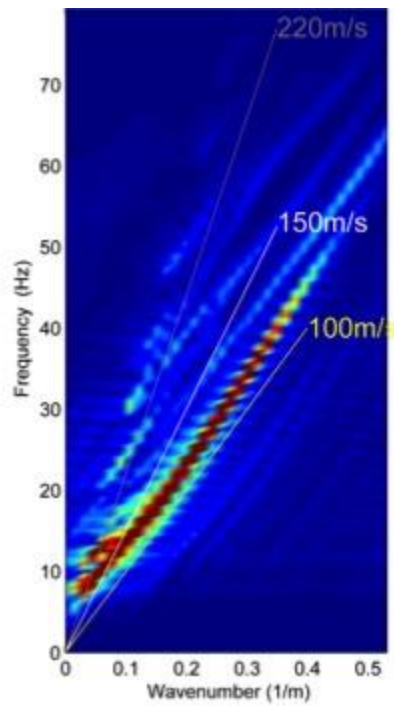
Figure 7.2 f-k-actual
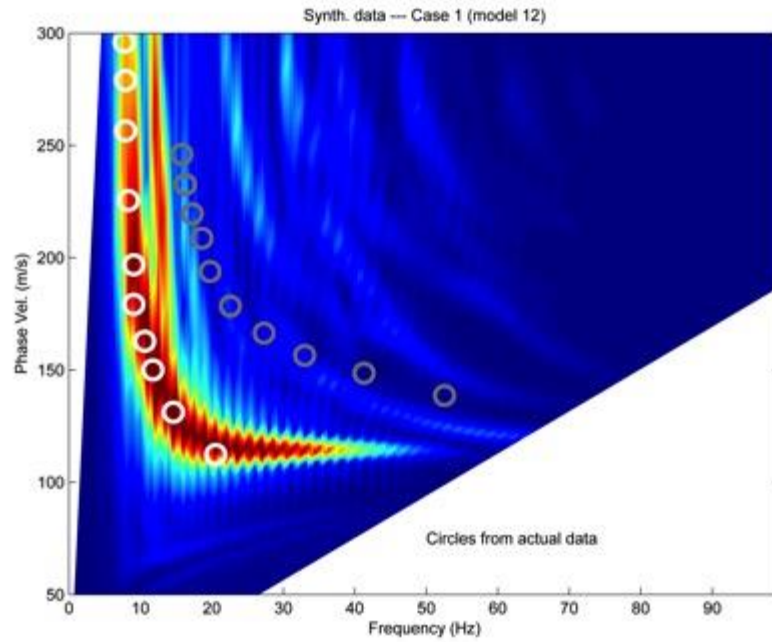

Figure 7.3 f-k-synthetic
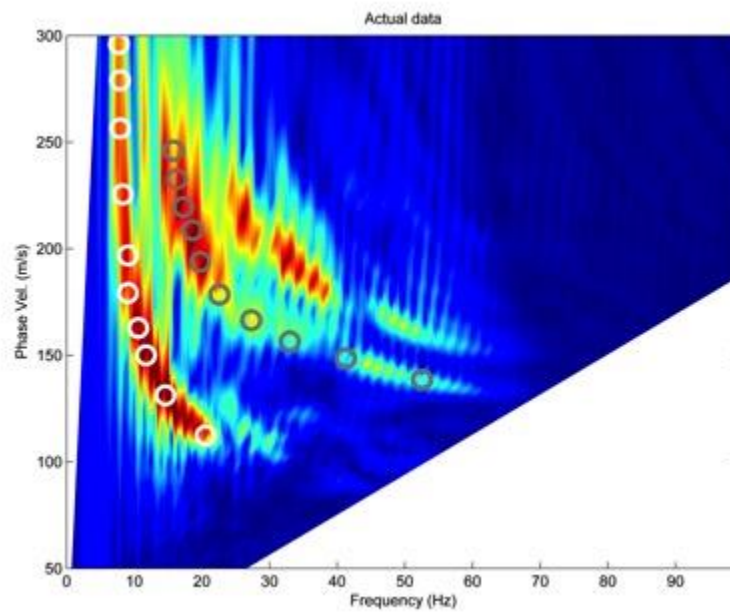
Figure 7.4. Phase velocity of actual data

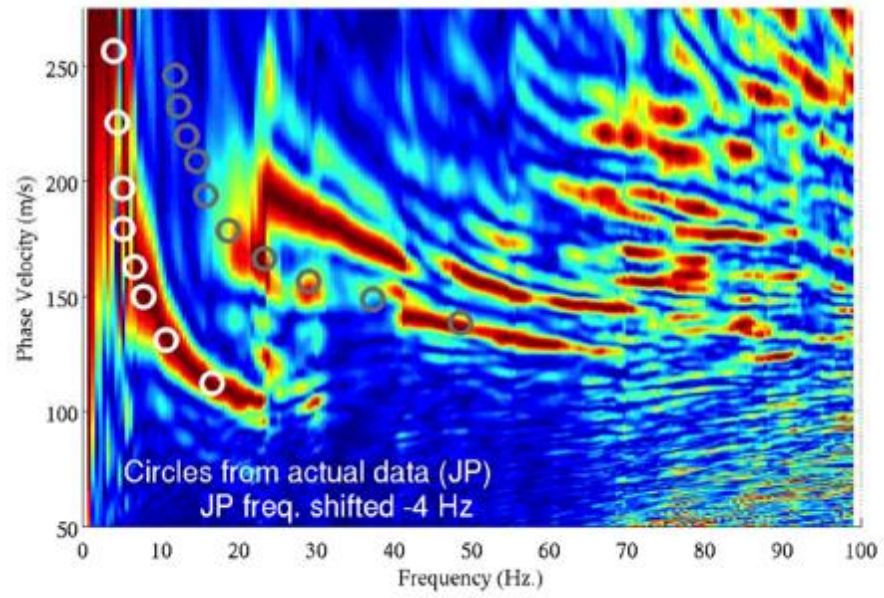*figure 7.5. Phase velocity of synthetic data*

Figure 7.6. Phase velocities of current approach as compared with phase velocities determined from Figure 7.4.

8. References

Aki, K., and P. G. Richards (1980). *Quantitative Seismology*, Freeman and Co., New York.

Ammon, C. J., G. E. Randall, and G. Zandt (1990). On the non-uniqueness of receiver function inversions, *J. Geophys. Res*. **95** 15303-15318.

Anderson, J. G. (2004). Quantitative Measure of the Goodness-of-Fit of Synthetic Seismograms, 13th *World Conference on Earthquake Engineering*, No. 243.

Aster, R. C., B. Borchers, and C. H. Thurber (2013). *Parameter estimation and inverse problems*, Elsevier, Amsterdam, 2nd edition.

Atkinson, G. M. (2012). Evaluation of Attenuation Models for the Northeastern United States/Southeastern Canada, *Seismol. Res. Lett.* **83** 166–178.

Atkinson, G., and R. Mereu (1992). The shape of ground motion attenuation curves in southeastern Canada, *Bull. Seismol. Soc. Am.* **82** 2014–2031.

Backus G., and F. Gilbert (1970). Uniqueness in the Inversion of Inaccurate Gross Earth Data, *Philos. T. Roy. Soc. A*. **266** 123-192.

Bard, P. Y., and M. Bouchon (1980a). Seismic response of sediment-filled valleys, Part 1: The case of incident *SH* waves*, Bull. Seism. Soc. Am.* **70** 1263- 1286*.*

Bard, P. Y., and M. Bouchon (1980b). Seismic response of sediment-filled valleys, Part 2: The case of incident *P* and *SV* waves*, Bull. Seism. Soc. Am.* **70** 1921- 1941.

Beaty, K., D. R. Schmitt, and M. Sacchi (2002). Simulated annealing inversion of multi-mode Rayleigh wave dispersion curves for geological structure, *Geophys. J. Int*. **151** 622-671.

Ben-Menahem A., and S. J. Singh (1981), *Seismic Waves and Sources*, Springer New York, 10.1007/978-1-4612-5856-8

Boaga, J., S. Renzi, G. Vignoli, R. Deiana, and G. Cassiani (2012). From surface wave inversion to seismic site response prediction: Beyond the 1D approach*, Soil Dynam. Earthquake Eng.* **36** 38–51.

Bodin, P., and S. Horton (1999). Broadband microtremor observation of basin resonance in the Mississippi Embayment, central US, *Geophys. Res. Lett*. **26** 903-906.

Boore, D. M., W. B. Joyner, and T. E. Fumal (1994). Estimation of response spectra and peak accelerations from western North American earthquakes: An interim report, Part 2, *U.S. Geological Survey*, Open-File Report 94-127.

Borcherdt, R. D. (1994). New developments in estimating site effects on ground motion - A new integrated methodology for estimates of site-dependent response spectra, seismic coefficients for site-dependent building code provisions, and predictive GIS maps of strong ground shaking, *New Developments in Earthquake Ground Motion Estimation and Implications for Engineering Design Practice ATC 35-1*, Applied Technology Council. **10** 1-44.

Burridge, R., and L. Knopoff (1964). Body force equivalent for seismic dislocations, *Bull. Seism. Soc. Am.* **54** 1875- 1888*.*

Brune, J. N., and J. Dorman (1963). Seismic waves and earth structure in the Canadian Shield*, Bull. Seism. Soc. Am.* **53** 167-210.

Capon, J. (1969). High-Resolution Frequency-Wavenumber Spectrum Analysis, Proceedings of the IEEE **57** 1408-1418.

Cercato, M. (2007). Computation of partial derivatives of Rayleigh-wave phase velocity using second-order sub determinants, *Geophys. J. Int.* **170** 217-238.

Cercato, M. (2009). Addressing non-uniqueness in linearized multichannel surface wave inversion, *Geophys. Prospect.* **57** 27-47.

Cerato, M., F. Cara, E. Cardarelli, G. D. Filippo, G. D. Giulio, G. and Milana (2010). Shear-wave velocity profiling at sites with high stiffness contrast: a comparison between invasive and non-invasive methods, *Near-surface Geophysics* **8** 75-94.

Conn, A., M. Chapman, S., Pezeshk, and S. M. Hosseini (2012). Path-dependent Lg propagation in the south-central United States revealed by the Earthscope transportable array, *Annual Meeting of the Seismological Society of America*, San Diego, CA.

Coruh, C. (1985). Stretched automatic amplitude adjustment of seismic data, *Geophysics* **50** 252–256.

Craig, R. F. (1992). *Soil Mechanics*, Chapman and Hall.

Cramer, C., A. Frankel, and C. Muller (2002). A state-of-the-art seismic hazard map with site effects for Memphis, Shelby County, Tennessee. 7th U.S. National Conference on Earthquake Engineering (7NCEE), Proceedings, Boston, Massachusetts.

Cramer, H. C. (2006). Quantifying the uncertainty in site amplification modeling and its effects on site-specific seismic-hazard estimation in the upper Mississippi embayment and adjacent area, *Bull. Seism. Soc. Am.* **96**(6) 2008-2020.

Dorman, J., and M. Ewing (1962). Numerical inversion of seismic surface wave dispersion data and crust-mantle structure in the New York-Pennsylvania area, *J. Geophys. Res.* **67** 5227-5241.

Dziewonski A., S. Bloch, and M. Landisman (1969). A technique for the analysis of transient seismic signals, *Bull. Seism. Soc. Am.* **59** 427-444.

Electric Power Research Institute (1993). *Guidelines for determining design basis ground motions*, Technical Report TR-102293

Evans, J. M. Jr., and S. Pezeshk (1998). West Tennessee Site Specific Studies. *EERI Annual Meeting*, San Francisco, CA, Poster Session.

Forbriger, T. (2003a). Inversion of shallow-seismic wavefields. Part I: Wavefield transformation. *Geophys. J. Int.* **153** 719-734.

Forbriger, T. (2003b). Inversion of shallow-seismic wavefields. Part II: Inferring subsurface properties from wavefield transforms. *Geophys. J. Int.* **153** 735-752.

Foti, S., and C. Strobbia (2002). Some notes on model parameters for surface wave data inversion. *Proceeding of Environmental and Engineering Geophysical Society Symposium on the Application of Geophysics to Engineering and Environmental Problems*.

Frankel, A., and J. Vidale (1992). A three-dimensional simulation of seismic waves in the Santa Clara Valley, California, from a Loma Prieta aftershock, *Bull. Seism. Soc. Am.* **82** 2045–2074.

Futterman, W. I. (1962). Dispersive Body Waves, *J. Geophys. Res.* **67** 5279-5291.

Gabriels, P., R. Snieder, and G. Nolet (1987). In situ measurements of shear-wave velocity in sediments using higher mode Rayleigh waves, *Geophys. Prospect.* **35** 187 – 196.

Gantmatcher, F. R. (1960). *Matrix Theory*, Chelsea Publishing Company, New York, NY.

Ge, J., J. Pujol, S. Pezeshk, and S. Stovall (2009). Determination of Shallow Shear Wave Attenuation in the Mississippi Embayment Using Vertical Seismic Profiling Data, *Bull. Seism. Soc. Am.* **99** 1636-1649.

Gebretsadik, E. (2005). *Geologically and well-log constrained quality factor (Q) analysis for seismic reservoir characterization*, PhD Dissertation
, University of Oklahoma.

Gladwin, M. T., and F. D. Stacey (1974). Anelastic degradation of acoustic pulse in rock, *Phys. Earth Planet. Inter.* **8** 332-336.

Groose, L. (2013). *2D full waveform inversion of shallow seismic Rayleigh waves*, PhD Dissertation, Karlsruhe Institute of Technology.

Gucunski, N., and R. D. Woods (1991). Use of Rayleigh modes in interpretation of SASW test, *Proc., 2d Int'l. Conf. on Recent Advances in Geotechnical Earthquake Eng. and Soil Dynamics*, St. Louis, MI, 1399-1408.

Hales, A. L. (1972). The travel times of P seismic waves and their relevance to the upper mantle velocity distribution, *Tectonophysics* **13** 447-482.

Haskell, N. (1953). The Dispersion of Surface Waves on Multilayered Media, *Bull. Seis. Soc. Am.* **43** 17-34.

Haskell, N. (1963). Radiation pattern of Rayleigh waves from a fault of arbitrary dip and direction of motion in a homogeneous medium, *Bull. Seis. Soc. Am.* **53** 619-642.

Haskell, N. (1964). Radiation pattern of surface waves from point sources in a multi-layered medium, *Bull. Seis. Soc. Am.* **54** 377-393.

Hebeler, G. (2001). *Site characterization in Shelby County, Tennessee using advanced surface wave methods*, Master Thesis, Georgia Institute of Technology.

Herrmann, R. B. (1987). *Computer Programs in Seismology, User's Manual II,* St. Louis University, Missouri.

Hinichi, M. J. (1981). Frequency-wavenumber array processing, *J. Acoust Soc. Am.* **69** 732-737

Hosseini, S. M., and S. Pezeshk (2011a). Comparison of phase velocities and shear-wave velocity inversion results of MASW method obtained by uniform receiver spacing analyzed by SurfSeis package software with nonuniform receiver spacing analyzed by the genetic algorithm inversion scheme, *Annual Meeting of the Geological Society of America*, Minneapolis, MN.

Hosseini, S. M., and S. Pezeshk (2011b). Multimodal inversion of phase velocity dispersion curves obtained by the MASW method using both a uniform and a nonuniform receiver spacing, *Eastern Section Annual Meeting of the Seismological Society of America*, Little Rock, AR.

Hosseini, S. M. and S. Pezeshk (2011c) "Identification and inversion of Rayleigh wave dispersion using a multimodal approach", Annual Meeting of the Seismological Society of America, Memphis, TN.

Hosseini, S. M., and S. Pezeshk (2011d). Reliability and efficiency in shear-wave velocity inversion methods and practical considerations for multimodal surface wave inversion technique, *Annual Meeting of the American Geophysical Union*, San Francisco, CA.

Hosseini, S. M., and S. Pezeshk (2012a). Improved inversion of surface waves including higher modes of propagation, *Annual Meeting of the Seismological Society of America*, San Diego, CA.

Hosseini, S. M., and S. Pezeshk (2012b). Reducing uncertainties in the velocities determined from the inversion of phase velocity dispersion curves using synthetic seismograms, *Annual Meeting of the American Geophysical Union*, San Francisco, CA.

Hosseini, S. M., and S. Pezeshk (2012c). Developments of the multi-channel surface-wave analysis method using dispersion curve and waveform comparison, *Eastern Section Annual Meeting of the Seismological Society of America*, Blacksburg, VA.

Hosseini, S. M., S. Pezeshk, M., Chapman, and A. Conn (2012). Regional investigation of geometrical spreading and quality factor in the central United States, *Annual Meeting of the Seismological Society of America*, Salt Lake City, UT.

Hosseini, S. M., F. Javadpour, and M. Tarrahi (2013) Geomechanical considerations in seismicity based reservoir characterization, *SPE 164551, SPE Unconventional Resources Conference*, The Woodlands, Texas.

Hosseini, S. M. (2013). On the application of linear elastic fracture mechanics in Barnett shale hydraulic fracturing, *ARMA 13-644, 47th US Rock Mechanics / Geomechanics Symposium, American Rock Mechanics Association*, San Francisco, California.

Hosseini, S. M., F. Aminzadeh (2013). A New Model for Geomechanical Seismicity Based Reservoir Characterization Including Reservoir Discontinuity Orientations, *SPE Annual Technical Conference and Exhibition*, New Orleans, Louisiana.

Hosseini, S. M. (2014). Reducing Uncertainties in the Velocities Determined By Inversion of Phase Velocity Dispersion Curves Using Synthetics Seismograms, Dissertation, The University of Memphis.

Hosseini, S. M., S. Pezeshk, A. Haji-Soltani, and M. Chapman (2015). Investigation of Attenuation of The Fourier Amplitude in the Caribbean Region, *Bull. Seis. Soc. Am.* 105 (2), doi: 10.1785/0120140006.

Hudson, J. A. (1969). A quantitative evaluation of seismic signals at teleseismic distances: I- radiation from a point source, *Geophys. J. R. Astr. Soc.* **18** 233-249.

Kafash M. H., D. Arellano, S. M., Hosseini, and S. Pezeshk, S. (2013). Feasibility of multi-channel analysis of surface waves (MASW) for evaluating the dynamic properties of geofoam, *Geosynthetics*, Long Beach, CA. (peer reviewed).

Kanamori, H., and D. L. Anderson (1977). Importance of Physical Dispersion in Surface Wave and Free Oscillation Problems; Review, *Rev. of Geophys. and Space Phys.* **15** 105-112.

Keilis-Borok C., and V. I. Yanovskaya (1967). Inverse problems in seismology, *J. R. Astron. Soc.* **13** 223-234.

Kennett, B. L. N., and N. J. Kerry (1979). Seismic waves in a stratified half space, *Geophys. J. R. Astr. Soc.* **57** 557-583.

Knopoff, L. (1964). Q, *Rev. Geophys.* **2** 625-6650.

Kramer, S. L. (1996). *Geotechnical Earthquake Engineering*, Prentice Hall.

Lee, W.B., and S. C. Solomon (1978). Simultaneous inversion of surface wave phase velocity and attenuation: Love waves in western North America, *J. Geophys. Res.* **83** 0148-0227.

Levshin, A. L., T. M. Sabitova, and V. P. Valus (1966). Joint Interpretation of Body and Surface Waves Data for a District in Middle Asia, *Geophys. J. Int.* **11** 57-66.

Levshin, A.L. and G. F. Panza (2006). Caveats in Multi-modal Inversion of Seismic Surface Wavefields, *Pure Appl. Geophys.* **163** 1215- 1233.

Liu, L., C. Zhou, J. W. Lane Jr., and F. P. Haeni (1997). Cross-hole radar attenuation tomography using a frequency centroid down-shift method: consideration of non-linear frequency dependency of EM wave attenuation, *67th Ann. Mtg., Soc. Expl. Geophys.* (*Expanded Abstracts*), 442–445.

Longhurst, R. S. (1967). *Geometrical and physical optics*, Longmans, Norwich.

Love, A. E. H. (1944). *Mathematical theory of elasticity*, 4th Ed: 304-305. Dover, N.Y.

Luke, B., and C. Calderón-Macias (2007). Improved parameterization to invert Rayleigh-wave data for shallow profiles containing stiff inclusions, *Geophysics* **72** U1-U10.

Luo, Y., J. Xia, J. Liu, Q. Liu, and S. Xu (2007). Joint inversion of high-frequency surface waves with fundamental and higher modes, *J. Appl. Geophys.* **62** 375–384.

Malagnini, L. (1996). Velocity and attenuation structure of very shallow soils: evidence for a frequency-dependent Q, *Bull. Seis. Soc. Am.* **86** 1471-1486.

Malagnini, L., R. B. Herrmann, G. Biella, and R. de Franco (1995). Rayleigh waves in Quaternary alluvium from explosive sources: determination of shear-wave velocity and Q structure, *Bull. Seis. Soc. Am.* **85** 900-922.

Malekmohammadi, M., and S. Pezeshk. (2014). Nonlinear Site Amplification Factors for Sites Located within the Mississippi Embayment with Consideration for Deep Soil Deposit, *Earthquake Spectra*, in press.

McNamara, D., M. Meremonte, J. Z. Maharrey, S-L. Mildore, J. R. Altidore, D. Anglade, S. E. Hough, D. Given, H. Benz, L. Gee, and A. Frankel (2012). Frequency-dependent seismic attenuation within the Hispaniola Island region of the Caribbean Sea, *Bull. Seism. Soc. Am.* **102** 773-782.

Moczo, P. (1989). Finite-difference technique for SH waves in 2D media using irregular grids – application to seismic response problem, *Geophysics* **99** 321-329.

Nazarian, S. (1984). *In Situ Determination of Elastic Moduli of Soil Deposits and Pavement Systems by Spectral Analysis of Surface Waves Method*, Ph.D Dissertation, The University of Texas at Austin.

Nazarian, S., and K. H. Stokoe II (1984). Use of Surface Waves in Pavement Evaluation, Transportation Research Record **1070** 132-144.

O'Connell, D. R. H. and J. P. Turner (2011). Interferometric Multichannel Analysis of Surface Waves (IMASW), *Bull. Seism. Soc. Am.* **101** 2122-2141.

Odum, J.K., W. J. Stephenson, R. A. Williams, and C. Von Hillebrandt-Andrade (2013). VS30 and Spectral Response from Collocated Shallow, Active-, and Passive-Source VS Data at 27 Sites in Puerto Rico, *Bull. Seism. Soc. Am.* **103** 2709-2728.

Olson, J., J. Holder, and S. M. Hosseini (2011). Soft rock fracturing geometry and failure mode in lab experiments, *SPE 140543, SPE Hydraulic Fracturing Technology Conference and Exhibition*, The Woodlands, Texas.

Park, C. B., J. Xia, and R. D. Miller (1998a). Imaging dispersion curves of surface waves on multi-channel record, *68th Ann. Internat. Mtg., Soc. Expl. Geophys.* (*Expanded Abstracts*), 1377–1380.

Park, C.B., R. D. Miller, and J. Xia (1998b). "Ground roll as a tool to image near-surface anomaly", *68th Ann. Internat. Mtg., Soc. Expl. Geophys.* (*Expanded Abstracts*), 874-877.

Park, C. B., R. D. Miller, and J. Xia (1999a). Multichannel analysis of surface waves (MASW), *Geophysics* **64** 800-808.

Park, C. B., R. D. Miller, J. Xia, J. A. Hunter, and J. B. Harris (1999b). Higher mode observation by the MASW method, *69th Ann. Mtg., Soc. Expl. Geophys.* (*Expanded Abstracts*), 524-527.

Park, C. B., R. D. Miller, J. Xia, and J. Ivanov (2000). Multichannel seismic surface-wave methods for geotechnical applications, *First International Conference on the Application of Geophysical Methodologies to Transportation Facilities and Infrastructure*, St. Louis, 11-15.

Parker, R. L. (1994). *Geophysical Inverse Theory*. Princeton University Press.

Petropsino, S., P. Cusano, G. Saccorotti, and E. Del Pezzo (2002). Seismic attenuation and shallow velocity structures at Stromboli Volcano, Italy, *Bull. Seismol. Soc. Am.* **92** 1102-116.

Pezeshk, S., and S. M. Hosseini (2013). Geometrical spreading and quality factor in the central United States, Report to Virginia Institute of Technology in fulfillment of assigned duties for the NGA-East project, *The University of Memphis*, Memphis, TN.

Pezeshk, S., and M. Zarrabi (2005). A New Inversion Procedure for Spectral Analysis of Surface Waves Using a Genetic Algorithm, *Bull. Seism. Soc. Am.* **95** 1801-1808.

Pezeshk, S., C. V. Camp, L. Liu, J. M. Evans and J. He (1998). Seismic Acceleration Coefficients for West Tennessee and Expanded Scope of Work for Seismic Acceleration Coefficients for West Tennessee Phase 2 - Field Investigation", Final Report, Project Number TNSPR-RES116, January, Prepared for the Tennessee Department of Transportation and the U.S. Department of Transportation Federal Highway Administration.

Piatti, C., S. Foti, L. V. Socco, and D. Boiero (2013). Building 3D Shear-Wave Velocity Models Using Surface Waves Testing: The Tarcento Basin Case History, *Bull. Seism. Soc. Am.* **103** 1038-1047.

Pujol, J. (2003). *Elastic wave propagation and generation in seismology*, Cambridge University Press.

Pujol, J. (2007). The solution of nonlinear inverse problems and the Levenberg-Marquardt method, *Geophysics* **72** W1-W16.

Pujol, J., S. Pezeshk, Y. Zhang, and C. Zhao (2002). Unexpected values of Q_s in the unconsolidated sediments of the Mississippi embayment, *Bull. Seism. Soc. Am.* **92** 1117-1128.

Richart, F. E., J. R. Hall, and R. D. Woods (1970). *Vibrations of soils and foundations*, Prentice-Hall Inc., New Jersey.

Rix, G. J., and C. G. Lai (1998). Simultaneous inversion of surface wave velocity and attenuation. *Geotechnical Site Characterization*, Rotterdam, Balkema 503-508.

Rix, G. J., C. G. Lai, S. Foti (2001). Simultaneous Measurement of Surface wave dispersion and attenuation curves, *Geotechnical Testing Journal*, ASTM **24** 350-358.

Ryden, N., and C. B. Park (2006). Fast simulated annealing inversion of surface waves on pavement using phase velocity spectra, *Geophysics* **71** 49-58.

Rosenblad, B., J. Bailey, R. Csontos, and R. Van Arsdale (2010). Shear Wave Velocities of Mississippi Embayment Soils from Low Frequency Surface Wave Measurements, *Soil Dynam. Earthquake Eng.* **30** 691-701.

Stokoe II, K.H., and S. Nazarian (1983). Effectiveness of ground improvement from spectral analysis of surface waves, Proceeding of the 8th European Conference on Soil Mechanics and Foundation Engineering, Helsinki, Finland.

Stovall, S. (2010). *An Improved Method for the Identification and Inversion of Multi-Mode Rayleigh Surface Wave Dispersion Collected From Non-Uniform Arrays Utilizing A Moving Source Approach*, Ph.D. Dissertation, The University of Memphis.

Stovall, S., S. M. Hosseini, and S. Pezeshk (2011). Multimodal inversion of Rayleigh wave dispersion data using a nonuniform spacing array and moving source approach, *Annual Meeting of the Earthquake Engineering Research Institute*, San Diego, CA, poster session.

Taborda R., and J. Bielak (2014). Ground-Motion Simulation and Validation of the 2008 Chino Hills, California, Earthquake Using Different Velocity Models, *Bull. Seism. Soc. Am.* Submitted.

Taylor, S. R., and M. N. Toksöz (1982). Measurement of interstation phase and group velocities and *Q* using Wiener filtering, *Bull. Seism. Soc. Am.* **72** 73-91.

Timoshenko, S. (1953). *History of the Strength of Materials*, McGraw-Hill, New York.

Tokimatsu, K., S. Tamura, and H. Kojima (1992). Effects of multiple modes on Rayleigh wave dispersion characteristics, *J. Geotech. Engrg*, American Society of Civil Engineering **118** 1529-1543.

Tran K.T., and D. R. Hiltunen (2008). A Comparison of Shear Wave Velocity Profiles from SASW, MASW, and ReMi Techniques, *Geotechnical Earthquake Engineering and Soil Dynamics IV*, Geotechnical Special Publication **181** 1-9.

Tran, K.T., and D. R. Hiltunen (2012). One-Dimensional Inversion of Full Waveform Using Genetic Algorithm, *J. Environ. Eng. Geophys.* **17** 197-213.

Turnbull, W., and A. C. Aitken (1952). *An introduction to the theory of canonical matrices*, Blackie and Son, Ltd., London and Glasgow.

Van Veen, B. D., and K. M. Buckley (1988). Beamforming: a versatile approach to spatial filtering, *IEEE ASSP Magazine* **5** 4-24.

Wang, C. Y., and R. B. Herrmann (1980). A numerical study of *P*-, *SV*-, and *SH*-wave generation in a plane layered medium, *Bull. Seis. Soc. Am.* **70** 1015-1036.

Waters, K. H. (1978). *Reflection Seismology*, John Wiley and Sons, Inc.

Xia, J., R. D. Miller, and C. B. Park (1999a). Estimation of near-surface velocity by inversion of Rayleigh wave, *Geophysics* **64** 691-700.

Xia, J., R. D. Miller, and C. B. Park (1999b). Evaluation of the MASW technique in unconsolidated sediments, *69th Ann. Internat. Mtg., Soc. Expl. Geophys.* (*Expanded Abstracts*), 437-440.

Xia, J., R. D. Miller, C. B. Park, J. A. Hunter, and J. B. Harris (2000). Comparing shear-wave velocity profiles from MASW with borehole measurements in unconsolidated sediments, Fraser River Delta, BC, Canada, *J. Environ. Engng Geophys.* **5** 1-13.

Xia, J., R. D. Miller, C. B. Park, J. A. Hunter, J. B. Harris, and J. Ivanov (2002). Comparing shear-wave velocity profiles from multichannel analysis of surface wave with borehole measurements, *Soil Dyn. Earthq. Eng.* 22 181–190.

Xia, J., R. D. Miller, C. B. Park, and T. Gang (2003). Inversion of high frequency surface waves with fundamental and higher modes, *J. Appl. Geophys.* **52** 11-23.

Yamanaka, H., and H. Ishida (1996). Application of genetic algorithms to an inversion of surface-wave dispersion data, *Bull. Seis. Soc. Am.* **86** 436-444.

Yuan, D., and S. Nazarian (1993). Automated surface wave method: Inversion Technique, *J. Geotech. Engrg.*, American Society of Civil Engineering. **119** 1113-1126.

Zeng, C. (2011). *Wavefield Analysis of Rayleigh Waves for Near-Surface Shear-Wave Velocity*, Ph.D. Dissertation, The University of Kansas.

Zywicki, D. J. (1999). *Advanced signal-processing methods applied to engineering analysis of seismic surface waves*, Ph.D. Dissertation, Georgia Institute of Technology.